

THESIS APPROVAL

The abstract and thesis of Christine Marie LeDoux for the Master of Science in Geology were presented October 23, 2007, and accepted by the thesis committee and the department.

COMMITTEE APPROVALS:

Christina L. Hulbe, Chair

Kenneth M. Cruikshank

R. Benjamin Perkins

Andrew L. Rice
Representative of the Office of Graduate Studies

DEPARTMENT APPROVAL:

Andrew G. Fountain, Chair
Department of Geology

ABSTRACT

An abstract of the thesis of Christine Marie LeDoux for the Master of Science in Geology presented October 23, 2007.

Title: A boundary element model for fracture propagation in the Ronne Ice Shelf, Antarctica.

Calving of tabular icebergs is the dominant mass loss mechanism of large Antarctic ice shelves. In the Ronne Ice Shelf, Antarctica, large rifts near the shelf front are observed to begin as fractures along the lateral boundaries of large outlet streams feeding the shelf. The purpose of this study is to understand how an initial population of fractures evolves to become the large rifts along which tabular icebergs calve. Crack tip arrest is often observed to coincide with structural boundaries, such as “suture” zones between ice from adjacent outlet glaciers. The hypothesis tested in this work is that structural boundaries in the ice shelf are important in crack tip arrest.

A set of fractures advecting from the Evans Ice Stream to the front of the Ronne Ice Shelf are investigated using propagation models based on linear elastic fracture mechanics. Fracture geometries and material boundaries were digitized from a mosaic of stacked MODIS (Moderate Resolution Imaging Spectroradiometer) images. Ice-shelf stresses were computed from velocity data collected via satellite remote sensing. Stresses are simulated using the displacement discontinuity method, a boundary element

technique. Stress intensity factors and mixed-mode fracture propagation behavior are evaluated using the maximum circumferential tensile stress criterion. Conclusions drawn from a set of experiments conducted with the model support the hypothesis.

An important goal in studying the propagation of ice shelf fractures is the development of a “calving criterion” that can be used in simulation of ice shelf and ice sheet evolution over long time scales. Current developments of calving criteria parameterize the calving rate according to longitudinal strain rates, an approach that implies a dominant role for vertical propagation in calving events. For ice shelves in wide embayments, however, the work presented here suggests that it is more physically realistic to base a calving criterion on the requirements for horizontal propagation. A criterion incorporating these findings may be developed to predict a position toward which the shelf front will tend, given a specified embayment geometry and ice thickness.

A BOUNDARY ELEMENT MODEL FOR FRACTURE PROPAGATION
IN THE RONNE ICE SHELF, ANTARCTICA

by

CHRISTINE MARIE LEDOUX

A thesis submitted in partial fulfillment of the
requirements for the degree of

MASTER OF SCIENCE
in
GEOLOGY

Portland State University

2007

DEDICATION

I dedicate this work to my father Ray. He taught me to never stop dreaming and convinced me that I could accomplish whatever I set my heart to do. He taught me to solve problems through science and mathematics, before age seven. It took many years for me to return to these disciplines, taking many paths unexpected and seldom traveled by the same individual. It required a “should have been paralyzed” personal experience to temporarily set me back on the path to science, and my father’s illness to cement that decision. So this work is dedicated to someone who cherished mathematics, engineering, and problem solving, in his own way. In a way that became more special and eccentric with time. To someone who is now losing a fight against frontal-temporal lobe dementia. It caught him too young and took away an important organ—his brain. This work is dedicated to the part of his life that he has lost and to the life that he lived. May we all become as considerate and inquisitive as he has become in his illness, with an unfettered curiosity about the world around us but armed with the tools to pursue that curiosity respectfully and productively, tools that he no longer has.

ACKNOWLEDGEMENTS

I thank my advisor Dr. Christina Hulbe for helping me to understand ice mechanics, develop skills in numerical modeling, and approach problems (and results) with a critical eye. Her “copious editorial notes” improved my scientific writing. She provided support and encouragement, especially when I needed them most. Thank you, Christina.

I appreciate the comments and suggestions provided by thesis committee members. I thank Dr. Ken Cruikshank for sharing his knowledge of fracture mechanics and the boundary element method. I thank Dr. Ben Perkins for his detailed editorial review. And I thank Dr. Andrew Rice for serving on my committee and providing suggestions.

I thank my husband Marty for his support and understanding. I thank Marty and my climbing friends for joining me on powder-filled ski trips and high descents from Mt Hood, and mountain climbing adventures in Washington and Oregon. Those trips and many summits kept me sane. I thank my late puppy Logan for her companionship when I digitized the ice shelf, and our dog Kenai for endless affection and companionship.

I thank my mother for her support and understanding, and am grateful for the strength she found to make necessary but difficult decisions. And I thank my father for the short notes he left me in my office, and the encouragement he almost always gave.

I thank the other graduate students for their friendship, even when I was not on campus often. I thank Ashleigh for working with me to understand fracture mechanics.

TABLE OF CONTENTS

Acknowledgements.....	ii
List of Tables	v
List of Figures.....	vi
Table of Variables.....	x
Table of Constants	xii
1 Introduction.....	1
2 Fracture Mechanics.....	11
2.1 Definitions	13
2.2 Assumptions	15
2.3 Governing Equations for Plane Strain	17
2.4 Stress Field near the Fracture	20
2.5 Stress Concentration near the Fracture Tip	23
2.6 Displacement Discontinuity Method	31
2.7 Model Validation.....	41
3 Methods	43
3.1 Ronne-Filcher Ice Shelf.....	43
3.2 Structural Map	45
3.3 Observed Ice Flow Used to Compute Stresses	59
3.4 Model Inputs	71
3.5 Model Outputs	76
4 Experiments	79
4.1 Experiment 1.....	83
4.2 Experiment 2.....	90
4.3 Experiment 3.....	99
4.4 Experiment 4.....	112
4.5 Experiment 5.....	119
5 Discussion.....	134
5.1 Role of Suture Zones	135

5.2	Other Insights.....	140
5.3	Model Implementation.....	145
6	Conclusions.....	147
	Literature Cited.....	153
	Appendix.....	158
A	Root-Mean Square Errors	159
B	Stress Intensity Factors	163
C	MATLAB Scripts	171
C.1	preview_data.m.....	171
C.2	get_export.m	171
C.3	read_outfile.m.....	173
C.4	plot_data.m	174

LIST OF TABLES

Table 2.1 Stress intensity factors for selected geometries subject to mode I loading	27
Table 3.1 Example of stress magnitude changes for a location of minimal shear and positive τ_{xx} , using different scaling factors.....	73
Table 3.2 Example of stress magnitude changes for a location of strong shear and negative τ_{xx} , using different scaling factors.....	74
Table 5.1 Experiments that demonstrate the importance of suture zones in fracture tip arrest. In these experiments, test fractures do not arrest at the Evans-Carlson suture zone.....	137

LIST OF FIGURES

Figure 1.1 Location of the Ronne-Filchner Ice Shelf within Antarctica and the outflow of the Evans Ice Stream	2
Figure 1.2 May 2000 calving of A-43 and A-44 icebergs from the western front of the Ronne Ice Shelf.....	4
Figure 1.3 Large rifts near the western front of the Ronne Ice Shelf observed in MODIS imagery	7
Figure 2.1 Modes of fracturing.....	11
Figure 2.2 Cartoon depicting the ice shelf as a thin plate and modes of fracturing within the ice shelf.	12
Figure 2.3. Zones of deformation within an ice shelf.....	16
Figure 2.4 Tri-polar coordinate system illustrating the physical representation of the fracture system using complex analysis with the origin at the fracture midpoint. .	22
Figure 2.5. Framework for the Inglis (1913) study of an elliptical flaw in a thin plate subject to uniformly applied stresses normal to the major axis of the flaw.....	24
Figure 2.6 Schematic of the region around the fracture tip where D is a measure of the size of the neighborhood around the fracture tip in which the stress-intensity approach is valid.	25
Figure 2.7 The stress intensity expansions given in Eq. [2.14] are valid for $R \ll D$ within the "K-dominant" neighborhood where D is the characteristic size of the outer boundary of this neighborhood.....	26
Figure 2.8 Boundary and boundary trace for boundary element method	32
Figure 2.9 Boundary element representation for model boundary in ice-shelf and for fracture.....	33
Figure 2.10 Displacement discontinuity along arbitrarily oriented line, showing global and local reference frames.	35
Figure 2.11 Flowchart describing simulation of stresses using the displacement discontinuity method and FRAC2D software.....	40
Figure 2.12 Validation of simple box with left-lateral shear.....	42
Figure 3.1 MODIS mosaic of Antarctica (Haran et al., 2005) showing Ronne-Filchner Ice Shelf.. ..	44
Figure 3.2 Digitized structural map of Ronne-Filchner Ice Shelf, based on MOA.....	47
Figure 3.3 Digitization of structural map, based on MOA (Haran et al., 2005).....	48
Figure 3.4 Evans Ice Stream drainage basin drawn over the MOA with Radarsat Antarctic Mapping Project Antarctic Mapping Mission 1 amplitude image.....	49

Figure 3.5 Ice flow near the grounding lines of the Evans Ice Stream (EvIS), Talutis Inlet (TI), Carlson Inlet (CI), and Rutford Ice Stream (RuIS).....	51
Figure 3.6 Notches in fractures near the shelf-front are interpreted as evidence of episodic fracture growth.	53
Figure 3.7 Flow features and velocity vectors in the outflow of the Evans Ice Stream.	54
Figure 3.8 Digitized features in the outflow of Evans Ice Stream.....	55
Figure 3.9 Digitized features in the outflow of Evans Ice Stream, showing provinces B and C.	57
Figure 3.10 Digitized features in the outflow of Evans Ice Stream within province D.	58
Figure 3.11 An example quadrilateral in the gridded velocity data set.	60
Figure 3.12 Small variations in observed speed due to the interferometric technique are enhanced by strain rate calculations, leading to substantial noise in strain rates. A running average smoothing filter of 20-km x 20-km was applied to the velocity data.....	62
Figure 3.13 Velocity map filtered using a 20-km x 20-km smoothing filter, based on measured ice velocity.....	63
Figure 3.14 Effective strain rate map.	64
Figure 3.15 Side view of an ice shelf of non-uniform thickness.	69
Figure 3.16 Ice thickness map of western Ronne Ice Shelf from BEDMAP.	70
Figure 4.1 Fracture geometry is defined by an upstream-pointing segment, formed along a shear margin, and a transverse segment, formed as the fracture advects through a different stress field.	79
Figure 4.2 Overview map of experiment locations in the Evans Ice Stream outflow of the Ronne Ice Shelf.....	81
Figure 4.3 Principal stress orientations and relative magnitudes for Evans Ice Stream.	82
Figure 4.4 Location of Experiment 1 in the ice shelf and model boundary	84
Figure 4.5 Experiment 1: Principal stress orientations and relative magnitudes.....	85
Figure 4.6 Experiment 1: Observed and calibrated mean stresses.	87
Figure 4.7 Experiment 1: Simulated propagation of test fracture k1 and mean stresses within model domain.	89
Figure 4.8 Location of Experiment 2 in the ice shelf and model boundaries	91
Figure 4.9 Experiment 2: Principal stress orientations and relative	92
Figure 4.10 Experiment 2: Observed and calibrated mean stresses for small model domain	94

Figure 4.11 Experiment 2: Observed and calibrated mean stresses for extended model domain.	95
Figure 4.12 Experiment 2: Simulated propagation of test fractures j3 and g6 and mean stresses within model domain. For these panels, the fracture toughness $K_{IC} = 0.3$ MPa m ^{1/2} and $\nu = 0.75$ for the fracture boundary stresses (a) Iteration 1. (b) Iteration 2.	96
Figure 4.13 Experiment 2: Simulated propagation of test fractures j3 and g6 and mean stresses within model domain. For these panels, the fracture toughness $K_{IC} = 0.3$ MPa m ^{1/2} and $\nu = 0.7$ for the fracture boundary stresses (a) Iteration 5. (b) Iteration 9.	98
Figure 4.14 Location of Experiment 3 in the ice shelf and model boundary	101
Figure 4.15 Experiment 3: Principal stress orientations and relative magnitudes.....	102
Figure 4.16 Experiment 3: Observed and calibrated mean stresses for the smaller boundary.	103
Figure 4.17 Experiment 3: Observed and calibrated mean stresses for the boundary extended 4 km to the west.....	104
Figure 4.18 Experiment 3: Simulated propagation of test fracture s6 and mean stresses within smaller model domain. The fracture toughness $K_{IC} = 0.15$ MPa m ^{1/2} and $\nu = 0.75$ for the fracture boundary (a) Iteration 7. (b) Iteration 12.	105
Figure 4.19 Experiment 3: Simulated propagation of fracture s4 and mean stresses within extended-boundary domain. The fracture toughness $K_{IC} = 0.3$ MPa m ^{1/2} and $\nu = 0.8$. Iteration 5.	106
Figure 4.20 Experiment 3: Simulated propagation of fracture s4 and mean stresses within extended-boundary domain. The fracture toughness $K_{IC} = 0.3$ MPa m ^{1/2} and $\nu = 0.75$. (a) Iteration 6. (b) Iteration 12. (c) Iteration 18.	108
Figure 4.21 Experiment 3: Simulated propagation of fracture z2 and mean stresses within extended-boundary domain. The fracture toughness was $K_{IC} = 0.3$ MPa m ^{1/2} and $\nu = 0.85$. (a) Iteration 1. (b) Iteration 2.	110
Figure 4.22 Experiment 3: Simulated propagation of fracture z2 and mean stresses within extended-boundary domain. The fracture toughness was $K_{IC} = 0.3$ MPa m ^{1/2} and $\nu = 0.8$. (a) Iteration 10. (b) Iteration 16.	111
Figure 4.23 Location of Experiment 4 in the ice shelf and model boundary.	113
Figure 4.24 Experiment 4: Principal stress orientations and relative magnitudes.....	114
Figure 4.25 Experiment 4: Observed and calibrated mean stresses.	115
Figure 4.26 Experiment 4: Simulated propagation of fracture N1 and mean stresses within model domain. The fracture toughness was $K_{IC} = 0.3$ MPa m ^{1/2} and $\nu = 0.8$. (a) Iteration 1. (b) Iteration 2.	117

Figure 4.27 Experiment 4: Simulated propagation of fracture N1 and mean stresses within model domain. The fracture toughness was $K_{IC} = 0.3 \text{ MPa m}^{1/2}$ and $\nu = 0.75$. (a) Iteration 6. (b) Iteration 12. (c) Iteration 18.....	118
Figure 4.28 Location of Experiment 5 in the ice shelf and model boundary	120
Figure 4.29 Experiment 5: Principal stress orientations and relative magnitudes for deviatoric stresses	121
Figure 4.30 Experiment 5: Effective strain rate.....	122
Figure 4.31 Experiment 5: Principal stress orientations and relative magnitudes for full glaciological stresses.....	123
Figure 4.32 Experiment 5: Observed mean and calibrated mean stresses.....	125
Figure 4.33 Experiment 5: Simulated propagation of test fracture J5 and mean stresses. The fracture toughness was $K_{IC} = 0.3 \text{ MPa m}^{1/2}$ and $\nu = 0.8$. (a) Iteration 1. (b) Iteration 12. (c) Iteration 24. (d) Iteration 36.....	127
Figure 4.34 Experiment 5: Principal stress orientations and relative magnitudes for deviatoric stresses	128
Figure 4.35 Experiment 5: Mean stresses and propagation based on simulation of mechanical interaction between test fractures A4 and J7, iteration 25.....	130
Figure 4.36 Experiment 5: Principal stress orientations and relative magnitudes for deviatoric stresses (red: extensive, cyan: compressive) based on simulation of mechanical interaction between test fractures A4 and J7, iteration 25. (.....	131
Figure 4.37 Experiment 5: Mean stresses and propagation based on simulation of mechanical interaction between test fractures A4 and J7, iteration 28.....	132
Figure 4.38 Experiment 5: Principal stress orientations and relative magnitudes for deviatoric stresses (red: extensive, cyan: compressive) based on simulation of mechanical interaction between test fractures A4 and J7, iteration 28.....	133
Figure 5.1 Outflow from Evans Ice Stream and neighboring ice streams (left to right: Carlson Inlet, Rutford Ice Stream, and Institute Ice Stream).....	136
Figure 5.2 Crevasses at the downstream ends of Kershaw Ice Rumples and Korff Ice Rise, in the outflow of the Rutford Ice Stream.....	139
Figure 5.3 Propagation orientation of fractures subject to shear stress.	141
Figure 5.4 Ice shelf thickness for Experiment 5.....	144
Figure 6.1 Idealization of mode I fracture propagation for (a) fracture length \sim ice thickness (e.g. tidewater glacier) and (b) fracture length \gg ice thickness (e.g. ice shelf).	148
Figure 6.2 AVHRR scenes from the National Snow and Ice Data Center track development of fractures in the eastern Ross Ice Shelf that resulted in the calving of a large iceberg in March 2000.	152

TABLE OF VARIABLES

Variable	Definition
σ_{ij}	= total stress, kPa
τ_{ij}	= deviatoric stress, kPa
P	= mean normal stress, kPa
ε_{ij}	= strain
σ_1	= greatest tensile stress, kPa
σ_2	= least tensile stress, kPa
a	= fracture half-length, km
$\psi(x, y)$	= Airy's stress function
K_m	= stress intensity factor for mode m
σ_{md}	= driving stress for mode m
c_x, c_y	= boundary element midpoint
\bar{x}, \bar{y}	= midpoint of element with respect to another element
β	= orientation of shear axis of element with respect to global x -axis, positive in the counter-clockwise direction
σ_s, σ_n	= shear and normal stresses relative to element, including remote stresses
b_s, b_n	= shear and normal boundary stresses, without remote stresses
D_s, D_n	= shear and normal displacement discontinuities relative to element
u_s, u_n	= shear and normal displacements for positive and negative fracture surfaces
u_x, u_y	= displacements relative to global reference frame
C	= influence coefficient
$\dot{\varepsilon}_{ij}$	= infinitesimal strain rate tensor, a^{-1}
u, v	= velocity vectors for x and y directions, m a^{-1}
$\dot{\varepsilon}_e$	= effective strain rate, a^{-1}

Variable	Definition
τ_e	= effective deviatoric stress, kPa
\mathbf{x}_n	= unit eigenvectors representing principal stress directions
λ_1	= eigenvalue representing most tensile principal stress magnitude, kPa
λ_2	= eigenvalue representing least tensile principal stress magnitude, kPa
θ	= principal stress direction for most tensile principal stress
H	= ice thickness, m
τ_1, τ_2	= principal deviatoric stresses, kPa
\mathfrak{S}	= scaling factor for principal stresses
M_{ij}	= remote stress tensor, kPa
θ_0	= angle of propagation for mixed mode loading
$D_{\max m}$	= maximum displacement at element midpoint due to mode of loading m

TABLE OF CONSTANTS

Constant	Definition
γ	= parameter defined for fracture geometry, $-0.806/\sqrt{2}$
A	= flow law rate factor, value dependent on temperature and other conditions
n	= flow law parameter, 3
B	= inverse rate factor, $760 \text{ kPa a}^{1/3}$ (Larour et al., 2005)
g	= acceleration due to gravity, 9.8 m s^{-2}
ρ	= depth-integrated ice density, 910 kg m^{-3}

1 Introduction

Large, transverse fractures that appear near the fronts of ice shelves become the planes along which large icebergs calve. In the Ronne Ice Shelf, Antarctica (Figure 1.1), such rifts are observed to begin as shear-margin fractures along the lateral boundaries of large outlet streams feeding the shelf. The fractures may grow as they are advected through the shelf, responding to changes in the local stress field. The local stress field depends on the glaciological (far-field) stress, the geometry of the fracture, and the geometries of nearby fractures. Inhomogeneity of the ice may also be important. Propagation depends on the stress concentration at the fracture tip and may be episodic (growth followed by arrest and re-initiation). It is important to understand how relatively small fractures evolve into large ice shelf rifts so that physical processes governing ice shelf mass balance may be accounted for in predictive ice sheet models.

The study area is in the outflow of the Evans Ice Stream, which has the largest influx of ice to the Ronne Ice Shelf and a simple flow history. The Ronne-Filchner Ice Shelf is the second largest ice shelf in Antarctica, with a combined area of 487,000 km² (Sandhager et al., 2004). Ten ice streams flow from the West and East Antarctic Ice Sheets into the ice shelf. Berkner Island lies between the Ronne and Filchner ice shelves.

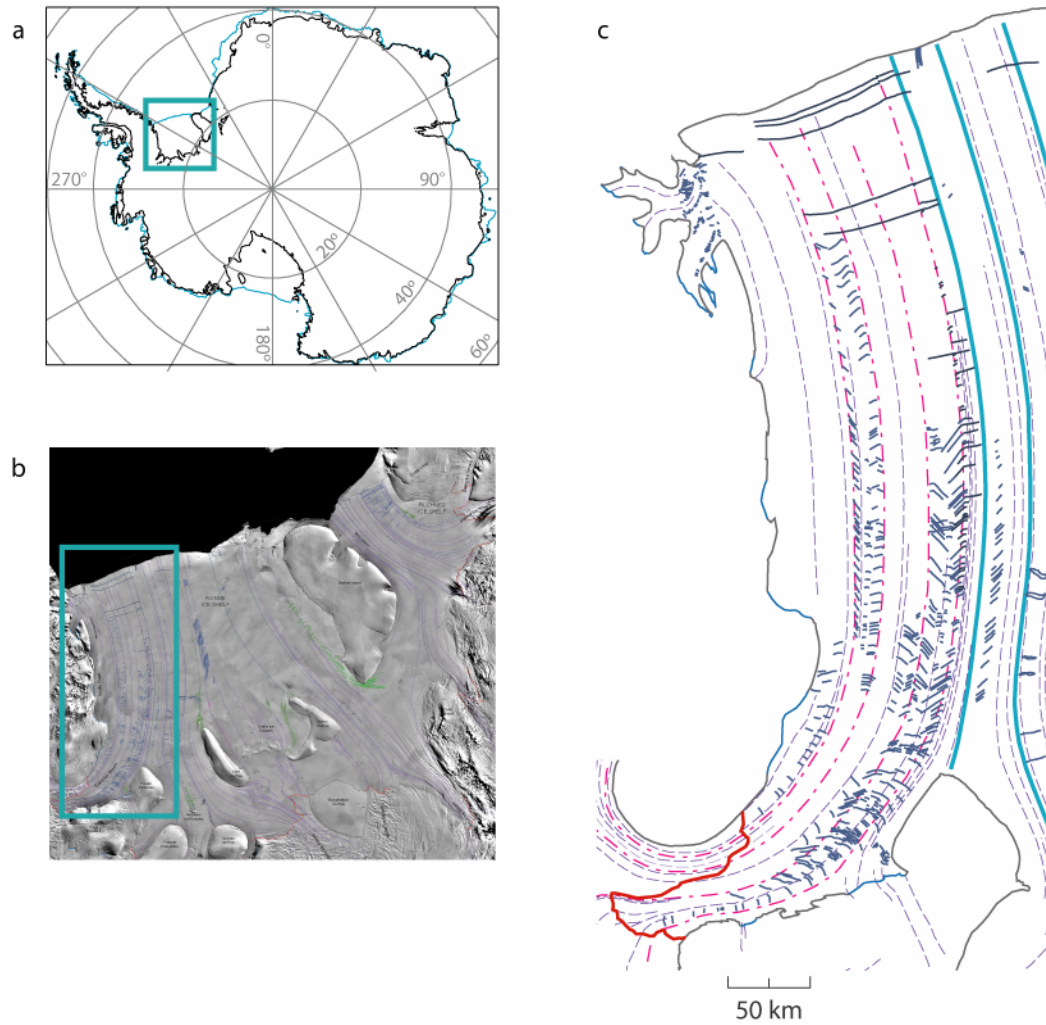


Figure 1.1 (a) Location of the Ronne-Filchner Ice Shelf within Antarctica. (b) The Ronne-Filchner Ice Shelf with the location of the outflow of the Evans Ice Stream outlined by solid line. Image from the MODIS Mosaic of Antarctica (Haran et al., 2005). (c) The outflow of the Evans Ice Stream, in the western Ronne Ice Shelf. Ice-shelf features and fractures digitized from the remote-sensed imagery in (b).

Ice Shelf Mass Balance

An ice shelf is a thick, floating platform of ice that may form at the terminus of an outlet glacier that flows into a sufficiently deep body of water (Paterson, 1994, p. 289).

The two largest ice shelves in Antarctica, the Ross and the Ronne-Filchner, serve as the

conduits through which approximately two-thirds of ice leaving the West Antarctic Ice Sheet (WAIS) flows. The WAIS rests on bedrock below sea level, most of which would remain below sea level even if all of the ice were removed. This “marine” character has been cited as a possible cause for instability in the ice sheet–ice-shelf system were ice-shelf geometry to change significantly (Mercer, 1978; Thomas et al., 1979).

Fast-moving ice streams transport ice from the interior of the ice sheet to the floating ice shelves. The grounding line, or location where ice begins to float, migrates seaward or landward in response to changing mass balance of the system. Ice shelf mass accumulation occurs through ice discharged from ice streams and outlet glaciers, marine ice accretion at the base of the ice shelf, and snowfall. Ablation occurs through calving of large tabular icebergs, melting at the underside of the shelf, and surface melting. The Ronne-Filchner Ice Shelf is the second largest ice shelf in Antarctica, with a combined area of 487,000 km² (Sandhager et al., 2004).

Calving of tabular icebergs is the dominant mass loss mechanism of large Antarctic ice shelves (Paterson, 1994 , p. 44). The large tabular icebergs A-43 and A-44, which calved from the western front of the Ronne Ice Shelf in May 2000 (Figure 1.2), contained an ice mass of 2075×10^{12} kg, approximately equivalent to one year’s accumulation across the entire Antarctic Ice Sheet (2326×10^{12} kg a⁻¹; Giovinetto and Zwally, 2000). By comparison, melting from ice shelves is ~ 544 kg a⁻¹ (Jacobs et al., 1992).

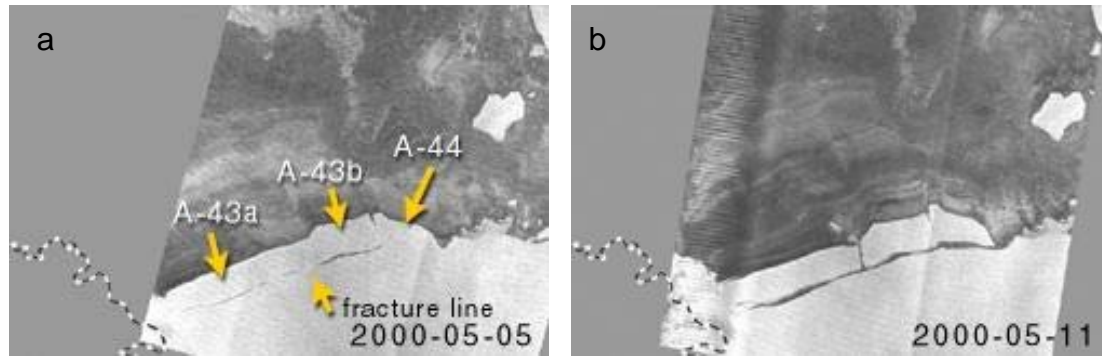


Figure 1.2 May 2000 calving of A-43 and A-44 icebergs from the western front of the Ronne Ice Shelf. Images derived from RADARSAT-1 ScanSAR by Canadian Centre for Remote Sensing (2000). Prior to splitting into sections A and B, A-43 measured approximately 257 km by 36 km (9252 km²) and A-44 measured approximately 72 km by 31 km (2232 km²). (a) May 5, 2000. (b) May 11, 2000.

The dominance of iceberg calving in mass loss from the WAIS and the role of fractures in ice shelf collapse events (Hughes, 1983; Scambos et al., 2000) make fracture propagation an important process to understand. Yet few ice-sheet models in use today incorporate principles from fracture mechanics in the description of mass loss at the calving fronts of ice shelves. This is, in part, because the topic is poorly understood. Insights gained in the present work may advance the development of useful parameterizations for mass loss due to iceberg calving at the fronts of large ice shelves.

Fracture Mechanics

Fractures are an observable effect of stress in a material. They form during the deformation associated with many geologic events, including landslides (Fleming and Johnson, 1989; Palmer and Rice, 1973), fault displacements (Aydin and Johnson, 1978; Fleming and Johnson, 1989), and glacier flow (Hambrey and Müller, 1978; Nemat-

Nasser et al., 1979; Nye, 1957; Smith, 1976; Weertman, 1973). Fractures may nucleate as microcracks, originating from an internal weakness in the material such as an air pocket. If the fracture nucleates but the local stress field is in equilibrium, the fracture will not grow. Changes in the stress field drive propagation. These changes may include an increase in fluid pressure within the fracture or modification to the remote stress. Stresses are concentrated at the fracture tips and fracture propagation occurs when tip stress intensity exceeds a critical material value, the fracture toughness. In the present work, through-cutting rifts, crevasses, and cracks are treated as mixed-mode fractures that can be studied using linear elastic fracture mechanics (LEFM) theory.

Structural boundaries may initiate or arrest growth, or change the direction of fracture propagation. In geologic materials, fracture propagation often terminates at discontinuities such as lithologic boundaries, faults, or other fractures (Degraff and Aydin, 1987). Fracture geometries mapped for this thesis indicate that important structural boundaries may arrest fracture growth. Structural boundaries include former shear margins or suture zones formed by ice originating from different ice streams.

Glacier systems provide a unique opportunity to observe the evolution of fractures. It is rare to observe active fracture propagation in geologic settings. The relative accessibility of fractures in glacier ice (at the surface, not in deeply buried rocks) offers more opportunities than are available in other geologic settings. For the small process zone near the fracture tip, episodic fracture growth has been observed by direct measurement (Bassis et al., 2005). This growth occurs on short time scales (minutes to hours) and is confined to a small region near the tip. Here, we are interested in large-

scale features that are observed by remote sensing (Figure 1.3). Growth occurs over medium-length time scales (days or longer) and the stress shadow cast by the fracture extends beyond the region near the tip.

Fractures in glacier ice form where stresses are large enough to exceed the fracture toughness of the ice. Such conditions often arise at stick-slip boundaries such as grounding lines and lateral margins. Once initiated, fractures advect downstream with ice flow, propagating according to the stress intensity at the fracture tips. Near the shelf front, large transverse fractures develop, becoming the planes along which icebergs calve.

Crack Tip Arrest

Several mechanisms may drive crack tip arrest. We observe that the large rifts in the Ronne Ice Shelf (more than 30 km in length) begin as starter fractures in shear zones along the lateral boundaries of ice streams. As these fractures advect towards the shelf front, the propagation direction may change or a fracture tip may become inactive. Stress intensity at the fracture tip increases with increasing fracture length. Thus, the longer a fracture becomes, the more likely it is to continue propagating in a given remote stress field. Yet fractures in the ice shelf (and other geologic materials) are observed to have finite lengths. The explanation for this is typically that interaction among adjacent fractures reduces stress intensity at the fracture tip and limits propagation. In the Ronne Ice Shelf, inhomogeneity within the ice also appears to be important.

Crack tip arrest is often observed to coincide with structural boundaries, such as “suture” zones between ice from adjacent outlet ice streams (Figure 1.3). Downstream, the fracture may reactivate and arrest at another structural boundary. We hypothesize that these structural boundaries are important in crack tip arrest. To test this hypothesis, we model fracture propagation in the ice shelf.

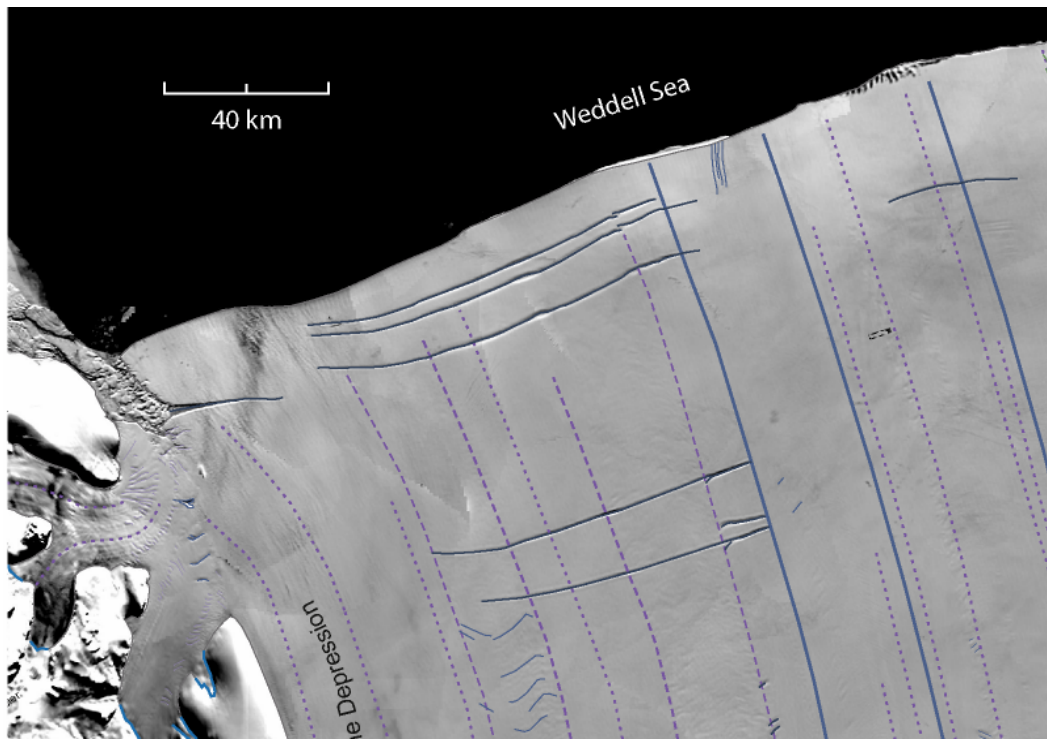


Figure 1.3 Large rifts near the western front of the Ronne Ice Shelf observed in MODIS imagery (Haran et al., 2005). Near the shelf front, these rifts exceed 100 km in length. Solid blue lines trace the boundaries between the outflow of ice from different ice streams; purple dashed lines trace suture zone; and purple dotted lines represent streaklines.

In order to study the effect of structural boundaries on propagation, we pose the question – is the glaciological stress field sufficient to propagate a given fracture? Two outcomes are possible. If the fracture propagates but we do not observe propagation in the ice shelf, then the structural boundary must play an important role in crack tip arrest.

If the fracture does not grow, then the stress conditions must not be favorable to growth and we learn little about the role of the structural boundary.

Numerical Method

In the present work, fracture propagation in ice is treated as an elastic boundary value problem. Boundary value problems are solved using a variety of numerical techniques. One approach is to simulate stresses throughout a region of interest, which is divided into a network of elements (finite element method). This method requires stress conditions to be specified for all elements of a design mesh within the model domain (Hughes, 2000). An alternative approach, the boundary element method (BEM), requires only discretization of the boundary and fractures, resulting in a smaller set of equations. The displacement discontinuity method (DDM) is a boundary element method developed to handle slit-like openings or thin fractures. A displacement discontinuity is the relative movement of one side of the fracture to the other, assumed constant along the length the fracture or boundary element.

Stresses are simulated throughout a fractured region in several steps. First, the fracture is divided into a number of elements and a constant displacement discontinuity assigned to each element. Next, the influences of the elements on one another are described using fundamental solutions that satisfy the governing differential equations, resulting in a set of influence coefficients. A system of linear equations composed of the known boundary stresses and the influence coefficients for these stresses is then solved

for the unknown elemental displacement discontinuities. Once the displacement discontinuities are computed for the boundary elements, stresses are computed along the fracture and at specified locations within the surrounding region using the principle of superposition. These stresses are due to the combined influences of the boundary stresses, and the geometry and proximity of any fractures within the region. Finally, the computed stresses at the fracture tips are used in fracture mechanics equations to compute stress intensity factors and predict propagation.

Objectives

The thesis has two components: (1) mapping fractures and other features of interest in the Ronne Ice Shelf, and (2) application of the boundary element method to study the evolution of fractures that advect downstream and eventually become large shelf-front rifts. Fracture geometries and structural boundaries are digitized from stacked composite MODIS (Moderate Resolution Imaging Spectroradiometer) satellite images (Haran et al., 2005). A set of fractures advecting from the Evans Ice Stream to the front of the Ronne Ice Shelf (Figure 1.1c) are investigated using propagation models based on linear elastic fracture mechanics. Ice-shelf strain rates and associated stresses are computed from measured velocity data (Ian Joughin, UW Applied Physics Laboratory, personal communication, 2005). Model boundary conditions and elasticity parameters are calibrated to achieve reasonable agreement between model and observed stress fields.

The boundary element method used here is the displacement discontinuity method by Crouch and Starfield (1983). The method has been applied to study fracture geometries in rock (Olson and Pollard, 1989; Sempere and Macdonald, 1986) and the propagation of magma-filled fractures deep within Earth (Dahm, 2000). A suite of user input-driven tools is developed that can be used to study fracture propagation at nearly any location within the ice shelf. Once validated for the selected fractures, the model may be used to study past and present fracture propagation at other locations, including within other ice shelves that satisfy model assumptions.

2 Fracture Mechanics

Fracture mechanics provides the physical and mathematical framework for studying fracture propagation in glacier ice. Lawn and Wilshire (1975, p. 81) define three modes of fracturing (Figure 2.1). Mode I propagation ('opening mode') occurs when the fracture is subject to tensile stresses normal to the fracture plane. Displacement of the fracture walls is perpendicular to the fracture plane. The fracture tip propagates in the direction of least tensile stress. Mode II propagation ('sliding mode') results from shear loading in the fracture plane. Displacement occurs in the plane and normal to the fracture edge. Mode III propagation ('tearing mode') results from out-of-plane shear loading. Here, our interest is in mode I and II mixed-mode fracture propagation (Figure 2.2).

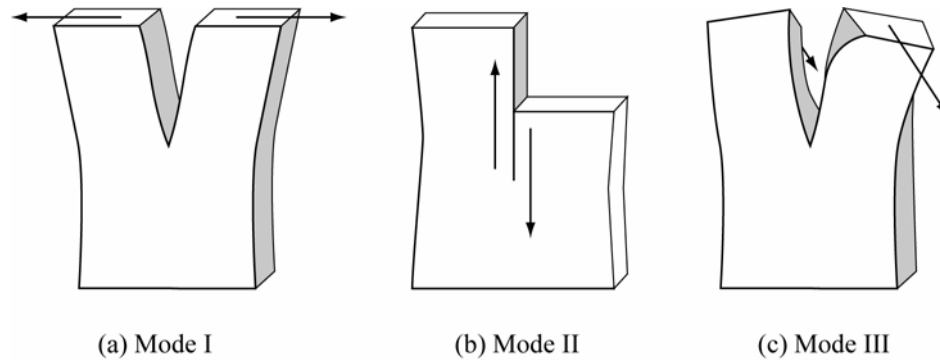


Figure 2.1 Modes of fracturing: mode I ('opening'), mode II ('sliding'), and mode III ('tearing').

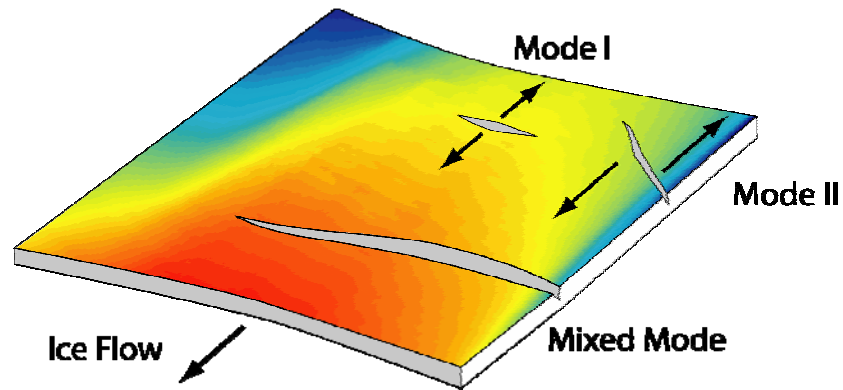


Figure 2.2 Cartoon depicting the ice shelf as a thin plate, in which the vertical dimension is much smaller than the horizontal dimensions. Mode I fractures propagate normal to the direction of most extensive principal stress, here due to longitudinal extension. Mode II fractures are located within shear margins in the ice where ice speed at the margin is much lower than within the main body of ice flow. Shaded area represents ice speed within an ice shelf.

Fracture propagation is controlled by the stress intensity at the fracture tip, computed using stress intensity factors for each mode of propagation, and fracture toughness, a material property defined as a critical stress intensity factor beyond which propagation will occur. If the stress intensity at the fracture tip exceeds the fracture toughness of the ice, the fracture will propagate. In the ice shelf, stress intensity at the tip may be reduced by mechanical interactions with other fractures or by inhomogeneities in the ice. Two types of interaction may be important in the study area:

1. A single propagating fracture may enter the region of influence of a pre-existing fracture. This can lead to crack tip arrest or a change in orientation of the propagating fracture (Cotterell and Rice, 1980).
2. Closely-spaced (the distance between fractures is small relative to the fracture lengths), subparallel fractures may affect each others' propagation. A longer fracture may inhibit growth of neighboring fractures or fractures of equal

lengths may inhibit each other from continued propagation (Pollard and Aydin, 1988).

Inhomogeneities in the ice are observed at structural boundaries in the ice shelf such as suture zones between adjacent former shear margins. Two conditions might occur:

1. If the stress field changes within the suture zone, the stress intensity at the fracture tips may be reduced, leading to tip arrest or the formation of kinks as the direction of propagation adjusts to the new stress conditions.
2. The fracture toughness of the material may change in response to softer ice (warmer or more highly fractured) or more brittle ice (colder). These conditions can further affect other material properties of the ice, such as the constants of elasticity.

Finally, if driving stress is present within the fracture but propagation cannot occur at one endpoint, the fracture may grow at the other endpoint, propagating until the stress intensity falls below the fracture toughness of the material. Increased fracture length may also lead to (re-)initiation of the opposite fracture tip.

2.1 Definitions

Some background on linear elastic fracture mechanics (LEFM), a branch of continuum mechanics, may aid the reader. Two types of forces act on a material: (1) *body* forces (e.g. gravity), which act equally on all elements of the material, and (2) *surface* forces (e.g. pressure and friction), which act along or across the surface of the material. Compared to the surface forces, body forces due to gravity acting upon the

low-slope, floating ice-shelf become insignificant and are ignored. The *total stress* acting on a plane within a material is a tensor σ_{ij} , where i, j are directions in a coordinate system. A Cartesian coordinate system with axes $x, y,$ and z is used here. In the present work, the y -axis is roughly aligned with ice flow (longitudinal) and the x -axis is orthogonal to ice flow (lateral); the z -axis denotes the vertical direction of the floating ice shelf (thickness). Using this convention, σ_{xx} (σ_{yy}) is the normal stress acting in the x -direction (y -direction) on the plane orthogonal to the x -axis (y -axis) and σ_{xy} is the shear stress acting in the x -direction on the plane orthogonal to the y -axis. The stress can be decomposed into *shear stress* components (e.g. σ_s) acting tangential to the surface and *normal stress* components (e.g. σ_n) acting normal to the surface. Materials deform according to the *deviatoric stress* τ_{ij} , which is the difference between the total stress σ_{ij} and the *mean normal stress* P , or *overburden pressure*. *Strain* ε_{ij} is a measure of the deformation in response to an applied stress. *Remote stresses* are far-field stresses resolved over a length scale that is large compared to the fracture length.

The sign convention follows the tension-positive approach, commonly used for fracture mechanics and mixed-mode fracture growth. In the tension-positive convention, normal tensile stresses are positive and normal compressive stresses are negative. The greatest tensile stress is designated σ_1 and the least tensile stress is designated σ_2 , for two dimensions. The sign convention for shear stresses is more complicated. Here, the sign of the outward normal to the face and the direction of the applied shear stress acting on the face determine the sign of the shear stress. For

example, a shear stress σ_{yx} acting on the plane whose normal is in the $+y$ direction and has stress applied in the $+x$ direction is positive.

Elasticity constants describe the behavior of a material in response to loading and are integral to relationships between stress and strain (Hooke's Law). The essential quantities used throughout the present work are defined here. The shear modulus μ describes the relationship between shear stress and strain, such that $2\mu = \sigma_{xy} / \varepsilon_{xy}$. The modulus of elasticity E is a measure of the stiffness of a material, $\sigma_{xx} / \varepsilon_{xx}$. Poisson's ratio ν is the ratio between contraction and extension in a deformed material, such that $\nu = -\varepsilon_{xx} / \varepsilon_{yy}$. The bounds on Poisson's ratio are $-1 < \nu \leq 0.5$. If the material is incompressible, $\nu = 0.5$ (Davis and Selvadurai, 1996, p. 51).

2.2 Assumptions

Fracture growth can be studied using linear elastic plane strain theory, which requires that certain assumptions be satisfied. A linear elastic material is assumed to be homogeneous, with material properties that do not vary spatially—it is isothermal and isotropic. The response of glacier ice to stresses within the material depends on the temperature, ice fabric, time scale, and other factors. At depth and on very long time scales (tens to thousands of years), glacier ice behaves as a ductile fluid, deforming viscously (Figure 2.3). Near the surface and on shorter time scales, glacier ice behaves elastically and undergoes brittle fracture at sufficiently large stresses. In the present work, our interest is in the elastic behavior of glacier ice on medium-length time scales

(days to months). That is, the growth of fractures (e.g. crevasses or rifts) in a floating, flowing ice mass.

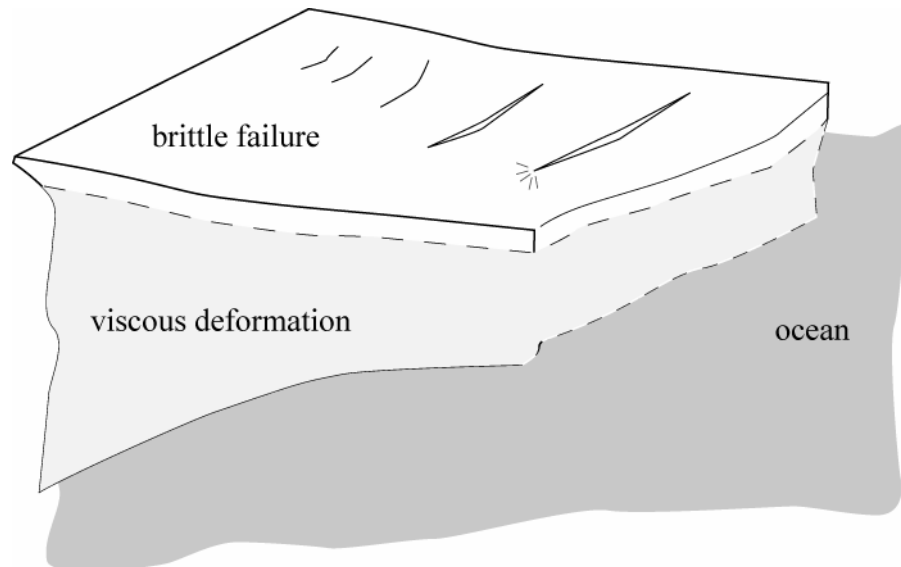


Figure 2.3. Zones of deformation within an ice shelf.

Although the ice shelf is three-dimensional, we are interested in fracture propagation in the horizontal directions. The vertical dimension is much smaller than the horizontal dimensions, allowing it to be neglected and a plane strain condition to be assumed (Figure 2.2). The plane strain assumption requires that the fracture geometry, material properties, and boundary conditions, including boundary tractions, do not vary in the vertical direction. Strain is taken to be zero in the vertical direction, while stress, due in large part to the overburden pressure, is nonzero. We assume that material properties are constant across the fracture for any given depth and that tidal displacement does not affect one side more than the other.

The deformation of glacier ice on medium-length time scales (days or longer) can be described by fluid dynamics, a branch of continuum mechanics that studies fluid flow. Observational evidence supports the assumption that ice flow in the study area is steady with respect to time (Chapter 3). The steady-state assumption allows us to equate the evolution of a suite of fractures in space with the evolution of a single fracture in time. That is, the observed downstream fracture geometries represent the evolution of an arbitrary fracture as it advects through the ice shelf. We wish to understand the nature of the evolution in terms of response to the remote stress field and to the structure of the ice shelf.

2.3 Governing Equations for Plane Strain

The governing equations of a plane strain problem are the equilibrium equations, compatibility equation, and constitutive relationships between stress and strain. These equations allow us to derive the biharmonic equation, which is the fundamental equation solved in elasticity problems.

Force balance is required by Newton's second law of motion, which states that the rate of change of the momentum of a body is directly proportional to the net force acting on it, and the direction of the change in momentum takes place in the direction of the net force. Ignoring body forces, the *equilibrium equations* for two dimensions are:

$$\begin{aligned}\frac{\partial \sigma_{xx}}{\partial x} + \frac{\partial \sigma_{xy}}{\partial y} &= 0 \\ \frac{\partial \sigma_{xy}}{\partial x} + \frac{\partial \sigma_{yy}}{\partial y} &= 0\end{aligned}\tag{2.1}$$

The in-plane strains and displacements are related by:

$$\varepsilon_{xx} = \frac{\partial u}{\partial x} \quad \varepsilon_{yy} = \frac{\partial v}{\partial y} \quad \varepsilon_{xy} = \frac{1}{2} \left(\frac{\partial u}{\partial y} + \frac{\partial v}{\partial x} \right)\tag{2.2}$$

in which u and v represent the x - and y - components of velocity. The *compatibility equation*, which must be true for a continuous material, ensures that the material remains continuous following deformation, without holes or discontinuities. For two dimensions, the compatibility equation is:

$$2 \frac{\partial^2 \varepsilon_{xy}}{\partial x \partial y} = \frac{\partial^2 \varepsilon_{xx}}{\partial x^2} + \frac{\partial^2 \varepsilon_{yy}}{\partial y^2}\tag{2.3}$$

(Muskhelishvili, 1963, § 15, p. 44).

The relationship between stress and strain in a homogeneous, isotropic, linear elastic material that meets the conditions of plane strain with independent elastic parameters (i.e. Hooke's law) is:

$$\begin{aligned}\varepsilon_{xx} &= \frac{1}{2\mu} \left[\sigma_{xx} - \nu (\sigma_{xx} + \sigma_{yy}) \right] \\ \varepsilon_{yy} &= \frac{1}{2\mu} \left[\sigma_{yy} - \nu (\sigma_{xx} + \sigma_{yy}) \right] \\ \varepsilon_{xy} &= \frac{1}{2\mu} \sigma_{xy}\end{aligned}\tag{2.4}$$

(Muskhelishvili, 1963).

This set of equations—two equilibrium equations ([2.1]), the compatibility equation ([2.3]), and the stress-strain Hooke's law relations ([2.4])—must be satisfied by the three in-plane stresses $(\sigma_{xx}, \sigma_{yy}, \sigma_{xy})$ for any solution of a plane strain problem. This system of equations and unknowns is computationally difficult. It is made simpler using an Airy stress function $\psi(x, y)$ (Airy, 1863) such that the equilibrium equations are satisfied:

$$\begin{aligned}\sigma_{xx} &= \frac{\partial^2 \psi}{\partial y^2} \\ \sigma_{yy} &= \frac{\partial^2 \psi}{\partial x^2} \\ \sigma_{xy} &= -\frac{\partial^2 \psi}{\partial x \partial y}\end{aligned} \quad . \quad [2.5]$$

Substituting the stress-strain relations ([2.4]) into the compatibility equation ([2.3]), and using partial derivatives of the equilibrium equations ([2.1]), the compatibility equation in terms of the in-plane stresses is:

$$\left(\frac{\partial^2}{\partial x^2} + \frac{\partial^2}{\partial y^2} \right) (\sigma_{xx} + \sigma_{yy}) = \nabla^2 (\sigma_{xx} + \sigma_{yy}) = 0 \quad [2.6]$$

in which ∇^2 is the Laplace operator. Using Airy's definitions from [2.5], the compatibility equation expressed in terms of the Airy stress function ψ is:

$$\nabla^4 \psi = 0 \quad . \quad [2.7]$$

The solution to the plane strain problem lies in finding an appropriate biharmonic Airy stress function, examples of which can be found in elasticity handbooks (e.g.,

Timoshenko and Goodier, 1969). Any stress function $\psi(x, y)$ that satisfies equation [2.7] is a solution to a plane strain problem.

2.4 Stress Field near the Fracture

Stresses in terms of partial derivatives of harmonic functions in x and y are not simple to solve. Muskhelishvili (1963) developed a method for solving plane strain problems using complex analysis. This method uses two analytical functions $\varphi(z)$ and $\chi(z)$ (Pollard and Segall, 1987) of the complex variable $z = x + iy$, where $z = re^{i\theta}$. The complex exponential function $e^{i\theta}$ is related to trigonometric functions by $e^{\pm in\theta} = \cos n\theta \pm i \sin n\theta$. The analytical functions are related to the Airy stress function by

$$\psi = \frac{1}{2} \operatorname{Re} \left[\bar{z} \varphi(z) + \chi(z) \right]. \quad [2.8]$$

For pure mode I loading, (Westergaard, 1939) found that this solution could be reduced to a single analytical stress function $\varphi_I(z)$. Sih (1966) introduced the function $\varphi_{II}(z)$ to account for pure mode II loading in the y -direction. The single fracture stress function $\varphi_m(z)$, in which m represents the mode of loading, may be written (Pollard and Segall, 1987):

$$\varphi_m(z) = A_m \left[(r_1 r_2)^{1/2} e^{i(\theta_1 + \theta_2)/2} - r e^{i\theta} \right] + B_m r e^{i\theta} \quad [2.9]$$

where for plane strain,

$$\begin{aligned}
A_m &= \left[\left(\sigma_{xx}^r - \sigma_{xx}^c \right), -i \left(\sigma_{xy}^r - \sigma_{xy}^c \right) \right] \\
B_m &= \left[\left(\sigma_{xx}^r + \sigma_{yy}^r \right) / 2, 0 \right]
\end{aligned}
\tag{2.10}$$

Here, A_m is the driving stress, which is the difference between the remote stress resolved on the fracture (superscript r) and the pressure at the fracture surface (superscript c). B_m represents the mean stresses, which can be taken as the contribution of the remote stresses in the absence of the fracture.

The fracture is represented geometrically using complex space and a tri-polar coordinate system (Figure 2.4), where

$$\begin{aligned}
r_1^2 &= (x-a)^2 + y^2 \\
r_2^2 &= (x+a)^2 + y^2
\end{aligned}
\tag{2.11}$$

and

$$\begin{aligned}
\theta_1 &= \arctan \frac{y}{x-a} \\
\theta_2 &= \arctan \frac{y}{x+a}
\end{aligned}
\tag{2.12}$$

In Figure 2.4, the fracture half-length, a , is aligned with the x -axis. The transformation equations for the complex variable z are:

$$\begin{aligned}
z &= r e^{i\theta} \\
z - a &= r_1 e^{i\theta_1} \\
z + a &= r_2 e^{i\theta_2}
\end{aligned}
\tag{2.13}$$

in which $r_1 = 0$ and $r_2 = 0$ correspond to the fracture endpoints.

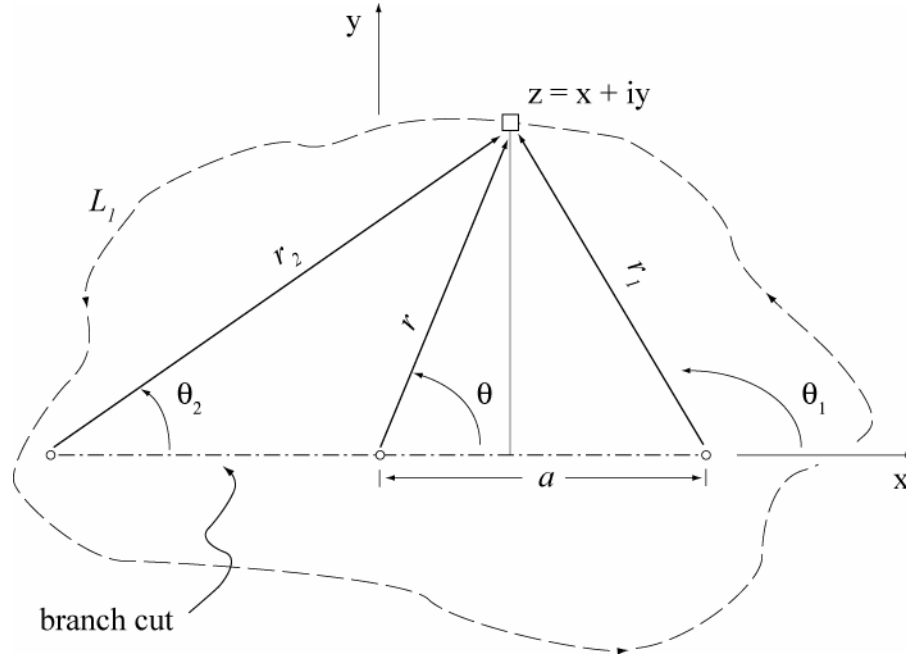


Figure 2.4 Tri-polar coordinate system illustrating the physical representation of the fracture system using complex analysis with the origin at the fracture midpoint. The line $|x| < a$ represents the branch cut that ensures that the analytical function $\varphi_m(z)$ is single-valued for L_1 . Modified from Pollard and Segall (1987).

$\varphi_m(z)$ is a multi-valued “function.” That is, using Figure 2.4 as a reference, the traversal of the path L_1 includes all three origins and we find that, for an increase of 2π in both θ and $(\theta_1 + \theta_2)/2$ (from Eq. [2.9]), $\varphi_m(z)$ returns to its original value. Multi-valued functions introduce discontinuities and are typically handled by constructing a branch cut in the complex plane. The origin 0 is the “branch point.” Because $\ln z$ is undefined for $z=0$, where $e^z = 1$, a branch cut is constructed between the origins $r_1=0$ and $r_2=0$ to limit the domain of $\log z$. The branch cut coincides with the discontinuity introduced by the fracture surface and ensures that the stress function $\varphi_m(z)$ is single-valued throughout the domain.

Analytical solutions for the stress components σ_{ij} have been derived for specific, relatively simple geometries (e.g., Pollard and Segall, 1987). For the more complicated geometries and stress conditions observed in an ice shelf, numerical methods such as those developed by Crouch and Starfield (1983) are required (section 2.6).

2.5 Stress Concentration near the Fracture Tip

In addition to evaluating the stress field near the fracture, we want to determine if the fracture will propagate and if so, the propagation direction. Stress intensity factors at the fracture tips are used to compute fracture propagation criterion.

The solutions for the stress field around a fracture break down near the fracture tip. Inglis (1913) first showed that stress concentration near the fracture tip depends on the shape of curvature of the region in which stresses are focused (Figure 2.5). The radius of curvature \wp is derived from the equation for an ellipse so that $\wp = b^2/a$, where b is the total displacement across the fracture and a is the fracture half-length. Griffith's (1921) analysis centered on minimizing the free energy of the fracture system. Irwin (1957) extended Griffith's energy balance criterion to develop an approach that evaluates the stress intensity in the vicinity of a fracture tip. Stress intensity factors K_m depend on the fracture geometry and applied loading, where the subscript m represents the mode of loading. Departing from Inglis' elliptical study specimen, many of the later approaches (Irwin, 1957; Paris and Sih, 1965) are based on the "sharp slit" approximation (Figure 2.6). The "sharp slit" introduces a singularity at the fracture tip,

which is handled through the methods of complex analysis described in the previous section. The stress-intensity approach is limited to a *neighborhood* near the fracture tip with radius D (Figure 2.6).

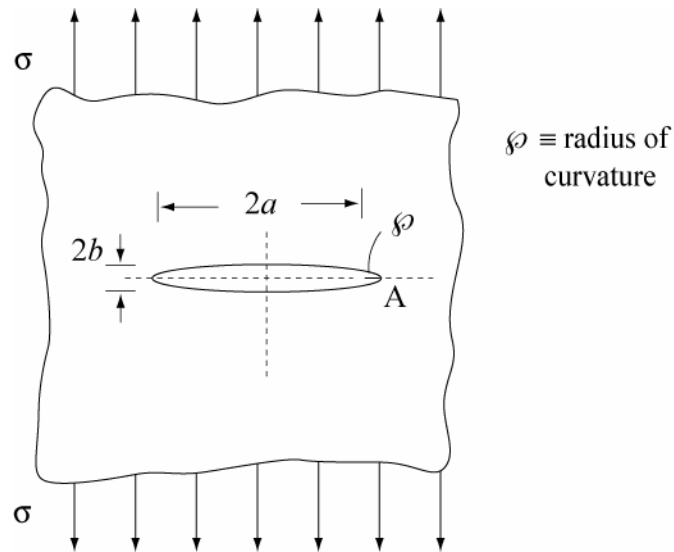


Figure 2.5. Framework for the Inglis (1913) study of an elliptical flaw in a thin plate subject to uniformly applied stresses normal to the major axis of the flaw.

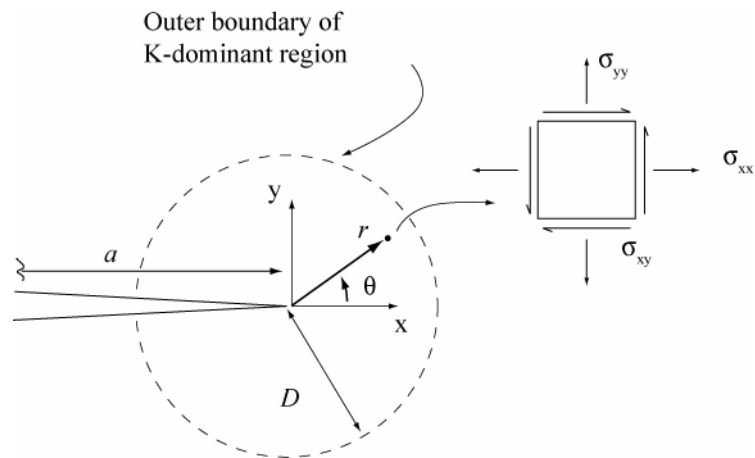


Figure 2.6 Schematic of the region around the fracture tip where D is a measure of the size of the neighborhood around the fracture tip in which the stress-intensity approach is valid. Here, a represents the fracture half-length. Box indicates stress fields acting on an infinitesimal element at radial distance r from the fracture tip and orientation θ relative to the x -axis (stresses are positive). Modified from Kanninen and Popelar (1985, p. 141).

The simple form of the analytical solution for stress components near the fracture tip is:

$$\sigma_{ij} = K_I (2\pi r)^{-1/2} f_{ij}(\theta) , \quad [2.14]$$

in which K_I is the stress-intensity factor for mode I fracture propagation and the distribution of the stress field is described by a radial component with $r^{-1/2}$ dependence and a function $f_{ij}(\theta)$ that depends on the orientation of a given point with respect to the fracture plane (Irwin, 1957; Kanninen and Popelar, 1985; Lawn and Wilshaw, 1975; Pollard and Segall, 1987). These approximations have several limitations. Higher-order terms are omitted, making solutions valid only for the region in which the leading terms are dominant, or in a small region surrounding the tip. In a purely elastic or Hookean material, the stresses at the tip are singular, growing to infinity if the fracture exceeds a critical length. Most materials, however, experience a small amount of plastic deformation in the process zone, designated by the circle of radius R in Figure 2.7. If the process zone is small compared to the fracture length or to the distance between the fracture tip and the next open surface (radius D , the characteristic size of the outer boundary), then the LEFM approach applies and the simple form of the analytical solution in equation [2.14] is valid. Pollard and Segall (1987) found that in the region in front of the fracture tip, the stresses approximated by equation [2.14] were within 15% of real stresses for $r < 0.01a$. For a fracture half-length of 5 km, typical for some fractures in this study, the radius for this region is approximately 50 meters.

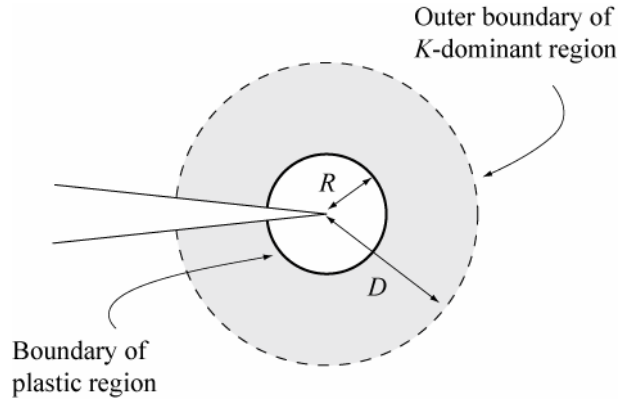


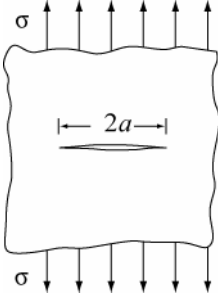
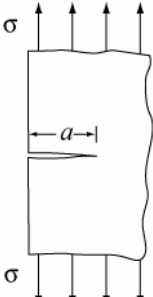
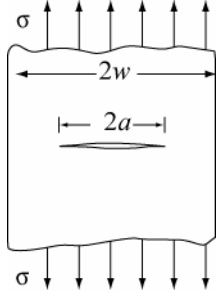
Figure 2.7 The stress intensity expansions given in Eq. [2.14] are valid for $R \ll D$ within the “K-dominant” neighborhood where D is the characteristic size of the outer boundary of this neighborhood. In this region, the leading terms of the expansions are dominant. The fracture criterion is not valid within the process zone enclosed by the white circle of radius R immediately surrounding the fracture tip. Diagram modified from (Kanninen and Popelar, 1985, p. 146).

To compute the stresses near the tip using Equation [2.14], the stress intensity factor K_m must be calculated. The general form of the stress-intensity factor is:

$$K_m = \gamma \sigma_{md} \sqrt{\pi a} , \quad [2.15]$$

in which σ_{md} represents the driving stress for mode m , a is the fracture half-length, and γ is some constant parameter defined by the fracture geometry. The principle of superposition applies for the linear system so that stress-intensity factors for a given mode are additive. Analytical solutions for various specimen geometries are found in reference volumes such as Tada et al. (2000). Several simple fracture geometry specimens are shown in Table 2.1.

Table 2.1 Stress intensity factors for selected geometries subject to mode I loading (Sih, 1973; Tada et al., 2000).

Description	Geometry	Stress intensity factor
Infinite solid with center fracture and constant tensile stress applied normal to fracture		$K_I = \sigma\sqrt{\pi a}$
Semi-infinite solid with edge fracture and tensile stress applied normal to fracture		$K_I = 1.12\sigma\sqrt{\pi a}$
Double-ended center fracture in long plate of finite width 2w with tensile stress applied normal to fracture		$K_I = \sigma\sqrt{\pi a} \left[\frac{2w}{\pi a} \tan\left(\frac{a}{2w}\right) \right]^{\frac{1}{2}}$ <p data-bbox="1036 1140 1170 1171">For $a \ll w$</p> $K_I = \sigma\sqrt{\pi a} \left[\sec\left(\frac{\pi a}{2w}\right) \right]^{\frac{1}{2}}$

The analytical solutions in Equation [2.15] require an evaluation of the driving stress but this quantity is difficult to calculate in most settings. Displacement of the material near the fracture and across the fracture surface, which occurs in response to the driving stress, is simpler to compute than driving stress. This displacement creates a discontinuity. One numerical method for approximating this is the displacement discontinuity method (Crouch and Starfield, 1983).

Stress-intensity factors K_I and K_{II} are computed using the maximum displacement at the active fracture tips (those allowed to propagate). In theory, maximum displacement $D_{\max i}$ due to the mode of loading m occurs at the midpoint of the fracture element. The equation for maximum displacement,

$$D_{\max m} = \sigma_{md} \frac{4(1-\nu^2)}{E} a , \quad [2.16]$$

can be solved for driving stress,

$$\sigma_{md} = \left[\frac{E}{4(1-\nu^2)} \right] D_{\max m} a . \quad [2.17]$$

Here, the maximum displacements at the tip elements are calculated for each of the relevant modes of fracturing:

$$\begin{aligned} D_I &= u_n^- - u_n^+ \\ D_{II} &= u_s^- - u_s^+ \end{aligned} \quad [2.18]$$

in which u_n and u_s are the displacements in the normal and shear directions that are computed using the displacement discontinuity method. Equation [2.17] is substituted into Equation ([2.17]):

$$K_m = \gamma \left[\frac{E}{4(1-\nu^2)} \right] D_{\max m} \sqrt{\frac{\pi}{a}} \quad [2.19]$$

in which K_I and K_{II} depend on the maximums of D_I and D_{II} , respectively, for the fracture and γ is a constant parameter defined by the fracture geometry. In the present work, $\gamma = -0.806/\sqrt{2}$.

The $\sigma(\theta)_{\max}$ theory, formulated by Erdogan and Sih (1963), provides a method for evaluating mixed-mode fracture growth. Here, propagation is governed by the maximum circumferential tensile stress $\sigma(\theta)_{\max}$ near the fracture tip. The $\sigma(\theta)_{\max}$ theory is:

$$\sigma_{\theta}(2\pi r)^{1/2} = \text{constant} = \cos \frac{\theta_0}{2} \left(K_I \cos^2 \frac{\theta_0}{2} - \frac{3}{2} K_{II} \sin \theta_0 \right) = K_{IC} \quad [2.20]$$

(Ingraffea, 1987, p. 92), where θ_0 is the angle of propagation for mixed-mode loading.

Dividing by K_{IC} , this is

$$1 = \cos \frac{\theta_0}{2} \left(\frac{K_I}{K_{IC}} \cos^2 \frac{\theta_0}{2} - \frac{3}{2} \frac{K_{II}}{K_{IC}} \sin \theta_0 \right), \quad [2.21]$$

The right side of [2.21] is evaluated for mixed-mode propagation. When it is equal to or exceeds 1, fracture propagation occurs. The fracture criterion in [2.21] requires the computation of θ_0 , the angle of propagation for mixed-mode loading. This angle is derived from the condition that propagation occurs in the plane in which shear stress is zero:

$$\cos \frac{\theta_0}{2} \left[K_I \sin \theta_0 + K_{II} (3 \cos \theta_0 - 1) \right] = 0 \quad [2.22]$$

(Ingraffea, 1987, p. 93). Ignoring the trivial solution, $\cos(\theta_0/2) = 0$ where $\theta_0 = \pm\pi$, the more useful solution is:

$$K_I \sin \theta_0 + K_{II} (3 \cos \theta_0 - 1) = 0 . \quad [2.23]$$

The propagation direction equation may be simplified for different conditions. Under pure mode I loading, such that $K_{II} = 0$, the only condition under which propagation is aligned with the fracture plane occurs when:

$$K_I \sin \theta_0 = 0 \rightarrow \theta_0 = 0^\circ . \quad [2.24]$$

For pure mode II loading, where $K_I = 0$,

$$\begin{aligned} K_{II} (3 \cos \theta_0 - 1) = 0 &\rightarrow \theta_0 = \pm \cos^{-1} \left(\frac{1}{3} \right) \\ \theta_0 &= -70.5^\circ \end{aligned} \quad [2.25]$$

For mixed-mode loading, the condition of interest in the ice shelf, [2.23] is re-arranged:

$$\frac{K_{II}}{K_I} = \frac{-\sin \theta_0}{3 \cos \theta_0 - 1} . \quad [2.26]$$

The angle of propagation θ_0 for mixed-mode loading is:

$$\theta_0 = -2 \tan^{-1} \left[\frac{1}{8K_{II}} \left(-2K_I + 2\sqrt{K_I^2 + 8K_{II}^2} \right) \right] . \quad [2.27]$$

2.6 Displacement Discontinuity Method

The displacement discontinuity method is a boundary element method that approximates the stresses due to the presence of fractures within a material (Crouch and Starfield, 1983). This method has not previously been applied to ice shelf fractures but has been applied in other geologic contexts (Dahm, 2000; Olson and Pollard, 1989; Sempere and Macdonald, 1986). The software used in this study is C-based Frac2D (Thomas, 1991), which employs the displacement discontinuity method (DDM) presented in the TWODD software (Crouch and Starfield, 1983). The software was modified for an MS-DOS environment (Cruikshank, 2005, personal communication).

A fracture can be viewed as a series of point disturbances within a stress field. The fractures selected for this study have considerable length relative to the areal extent of the study area in the ice shelf, so the problem domain is treated as a finite region Q of variable size enclosed within a boundary L_1 (Figure 2.8a). The constitutive equations introduced in section 2.3 describe the physics within the region Q (the “glaciological stress”). Analytical solutions can be written to describe the effect of each point disturbance on the stress field. These singular solutions are valid for every point within the region except the point of disturbance itself. The governing partial differential equations are linear so the complete solution is formed by summation of individual solutions. Because analytical solutions are easier to find for infinite plane problems than for finite plane problems, the boundary L_1 is treated as a tracing contour L_1' within an infinite plane (Figure 2.8b; Crouch and Starfield, 1983, p. 3-4). The sum of all singular

solutions should approximate conditions along the tracing contour L_1' , the model boundary.

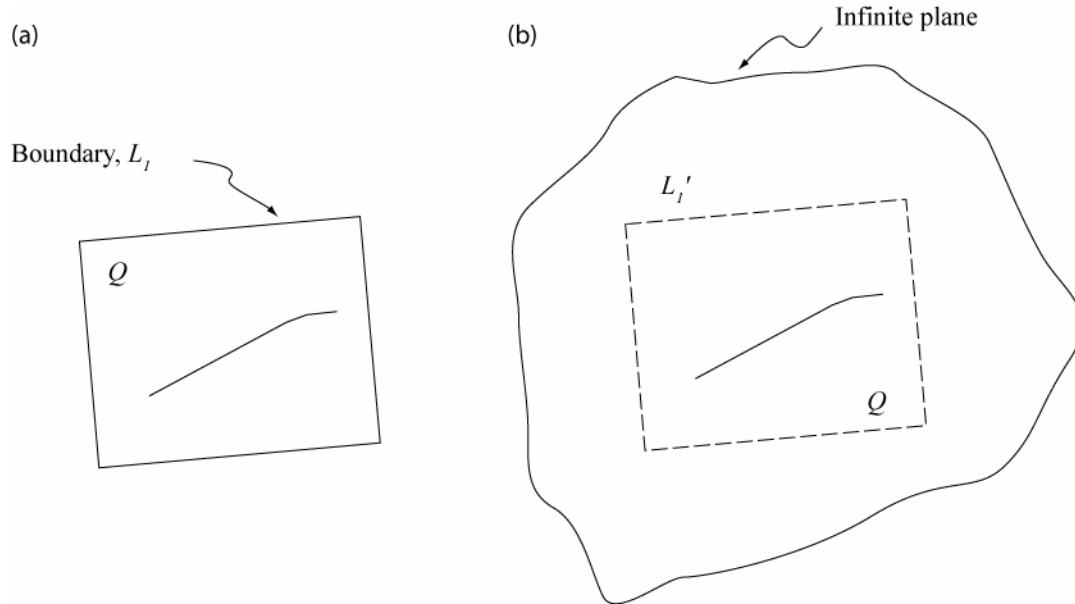


Figure 2.8 (a) Boundary L_1 enclosing region Q and (b) boundary trace L_1' within infinite plane. Modified from Crouch and Starfield (1983, p. 3).

Boundary elements are the framework through which stresses are simulated. Boundary conditions are specified by discretizing the model boundary and fracture into elements, which are defined by start- and end-points of straight-line segments, with shear and normal stresses σ_s and σ_n specified at the midpoints. These are hereafter referred to as the *boundary stresses*. Boundary elements are concatenated end-to-end (Figure 2.9). Each boundary element $i \{i \in 1 \dots N\}$ has a half-length of a^i . Stresses are computed for other locations within the model domain using an observation grid composed of elements (*observation stresses*, not shown in Figure 2.9).

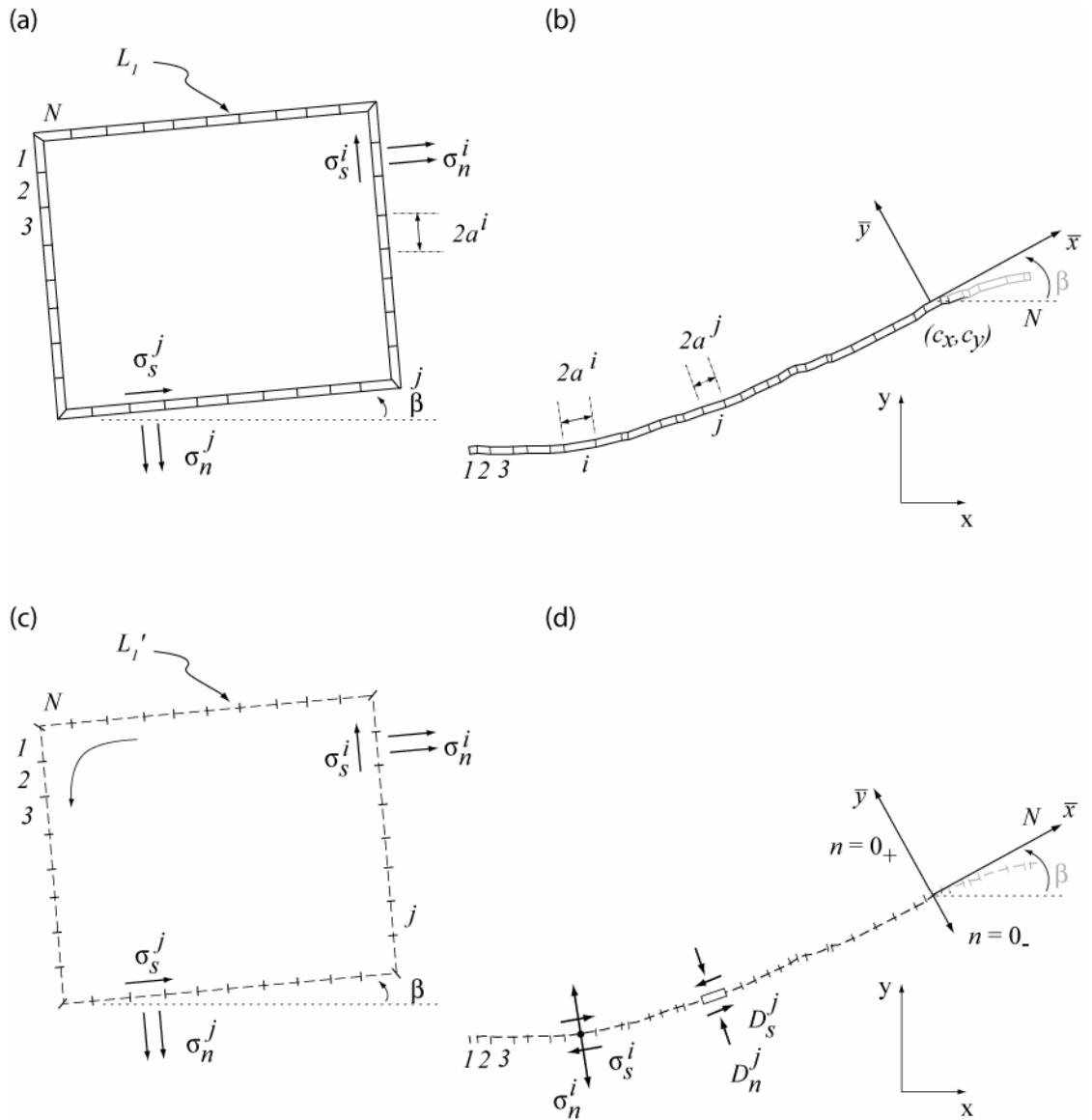


Figure 2.9 Boundary element representation for model boundary in ice-shelf and for fracture. Model boundary: (a) physical method and (c) numerical method. Model fracture: (b) physical method and (d) numerical method. Modified from Crouch and Starfield (1983, p. 54, 87).

Complicated fracture geometries make it convenient to adopt a local reference frame for each boundary element. The local reference frame has its origin at the element midpoint (c_x, c_y) (Figure 2.10). For convenience, different coordinate systems are used to describe the local reference frames of boundary stresses and observation stresses,

based on input and output products. For boundary stresses, the x -axis is rotated so that the *shear* axis is aligned with the boundary element (positive in the direction of transversal) and the y -axis is rotated so that the *normal* axis is normal to the boundary element (positive in the outward direction). For observation stresses, which are expressed using the Cartesian coordinate system, and stresses computed using the analytical solution (Crouch and Starfield, 1983, p. 81), the local reference frame is defined by an \bar{x} -axis (shear) and a \bar{y} -axis (normal). The angle β defines the orientation of the \bar{x} axis with respect to a global x -axis, positive in the counter-clockwise direction. Coordinate displacements and stresses are transformed between the global and local reference frames.

Displacement discontinuities require two surfaces of the boundary element. If the boundary element of a fracture occupies $|\bar{x}| \leq a, \bar{y} = 0$, then the positive fracture surface is at $\bar{y} = 0^+$ and the negative surface is at $\bar{y} = 0^-$. Displacement discontinuities relative to the element are expressed as $D_{\bar{x}}$ and $D_{\bar{y}}$ (D_s and D_n). They are assumed continuous everywhere except across the fracture and the change in displacement is assumed constant for any boundary element. By convention, negative $D_{\bar{y}}$ (D_n) indicates that the fracture surfaces are moving away from each other ('opening') and negative $D_{\bar{x}}$ (D_s) indicates that the positive fracture surface is moving to the left relative to the negative fracture surface (Figure 2.10).

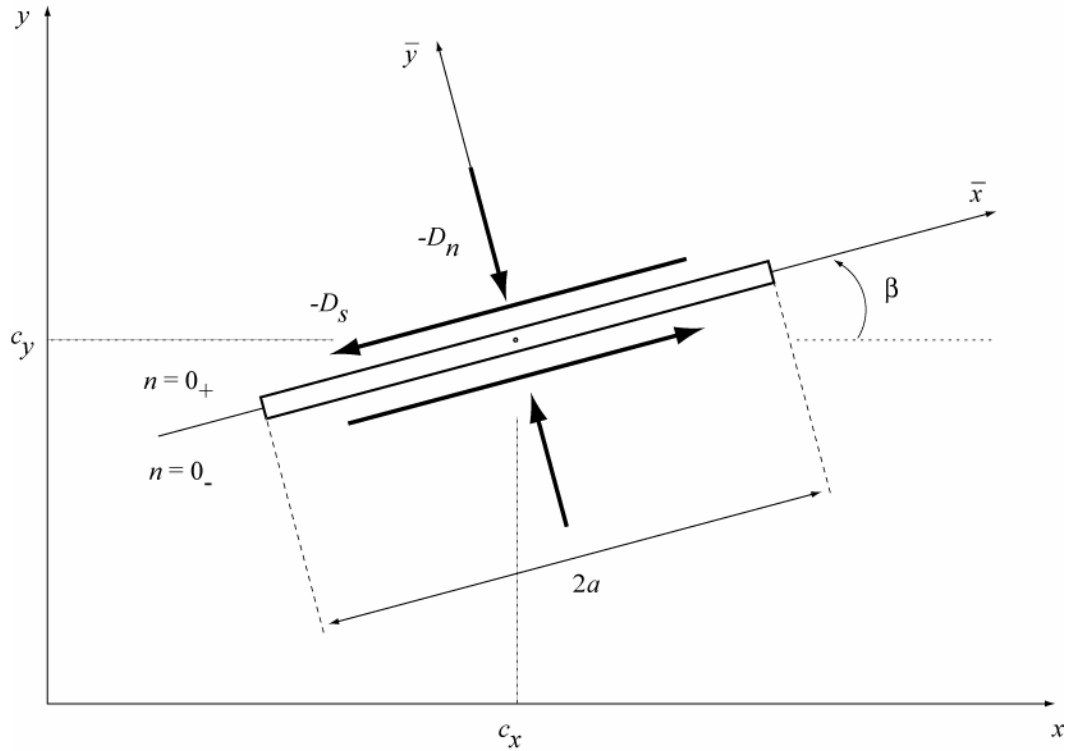


Figure 2.10 Displacement discontinuity along arbitrarily oriented line, showing global and local reference frames. Modified from Crouch and Starfield (1983, p. 91).

It is assumed that each boundary element has uniform stress conditions and material properties, including constants of elasticity and fracture toughness K_{IC} . The boundary stresses for each element i and remote stresses for the model domain are transformed from the global to local reference frame using rotation transformation equations (Crouch and Starfield, 1983, p. 13):

$$\begin{aligned}\sigma_s &= \frac{(\sigma_{yy} - \sigma_{xx}) \sin 2\beta}{2} + \sigma_{xy} \cos 2\beta \\ \sigma_n &= \sigma_{xx} \cos^2 \beta - \sigma_{xy} \sin 2\beta + \sigma_{yy} \sin^2 \beta\end{aligned}\quad [2.28]$$

in which σ_s and σ_n represent the shear and normal stresses of the element. Remote stresses are removed, leaving boundary stresses b_s and b_n that are due to near-field stresses and the presence of fractures within the shelf.

Because we consider the influence of each element on every other element, a new index j is introduced to represent the element that is acting *on* another element i . The element j must be transformed so that its midpoint coordinates (c_x^j, c_y^j) are expressed relative to the local reference frame of the element i , which has origin (c_x^i, c_y^i) :

$$\begin{aligned}\bar{x}^j &= (c_x^i - c_x^j) \cos \beta^j + (c_y^i - c_y^j) \sin \beta^j \\ \bar{y}^j &= -(c_x^i - c_x^j) \sin \beta^j + (c_y^i - c_y^j) \cos \beta^j.\end{aligned}\quad [2.29]$$

Here, coordinates (\bar{x}^j, \bar{y}^j) represent the midpoint of the transformed element with respect to element i and angle β^j represents the orientation of the \bar{x} axis of element j relative to the global x -axis. The elemental displacement discontinuities $(D_s^j, D_n^j)^i$ represent the change in displacement across an element i due to the influence of element j , where:

$$\begin{aligned}D_s^j &= u_s^{j-} - u_s^{j+} \\ D_n^j &= u_n^{j-} - u_n^{j+}.\end{aligned}\quad [2.30]$$

Here, u_s and u_n represent the shear and normal displacements for the positive and negative fracture surfaces.

Boundary stresses are simulated by evaluating the cumulative unknown shear and normal displacement discontinuities due to all boundary elements – fractures and the model boundary – on all other boundary elements. Each boundary element j exerts a stress influence on each other boundary element i . This influence can be expressed through the combined terms of influence coefficients and displacement discontinuities. The length, orientation, and location of an element j relative to element i are used to compute influence coefficients:

$$\begin{bmatrix} C_{ss}^{ij} & C_{sn}^{ij} \\ C_{ns}^{ij} & C_{nn}^{ij} \end{bmatrix}. \quad [2.31]$$

Each coefficient represents the shear or normal stress (first subscript) acting on the midpoint of the i th element due to a constant unit shear or normal (second subscript) displacement at the midpoint of the j th element. The relationship between boundary stresses b_s and b_n , influence coefficients, and displacement discontinuities is:

$$\begin{bmatrix} b_s^i \\ b_n^i \end{bmatrix} = \begin{bmatrix} C_{ss}^{ij} & C_{sn}^{ij} \\ C_{ns}^{ij} & C_{nn}^{ij} \end{bmatrix} \begin{bmatrix} D_s^j \\ D_n^j \end{bmatrix}. \quad [2.32]$$

Using the principle of superposition, the cumulative influence of the shear and normal displacement discontinuities of all j elements on the i th element is:

$$\left. \begin{aligned} b_s^i &= \sum_{j=1}^N C_{ss}^{ij} D_s^j + \sum_{j=1}^N C_{sn}^{ij} D_n^j \\ b_n^i &= \sum_{j=1}^N C_{ns}^{ij} D_s^j + \sum_{j=1}^N C_{nn}^{ij} D_n^j \end{aligned} \right\} i = 1 \text{ to } N. \quad [2.33]$$

Equation [2.33] results in $2N$ simultaneous linear equations for $2N$ unknowns for each element i .

The influence coefficient matrix is calculated in several steps (Figure 2.11). First, stress components are computed in the \bar{x} , \bar{y} coordinate system using the analytical solution described in Crouch and Starfield (1983, p. 81). Because the local reference frame is not convenient for other computations, the stress components are returned to the global x, y system using the general transformation equations:

$$\begin{aligned}\sigma_{xx} &= \sigma_{\bar{x}\bar{x}} \cos^2 \beta - 2\sigma_{\bar{x}\bar{y}} \sin \beta \cos \beta + \sigma_{\bar{y}\bar{y}} \sin^2 \beta \\ \sigma_{xy} &= (\sigma_{\bar{x}\bar{x}} - \sigma_{\bar{y}\bar{y}}) \sin \beta \cos \beta + \sigma_{\bar{x}\bar{y}} (\cos^2 \beta - \sin^2 \beta) . \\ \sigma_{yy} &= \sigma_{\bar{x}\bar{x}} \sin^2 \beta + 2\sigma_{\bar{x}\bar{y}} \sin \beta \cos \beta + \sigma_{\bar{y}\bar{y}} \cos^2 \beta\end{aligned}\quad (2.34)$$

This results in a set of six influence stress components (σ_{xxs}^{ij} , σ_{xsn}^{ij} , σ_{yys}^{ij} , σ_{yyn}^{ij} , σ_{xys}^{ij} , and σ_{xyn}^{ij}) due to a constant unit shear or normal displacement discontinuity at element j , represented by the subscripts s and n for each component. The shear or normal stress on each element i is computed using another coordinate transformation. Here, the influence stress components are transformed to shear and normal influence coefficients using Equation [2.28]. For example, the shear stress influence acting on the i th element due to the unit normal displacement discontinuity of the j th element is represented by C_{sn}^{ij} using the transformation equation:

$$C_{sn}^{ij} = \frac{(\sigma_{yyn}^{ij} - \sigma_{xsn}^{ij}) \sin 2\beta^i}{2} + \sigma_{xyn}^{ij} \cos 2\beta^i . \quad (2.35)$$

The actual boundary stresses due to the influences of all boundary elements are computed by re-arranging Equation [2.33] and solving for the unknown displacement discontinuities. Once the actual displacement discontinuities (D_s^j and D_n^j) are evaluated, only influence stress components (σ_{xxs}^{ij} , σ_{xxn}^{ij} , σ_{yys}^{ij} , σ_{yyn}^{ij} , σ_{xys}^{ij} , and σ_{xyn}^{ij}) are required to compute actual stresses. The full stresses for each boundary element i are obtained by returning the resolved remote stresses:

$$\begin{aligned}\sigma_{xx}^i &= P_{xx} + \sum \sigma_{xxs}^{ij} D_s^j + \sum \sigma_{xxn}^{ij} D_n^j \\ \sigma_{xy}^i &= P_{xy} + \sum \sigma_{xys}^{ij} D_s^j + \sum \sigma_{xyn}^{ij} D_n^j . \\ \sigma_{yy}^i &= P_{yy} + \sum \sigma_{yys}^{ij} D_s^j + \sum \sigma_{yyn}^{ij} D_n^j\end{aligned}\quad [2.36]$$

Because D_s^j and D_n^j represent the cumulative shear and normal displacement discontinuities for boundary element j , new stresses can be computed for any location within the model domain. Influence stress components at the midpoints of boundary elements in the observation grid are computed using the analytical solution in Crouch and Starfield (1983, p. 81). Observation stresses are then obtained in the same manner as actual boundary stresses using Equation [2.36].

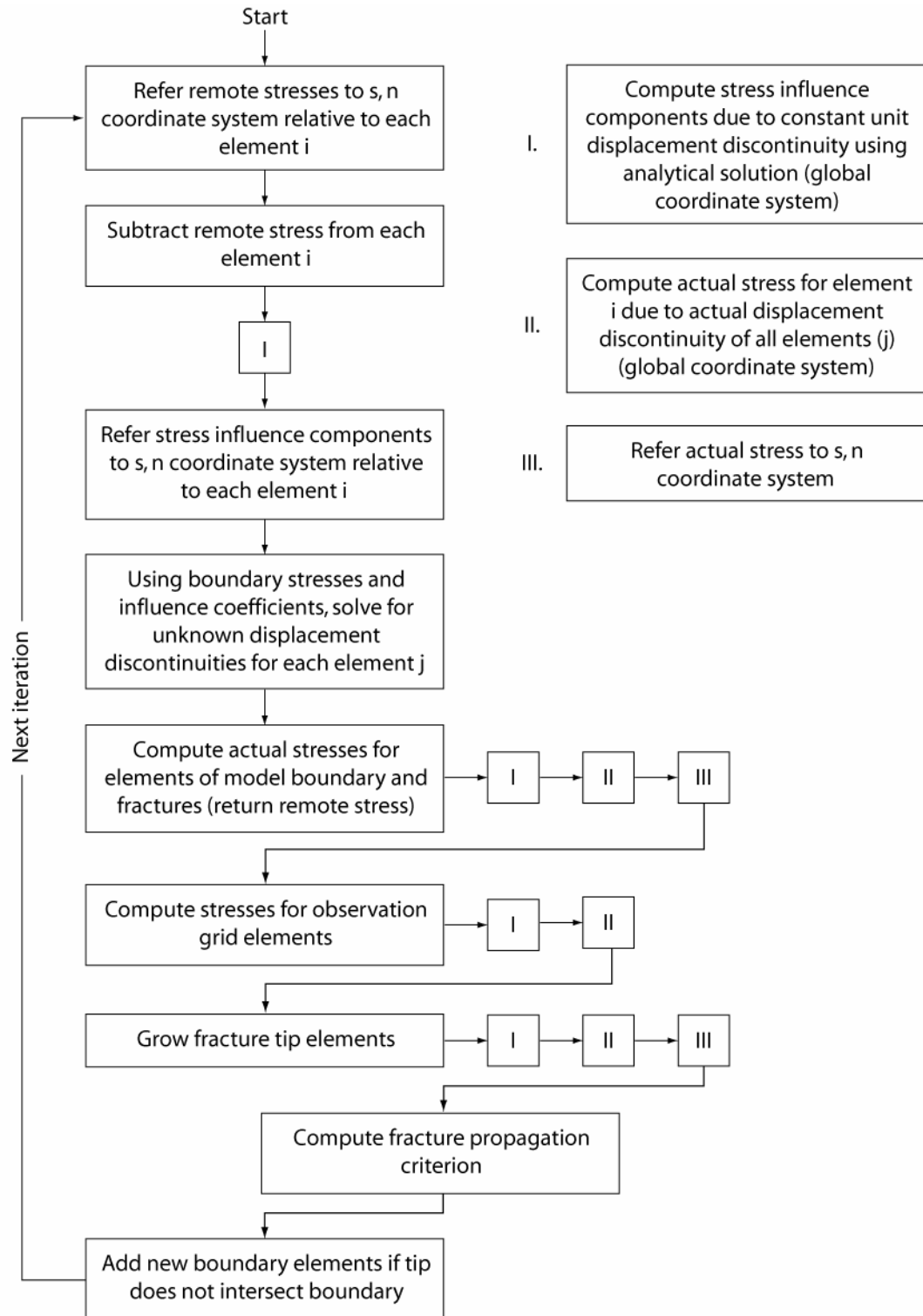


Figure 2.11 Flowchart describing simulation of stresses using the displacement discontinuity method and FRAC2D software.

2.7 Model Validation

Validation experiments for the model were conducted with increasing complexity in the boundary conditions. A simple test is described. A single fracture was placed within a small box boundary. A uniform left-lateral stress field was created with no remote stress ($\sigma_{xx} = 0$, $\sigma_{yy} = 0$, $\sigma_{xy} = -0.5$ MPa). Mean stresses due to the boundary stresses and the fracture were simulated using the displacement discontinuity method. Simulated mean stresses were consistent with expected results (Figure 2.12).

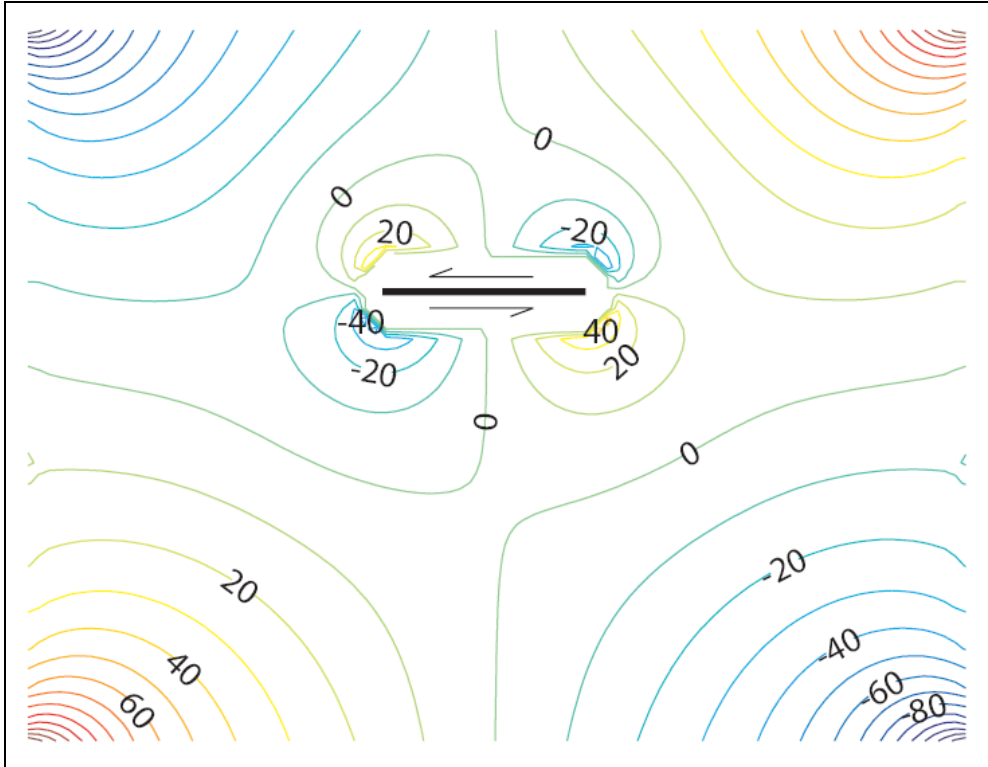


Figure 2.12 Validation of simple box with left-lateral shear ($\sigma_{xx} = 0$, $\sigma_{yy} = 0$, $\sigma_{xy} = -0.5$ MPa).

3 Methods

The study area is in the Ronne-Filchner Ice Shelf, Antarctica. All data are obtained from available datasets and remote-sensed imagery. The model data include digitized fracture geometries and ice shelf stresses derived from velocity gradients and ice thickness. All data sets and derived products are presented in a polar stereographic projection with a standard latitude of 71S, central meridian at 0E, and origin at the south pole. Where necessary, data were interpolated to a regular grid with orthogonal x - and y -axes in a horizontal plane and 1-km grid spacing. Methods include a description of the ice shelf and structural map, derivation of stresses, model inputs, and model outputs.

3.1 Ronne-Filcher Ice Shelf

The Ronne-Filchner Ice Shelf (Figure 3.1), the second largest ice shelf in Antarctica, is one of several large floating ice masses through which ice that discharges from the West Antarctic Ice Sheet flows. Together, these shelves have an area of 487,000 km² (Sandhager et al., 2004), slightly larger than the areas of Oregon and Washington combined. The Ronne Ice Shelf (RIS) lies to the west of Berkner Island, an ice rise separating it from the Filchner Ice Shelf. Six ice streams drain the West Antarctic Ice Sheet (WAIS) into the RIS – Evans, Carlson Inlet, Rutford, Institute, Möller, and Foundation Ice Streams. Ice velocities range from 200 m/year near the lateral margins to 1.4 km/yr near the center of the shelf front (Joughin and Padman,

2003). The study area extends through the outflow of the Evans Ice Stream from near the tip of the Fowler Peninsula to the shelf front.

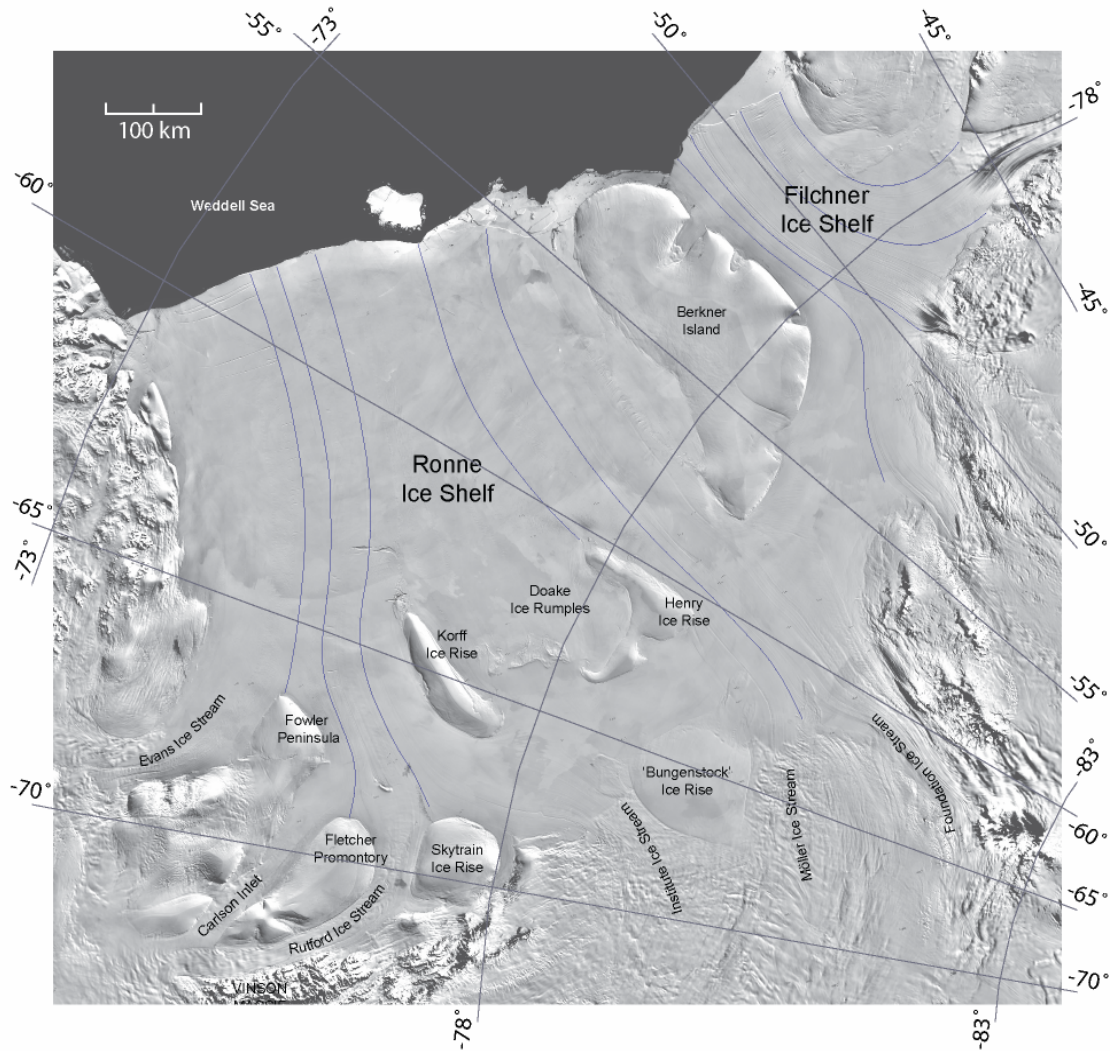


Figure 3.1 MODIS mosaic of Antarctica (Haran et al., 2005) showing Ronne-Filchner Ice Shelf. Berkner Island (upper center) separates the Ronne Ice Shelf to the west from the Filchner Ice Shelf to the east. Solid lines aligned with flow direction separate ice stream outflows.

The ice shelf is composed of ices of two origins—upper meteoric ice formed by snow accumulation, and lower accreted marine ice. The thickness of the RIS varies from more than 2000 m where the ice begins to float to between 50 and 200 m near the

seaward front (Lythe et al., 2000; Sandhager et al., 2004). Lateral differences arise due to spatial variations in ice inflow, basal melting, and strain rates. In general, ice thins as it flows toward the shelf front due to longitudinal stretching and basal melting. Basal melting is spatially variable but generally highest at the grounding lines. The fresh water released through basal melting rises buoyantly along the slope of the ice shelf. As it rises, the water becomes supercooled and refreezes, forming tiny platelets in the water column that accrete to the ice shelf base as marine ice (Jenkins and Doake, 1991). Near the shelf front, basal melting dominates and the marine ice layer thins to near-zero thickness.

The spatial distribution of this two-layer composition may have an effect on the ice rheology, which governs fracture propagation. However, for the fractures considered here, the influence of marine ice on lateral fracture propagation may be minimal. In the region immediately downstream of Fowler Peninsula, it is unlikely that crevasses penetrate the full thickness of the ice shelf; vertical arrest likely occurs above the marine ice layer. Nearer to the shelf front where rifts penetrate the full ice thickness, marine ice is largely absent due to basal melting processes.

3.2 Structural Map

A feature map of the Ronne-Filchner Ice Shelf (Figure 3.2 Figure 3.3) was developed from the MODIS Mosaic of Antarctica (MOA) image map (Haran et al., 2005; grid scale 125 m). The mosaic is a composite of MODIS images taken between 20 November 2003 and 29 February 2004. The resolution and use of many images with

different sun illumination angles used to construct the MOA made it possible to trace many features, including large fractures, streaklines, and former shear margins. Streaklines are surface undulations that originate in the grounded ice sheet as ice flows over variations in basal traction, or relief. The feature map provides a flow history over hundreds of years in the ice shelf, and delineates flow provenance through the mapping of distinctive flow features observed in outlet glaciers and ice streams.

Fractures, streaklines, and relict margins were digitized using Adobe Illustrator. Streaklines appear as shadows cast along their flanks. Fractures appear either as sharp, sunlit/shadowed faces or as shadows cast within sagging snow bridges (Merry and Whillans, 1993). Small fractures, or those well-covered by snow, are not visible. The closely-spaced fractures in a chaotic shear margin leave a signature in the shadows cast along the margin track (Merry and Whillans, 1993). Slope breaks, such as at the margins of ice rises, are also visible as shadows cast along the feature trace. Features were digitized at the dark/light boundary. All fractures were digitized at 5x magnification. All other features including boundaries, ice rises, streaklines, and grounding lines, were digitized at 2.5x magnification. The digitized points were assigned coordinates in the MOA projection. Features are in general agreement with the USGS map of Antarctica (Ferrigno et al., 2005).

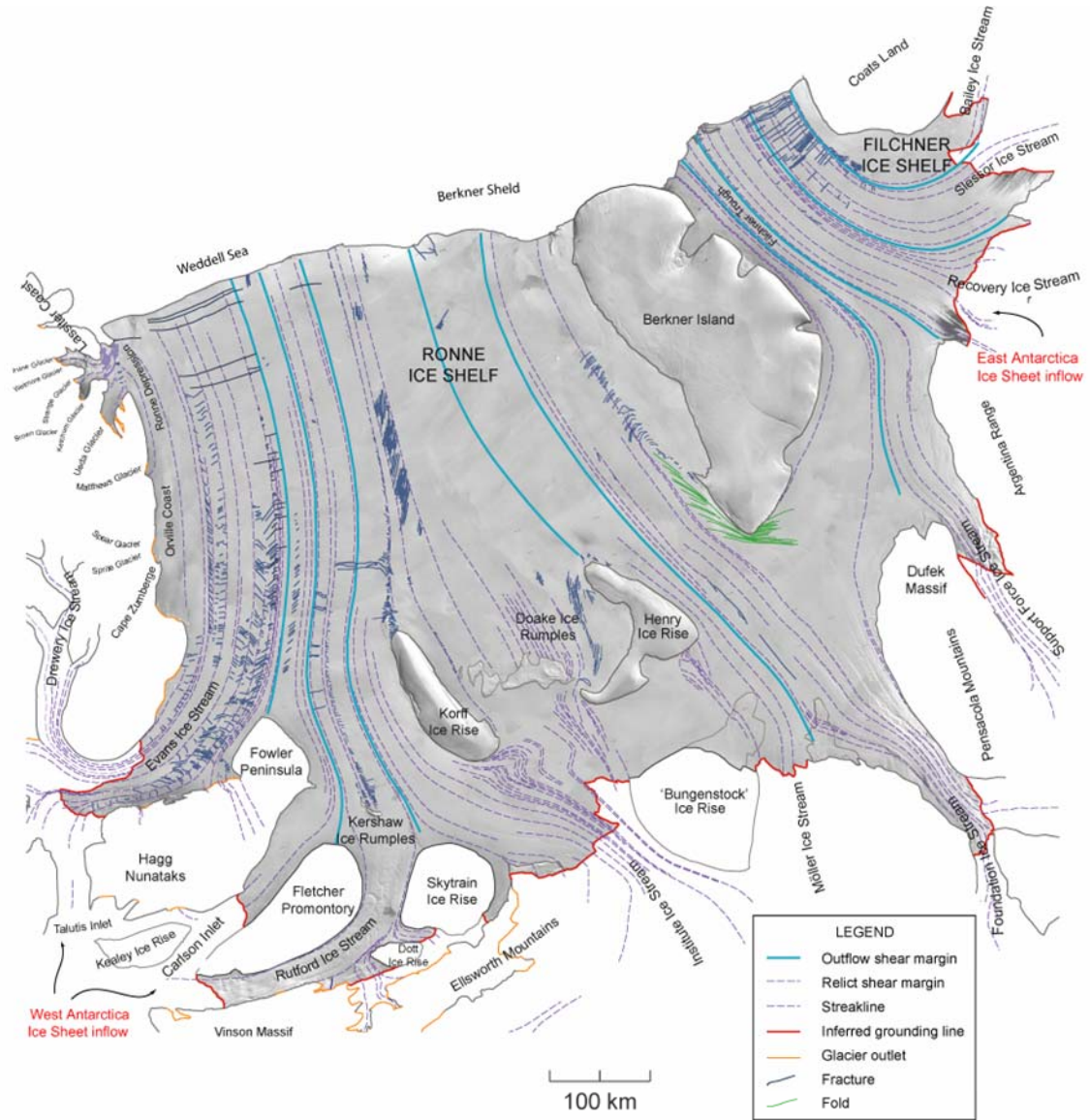


Figure 3.2 Digitized structural map of Ronne-Filchner Ice Shelf, based on MOA (Haran et al., 2005). MODIS image visible under digitization overlay.

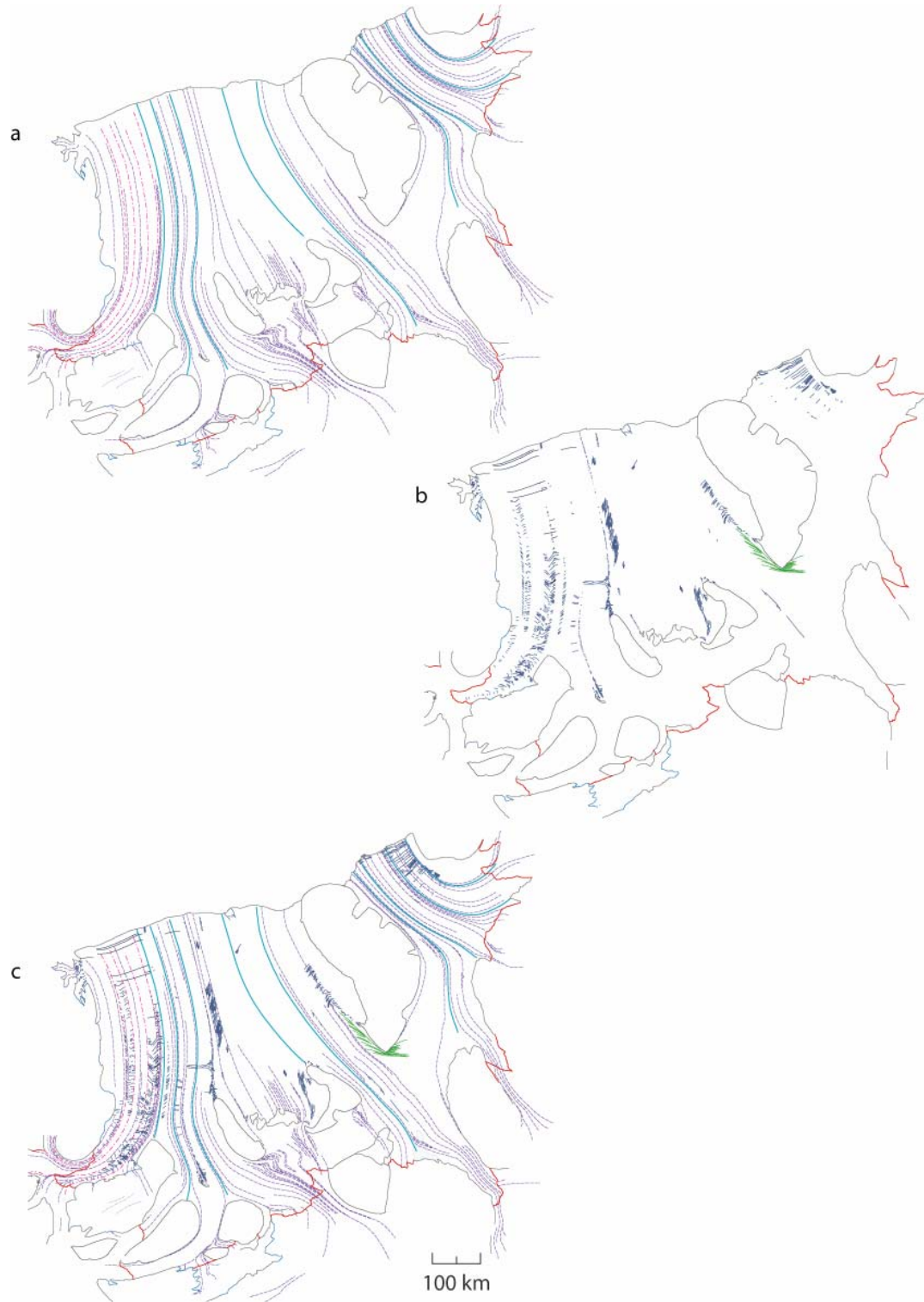


Figure 3.3 Digitization of structural map, based on MOA (Haran et al., 2005). (a) Structural boundaries. Solid lines separate ice from different ice streams (major suture zones), dash-dotted lines represent former shear margins, light dotted lines represent other streaklines, and the solid lines transversing ice streams represent the inferred grounding lines. (b) Fracture geometries. (c) Structural boundaries and fractures.

Evans Ice Stream

The Evans Ice Stream is the fastest-flowing outlet glacier entering the RIS and has the largest influx of ice, 35.7 ± 3.6 Gton/yr (Joughin and Padman, 2003). The drainage basin of the Evans Ice Stream includes ice flowing from the mountains of Ellsworth Land, of which the Drewery Ice Stream feeds the Evans, and ice originating near the ice divides with the Pine Island Glacier and Rutford Ice Stream (Figure 3.4).

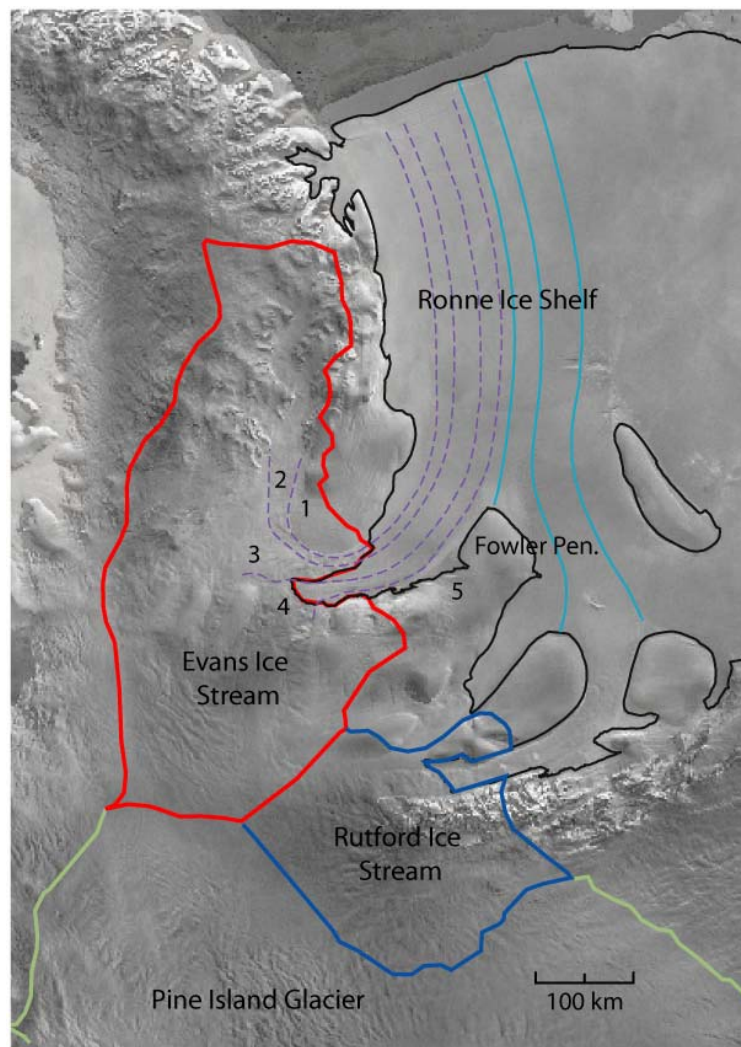


Figure 3.4 Evans Ice Stream drainage basin drawn over the MOA with Radarsat Antarctic Mapping Project Antarctic Mapping Mission 1 amplitude image, based on delineation of Rignot (2001) with updates from the present work.

Five primary tributaries of the Evans Ice Stream are identified, labeled from west to east (Figure 3.5 and Figure 3.6). **Tributary 1:** Ice flows south from the mountains to form the westernmost shear margin of the Ronne Ice Shelf. While the upper tributary has a relatively small ice flux to the shelf, ice flows into it from outlet glaciers on the Orville and Lassiter Coasts (Figure 3.2). **Tributary 2:** The Drewery Ice Stream flows south from the mountains of Ellsworth Land. **Tributary 3:** This tributary flows east with two substantial relict shear margins. To the west, the ice flows past a topographic high before aligning with its neighboring tributary, the Drewery Ice Stream. To the east, ice flows along a prominent grounded feature, generating a strong shear zone with *tributary 4*. **Tributary 4:** Ice flows north from the ice divide (part of the WAIS) before abruptly turning east. **Tributary 5:** This tributary contains outflows from the eastern shear margin of the Evans Ice Stream (*5a*) and from outlet glaciers on the Hagg Nunataks and between this feature and the Fowler Peninsula (*5b*). Where the tributaries coalesce, their lateral shear margins form “suture zones” visible in the MOA. The suture zones are highly fractured and form structural boundaries in the ice. They may be traced from the grounding line into the ice shelf.

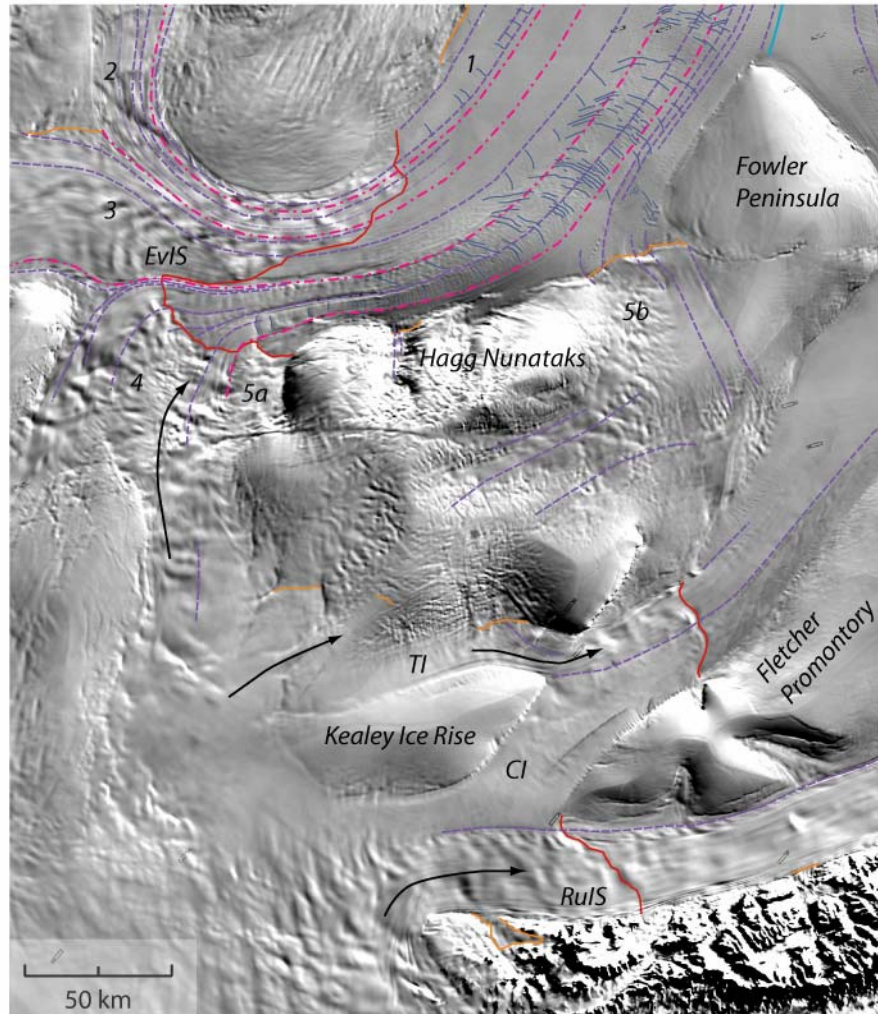


Figure 3.5 Ice flow near the grounding lines of the Evans Ice Stream (EvIS), Talutis Inlet (TI), Carlson Inlet (CI), and Rutford Ice Stream (RuIS). Tributaries of the Evans Ice Stream are numbered. Dash-dotted lines represent former shear margins, light dotted lines represent other streaklines, and the solid lines transversing ice streams represent the inferred grounding lines.

The Evans outflow passes through a narrow, tectonic gap (Jones et al., 2002; King and Bell, 1999) where it joins with another tributary as the ice begins to float. Observations of downstream fracture geometry suggest that the suture zone between these two inflows (the $3/4$ suture zone) is an important structural boundary. The grounding line is traced at the transition from a relatively hummocky to relatively

smooth surface, indicating the transition from flow over a rough bed to flow over water. Within ~30 km of the grounding line, *tributary 4* ice is compressed laterally to less than 20% its width at the grounding line. A prominent subglacial meltwater stream is expressed as a sinuous depression in the ice surface. Prominent crevasses are observed through this region. Downstream of the Fowler Peninsula, another important suture zone forms with the outflow of the Carlson Inlet.

Suture zones appear to be important structural boundaries in the ice shelf. They are observed to both initiate and arrest the propagation of large rifts. Perturbations of the fracture traces are observed where shelf-front rifts intersect these boundaries (Figure 3.6). These perturbations may be the result of differences in material properties of the ice. The suture zone between the Evans and Carlson Inlet flows is not breached by fractures until within 50 km of the shelf-front.

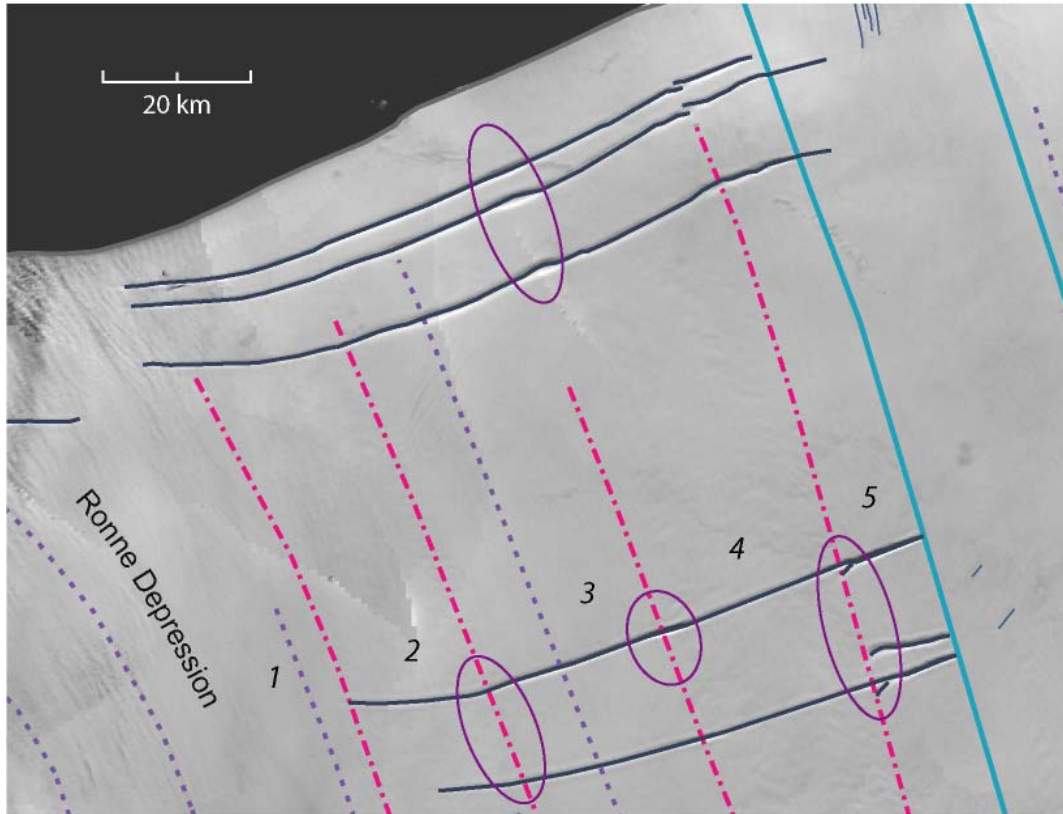


Figure 3.6 Notches in fractures near the shelf-front are interpreted as evidence of episodic fracture growth. These notches appear at changes in material properties of the ice.

The set of large, transverse fractures near the western front of the RIS (Figure 3.6) can be traced upstream if ice flow is assumed to be steady over the lifetime of ice moving from the grounding line to the shelf front. Agreement between flow features and velocity azimuths (Figure 3.7) make this a good assumption (Fahnestock et al., 2000). Tracking these features upstream allows their propagation history to be explored. The first step in that study is the classification of provinces with distinct fracture patterns within the Evans Ice Stream outflow (Figure 3.8). The provinces provide context in which to examine the growth of the large, through-cutting rifts.

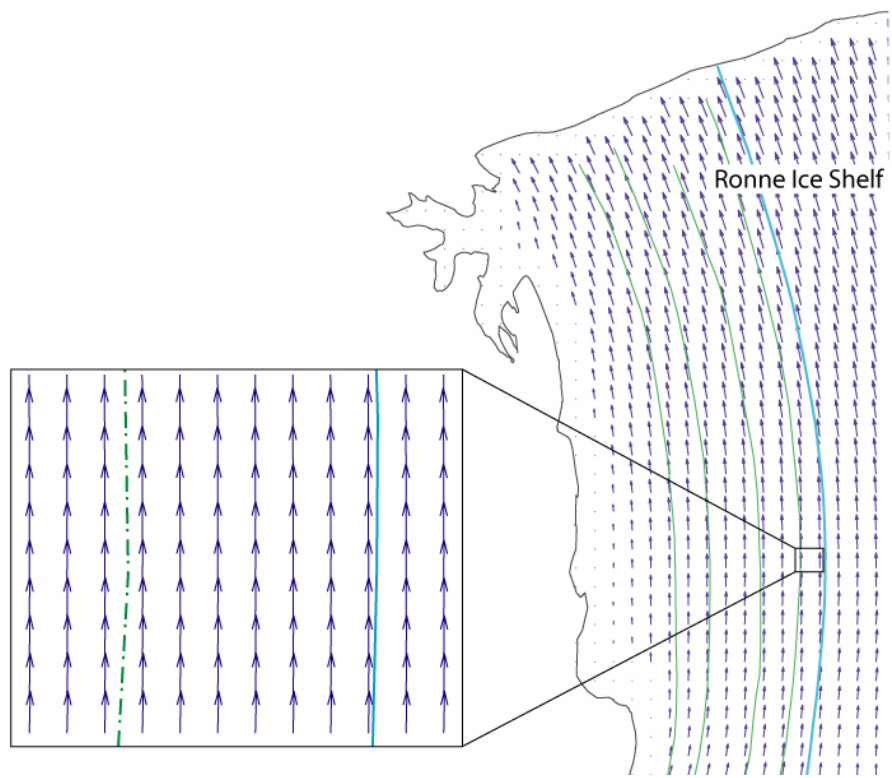


Figure 3.7 Flow features and velocity vectors in the outflow of the Evans Ice Stream.

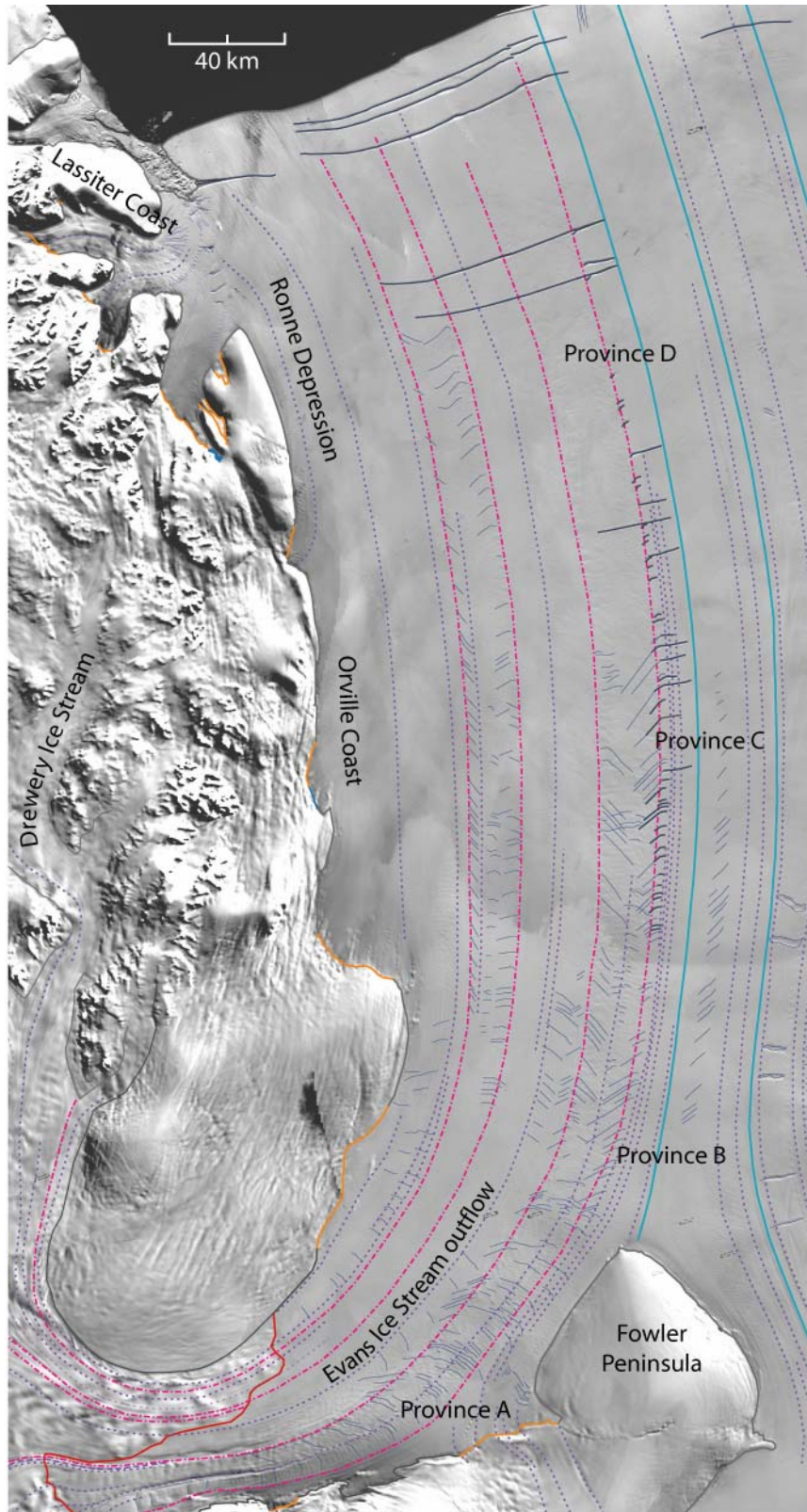


Figure 3.8 Digitized features in the outflow of Evans Ice Stream.

Province A is a chaotic region downstream of the grounding line. It is characterized by arcuate crevasses, intersecting crevasses, and relict shear margins (Figure 3.5). Shear margin fractures develop in *tributary 3* at the inboard side of the 3-4 suture zone, and become less prominent with increasing distance from the grounding line.

Province B, downstream of Fowler Peninsula, has clearly defined shear margin fractures in *tributary 4* along both margins (Figure 3.9). These younger, closely-spaced (1-2 km), upstream-pointing fractures develop in the wake of Fowler Peninsula, overprinting older crevasses. Near the downstream end of this province, the eastern fracture tips are observed to have ~1km growth normal to ice flow before crack tip arrest.

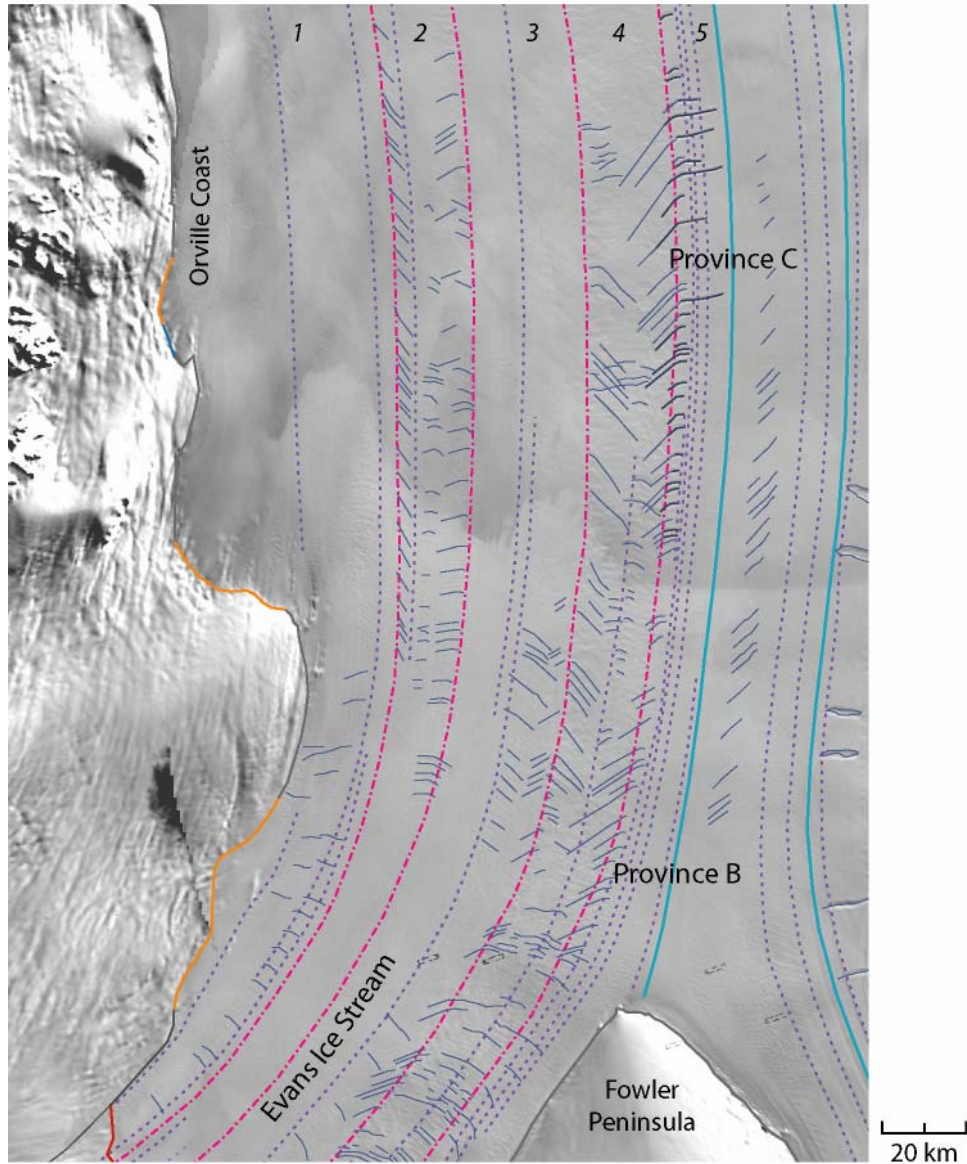


Figure 3.9 Digitized features in the outflow of Evans Ice Stream, showing provinces B and C.

In *Province C*, shear margin fractures at the 4/5 suture zone begin propagating east, normal to ice flow before arresting at the Evans-Carlson suture zone (Figure 3.9). The location is important because we can infer that a significant change in the stress field must occur here, driving the observed propagation. The 4/5 suture zone becomes an

important structural boundary. For over 100 km downstream of the first observed crack tip arrest at the Evans-Carlson suture zone, the fractures do not propagate westward through the 4/5 suture zone.

In *Province D*, the 4/5 suture zone is breached by a few large fractures, which propagate to the west (Figure 3.10). Apparent fracture spacing increases as fractures grow (10-20 km separation at the upstream end and 20-50 km separation at the downstream end). These larger fractures dominate the local stress field near the shelf front. It is inferred that nearby fractures become passive features and fill in with blowing snow. Near the shelf front, the largest fractures exceed 100 km in length.

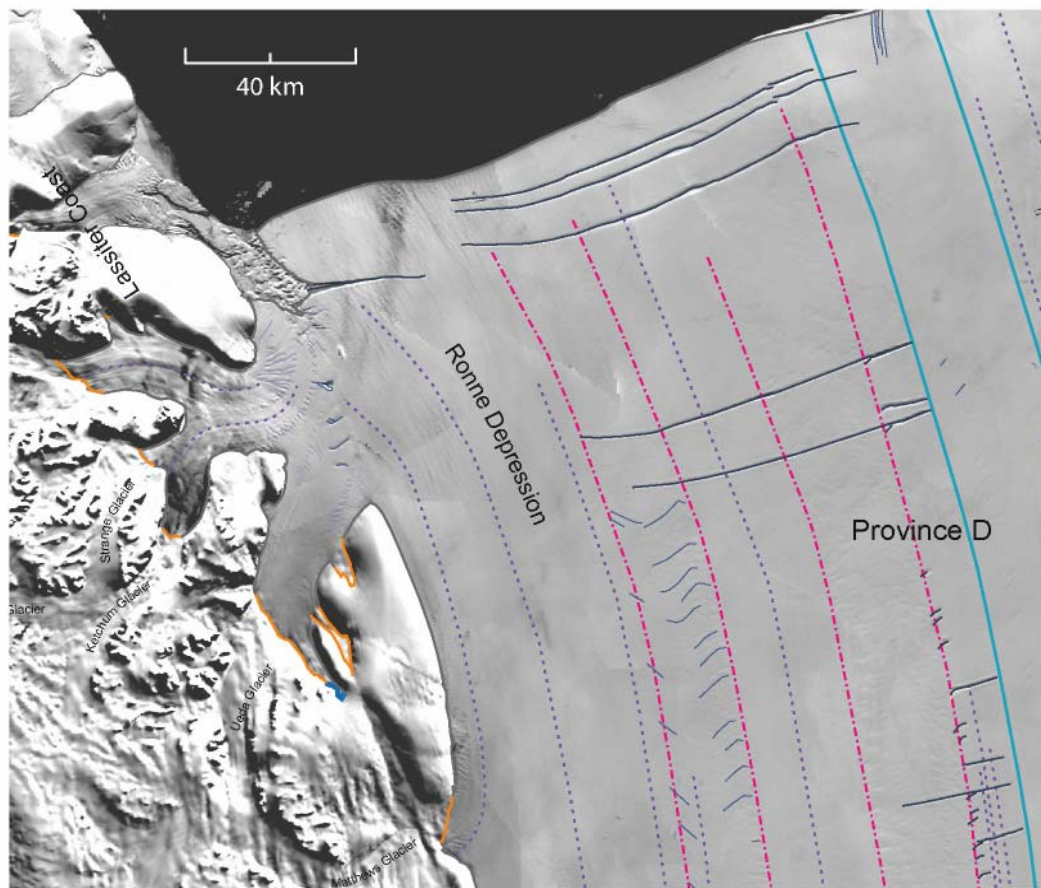


Figure 3.10 Digitized features in the outflow of Evans Ice Stream within province D.

3.3 Observed Ice Flow Used to Compute Stresses

Fractures grow according to the principal stress directions and the stress intensity at the propagating tip. These can be estimated using measured velocity gradients (strain rates) and an estimated flow-law rate factor.

Velocity Data and Strain Rates

Gridded ice velocity from Ian Joughin (UW Applied Physics Laboratory, personal communication, 2005; grid scale 1 km) was used to derive strain rates in the ice shelf. Infinitesimal strain rates were computed as gradients of the velocity field, which is a valid approximation for small displacement gradients. The infinitesimal strain rate tensor $\dot{\epsilon}_{ij}$ is expressed in terms of the partial derivatives of the velocity vector u_i :

$$\dot{\epsilon}_{ij} = \frac{1}{2} \left(\frac{\partial u_i}{\partial x_j} + \frac{\partial u_j}{\partial x_i} \right) \quad i, j = \{x, y\} . \quad [3.1]$$

The uncertainty in this simplification is the sum of the effects of the omitted higher-order terms. Mean velocity gradients were computed using differences along quadrilateral edges (Figure 3.11). For example,

$$\dot{\epsilon}_{xx} \Big|_{y=m} = \frac{\partial u_x}{\partial x} \Big|_{y=m} \cong \frac{u_x^{m,n+1} - u_x^{m,n}}{\Delta x} \quad [3.2]$$

in which Δx represents the spatial change in the x -direction and n, m are the respective indices for x, y . Strain rates for the quadrilateral centroid were obtained by taking the mean of the velocity gradients on opposite sides of the quadrilateral. For example,

$$\dot{\epsilon}_{xx}|_{\text{centroid}} = \frac{1}{2} \left(\left. \frac{\partial u_x}{\partial x} \right|_{m+1} + \left. \frac{\partial u_x}{\partial x} \right|_m \right). \quad [3.3]$$

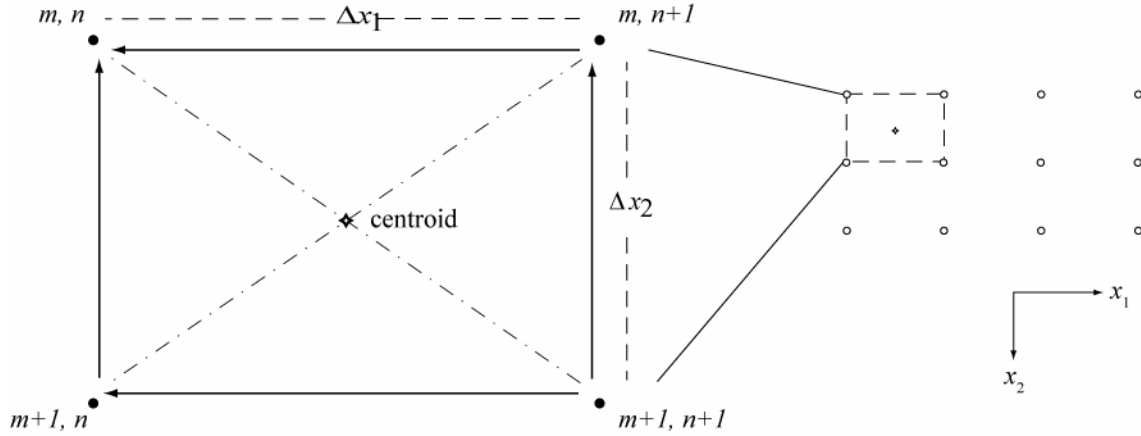


Figure 3.11 An example quadrilateral in the gridded velocity data set. Differences may be computed along edges of the quadrilateral or across diagonals. The resulting mean gradients apply at the centroid.

Other components of the strain rate tensor, for two dimensions, were computed in a similar manner. A mean shear strain rate $\dot{\epsilon}_{xy}$ was obtained by averaging $\dot{\epsilon}_{xy}$ and $\dot{\epsilon}_{yx}$ for each centroid node:

$$\dot{\epsilon}_{xy}|_{\text{centroid}} = \frac{1}{2} \left(\dot{\epsilon}_{xy}|_{\text{centroid}} + \dot{\epsilon}_{yx}|_{\text{centroid}} \right) = \frac{1}{2} \left(\left. \frac{\partial u_x}{\partial y} \right|_{\text{centroid}} + \left. \frac{\partial u_y}{\partial x} \right|_{\text{centroid}} \right). \quad [3.4]$$

The effective strain rate provides a general reference for the magnitude of deformation in the flowing ice (Figure 3.12). The effective strain rate $\dot{\epsilon}_e$ for two dimensions was computed:

$$\dot{\epsilon}_e = \left(\frac{\dot{\epsilon}_{xx}^2 + \dot{\epsilon}_{yy}^2}{2} + \dot{\epsilon}_{xy}^2 \right)^{1/2}. \quad [3.5]$$

The velocity data contain a non-random error that is an artifact of the interferometric technique used to compute velocities (Figure 3.13a). This non-random error was enhanced by the strain-rate calculations and manifests as banding in the strain rate amplitude (Figure 3.13b). The effect of this error was minimized by smoothing the raw velocity data using MATLAB's *fspecial* function and a running average (Figure 3.14). Several filter dimensions were tried and a 20 km square was the smallest useful smoothing window. The effect of the error was reduced but not removed (Figure 3.13c and Figure 3.13d).

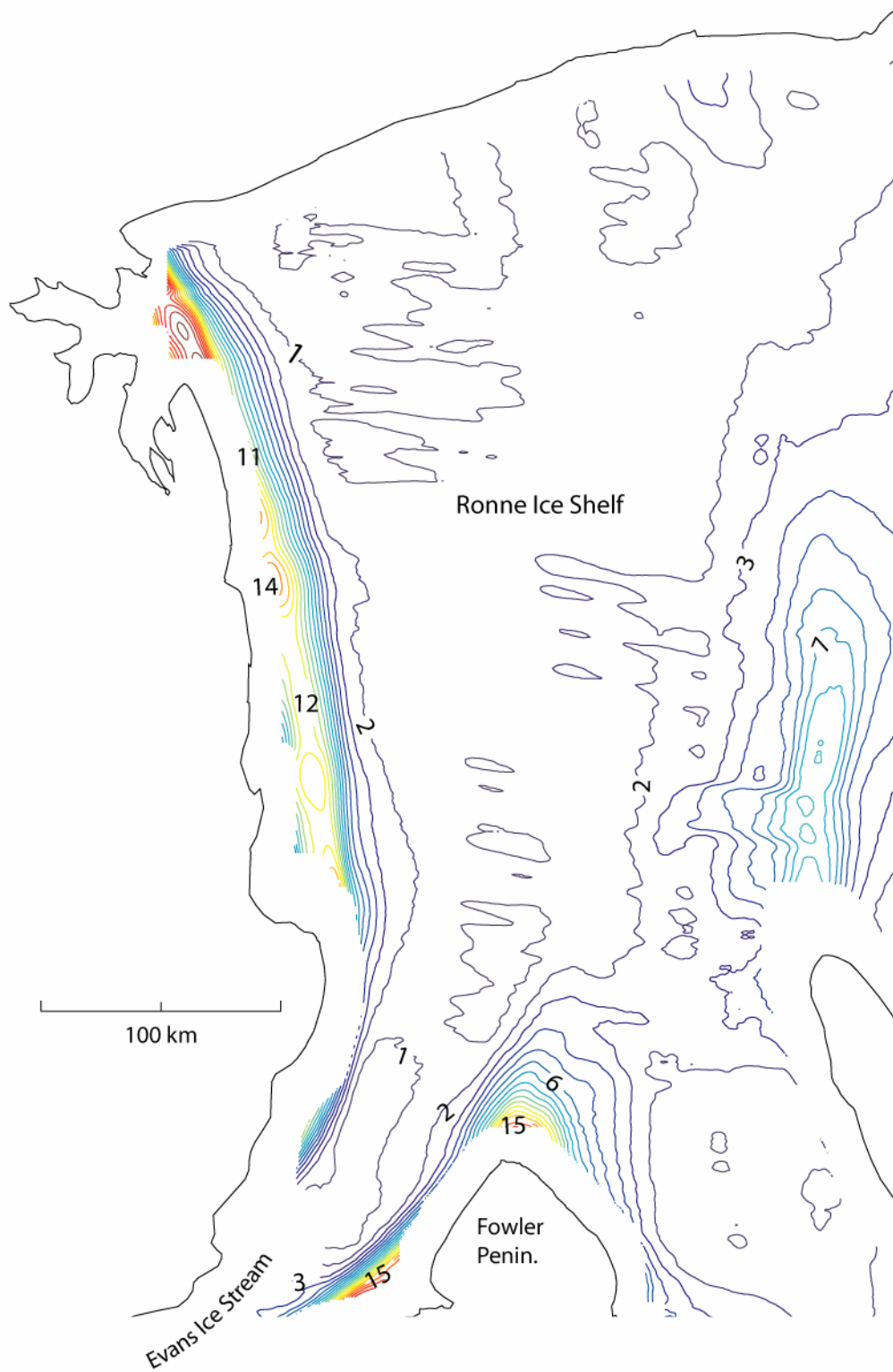


Figure 3.12 Effective strain rate map. The effective strain rate, which represents large-scale deformation within the ice shelf, was computed using Equation [3.5].

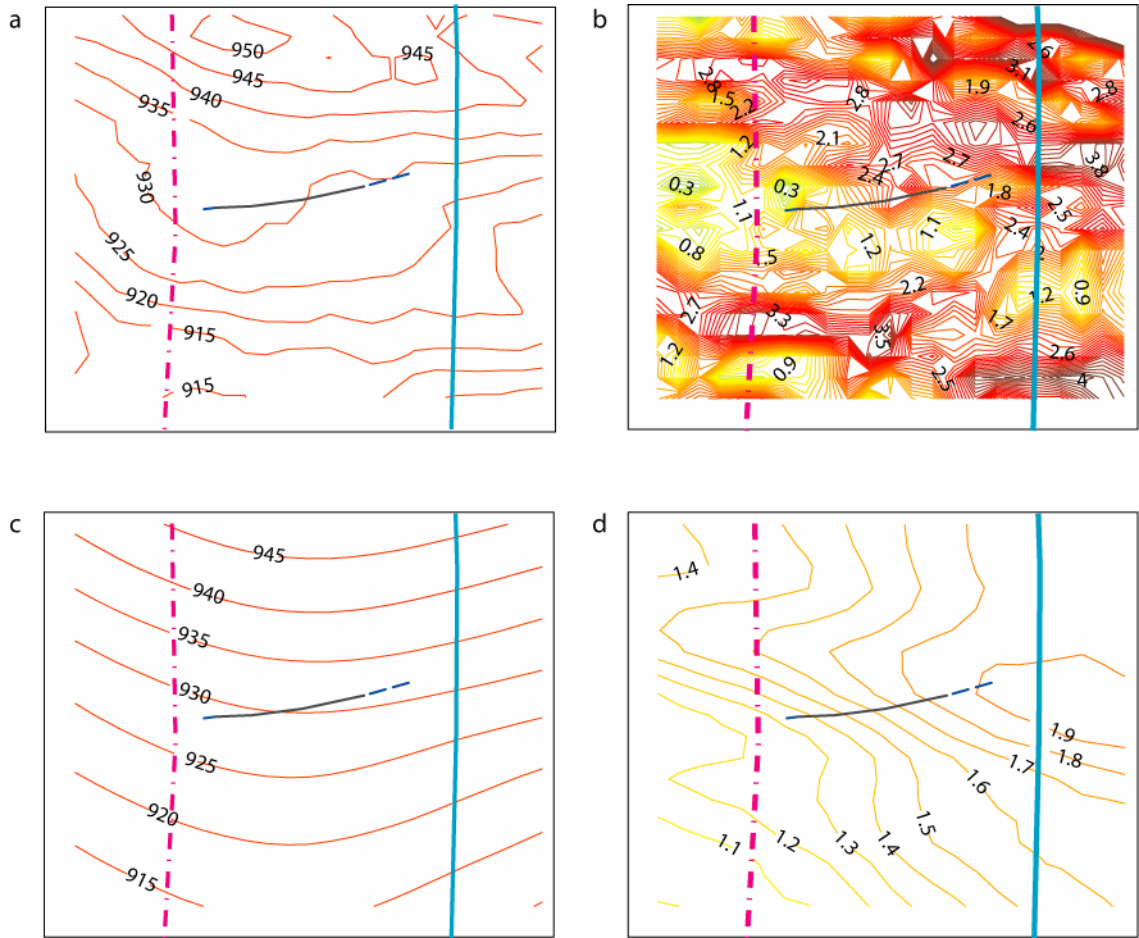


Figure 3.13 Small variations in observed speed (a) due to the interferometric technique are enhanced by strain rate calculations, leading to substantial noise in strain rates. The effective strain rate is shown here (b). A running average smoothing filter of 20-km x 20-km was applied to the velocity data (c and d). The fracture trace and suture zones drawn in each panel are for reference only.

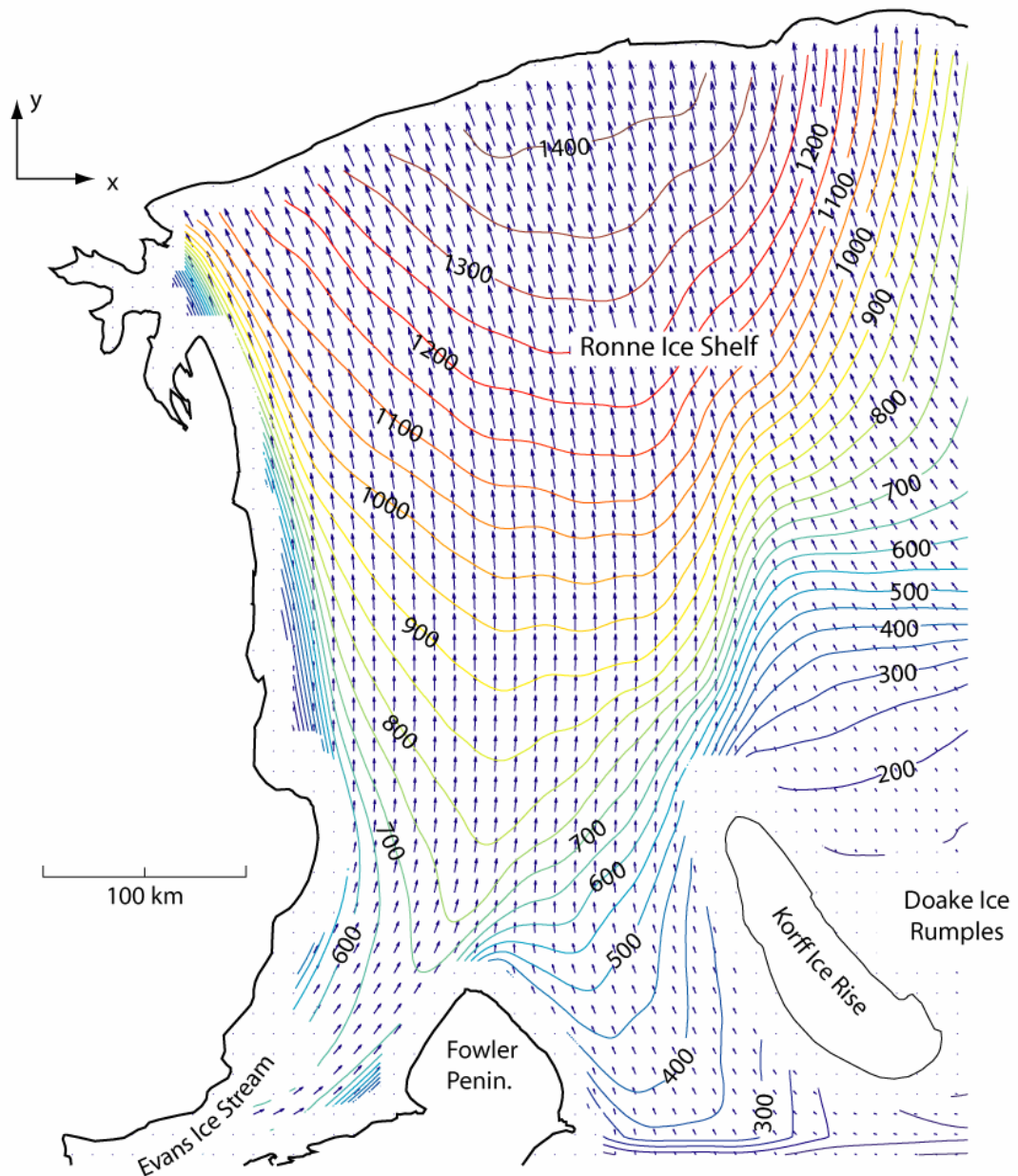


Figure 3.14 Velocity map filtered using a 20-km x 20-km smoothing filter, based on measured ice velocity (Ian Joughin, personal communication). The stippled regions near the shelf boundaries represent data loss due to the velocity smoothing technique.

Deviatoric Stresses

Strain rates are related to deviatoric stresses in the ice according to a constitutive relation often called a flow law. The rate at which ice deforms depends on its temperature, and other less well-understood parameters. Nye's generalization of Glen's flow law for glacier ice (forward flow law) is:

$$\dot{\epsilon}_{ij} = A\tau_e^{n-1}\tau_{ij} , \quad [3.6]$$

in which A is the temperature-dependent flow law rate factor, n is typically taken as 3, τ_{ij} is deviatoric stress, and τ_e is the effective deviatoric stress, a scalar quantity (Hooke, 1998, p. 14-15; Nye, 1953, 1957). The ice is assumed to be incompressible and isotropic. To derive stresses using computed strain rates, the inverse flow law is used:

$$\tau_{ij} = B\dot{\epsilon}_e^{1/n-1}\dot{\epsilon}_{ij} , \quad [3.7]$$

in which B is the inverse rate factor and $\dot{\epsilon}_e$ is the effective strain rate.

The constitutive relation cannot be frame dependent. That is, the strain rates in a given direction within glacier ice depend not only on the stresses acting in that direction but also upon the stress state as a whole. Thus, the forward and inverse flow laws involve the products, $\tau_e^{n-1}\tau_{ij}$ and $\dot{\epsilon}_e^{1/n-1}\dot{\epsilon}_{ij}$, respectively, in which the effective strain rate $\dot{\epsilon}_e$ is defined in [3.5] and the effective deviatoric stress τ_e , for two dimensions, is defined:

$$\tau_e = \left(\frac{\tau_{xx}^2 + \tau_{yy}^2}{2} + \tau_{xy}^2 \right)^{1/2}. \quad [3.8]$$

The rate factor is a measure of the viscosity of the ice and depends on temperature, ice fabric, and other factors. Using the velocity data set in the present work, Larour et al. (2005) employed an inverse control method to infer B for the Ronne Ice Shelf. Across the RIS, depth-averaged B was found to vary between 300 and 900 $\text{kPa a}^{1/3}$, with an average value of 760 $\text{kPa a}^{1/3}$ at the western front of the ice shelf. In the present work, a uniform value of 760 $\text{kPa a}^{1/3}$ is used.

Principal Stresses

Principal stresses σ_1 and σ_2 represent the greatest and least normal stresses, respectively, on a surface. Principal stresses may be extensive or compressive; shear tractions are not present. Mode I fractures have maximum displacement in the direction of most extensive principal stress and propagate orthogonal to this direction. In the present work, principal stresses are derived using deviatoric stresses, which better represent the stress magnitudes that affect deformation within the ice but do not modify the principal stress directions.

Principal stresses and directions must satisfy the eigenvalue problem:

$$\left(\tau_{ij} - \lambda_n I \right) \mathbf{x}_n = 0 \quad \left. \vphantom{\left(\tau_{ij} - \lambda_n I \right) \mathbf{x}_n = 0} \right\} n = 1, 2 \quad [3.9]$$

in which λ_1 (λ_2) represents the maximum (minimum) principal stress magnitude and x_1 (x_2) is the vector corresponding to the respective principal stress direction. Written out, equations for the individual components are:

$$\tau_1 = \frac{\tau_{xx} + \tau_{yy}}{2} + \sqrt{\left(\frac{\tau_{xx} - \tau_{yy}}{2}\right)^2 + \tau_{xy}^2} \quad [3.10]$$

$$\tau_2 = \frac{\tau_{xx} + \tau_{yy}}{2} - \sqrt{\left(\frac{\tau_{xx} - \tau_{yy}}{2}\right)^2 + \tau_{xy}^2} \quad [3.11]$$

$$\tan 2\theta_1 = \frac{2\tau_{xy}}{\tau_{xx} - \tau_{yy}} . \quad [3.12]$$

in which θ_1 is the principal stress direction for τ_1 . θ_2 is orthogonal to θ_1 .

Full Stresses

The full glaciological stress is the sum of the deviatoric stress and the lithostatic stress:

$$\sigma_{ij} = \tau_{ij} + \frac{1}{3}\sigma_{kk}\delta_{ij} , \quad [3.13]$$

in which repeated indices are understood to be summed and δ_{ij} is the Kronecker delta.

The mean normal stress is taken to be the overburden pressure,

$$P(z) = P_0 + g \int_z^{z_s} \rho(z) dz \quad [3.14]$$

in which P_0 is the surface pressure, ρ is the ice density, g is acceleration due to gravity, z_s is the surface elevation, and z is the depth below the surface. For the present work, a single mean value was required at each grid point. The engineering hydrodynamics practice of using $\frac{2}{3}$ the ice thickness was followed such that

$$P(x, y) = \frac{2}{3} \rho g H \quad [3.15]$$

in which H is the ice thickness and the depth-integrated density ρ is 910 kg m^{-3} (Figure 3.15). Ice shelf thickness H was obtained from the BEDMAP data set (Lythe et al., 2000). The data were interpolated using cubic interpolation to match the 1-km grid spacing of stresses (Figure 3.16). Conservation of angular momentum requires symmetry in the stress tensor $\sigma_{ij} = \sigma_{ji}$. Thus, the expanded full stress tensor is

$$\begin{bmatrix} \sigma_{xx} & \sigma_{xy} \\ \sigma_{xy} & \sigma_{yy} \end{bmatrix} = \begin{bmatrix} \tau_{xx} + \frac{2}{9} \rho g H & \frac{1}{2} (\tau_{xy} + \tau_{yx}) \\ \frac{1}{2} (\tau_{xy} + \tau_{yx}) & \tau_{yy} + \frac{2}{9} \rho g H \end{bmatrix}. \quad [3.16]$$

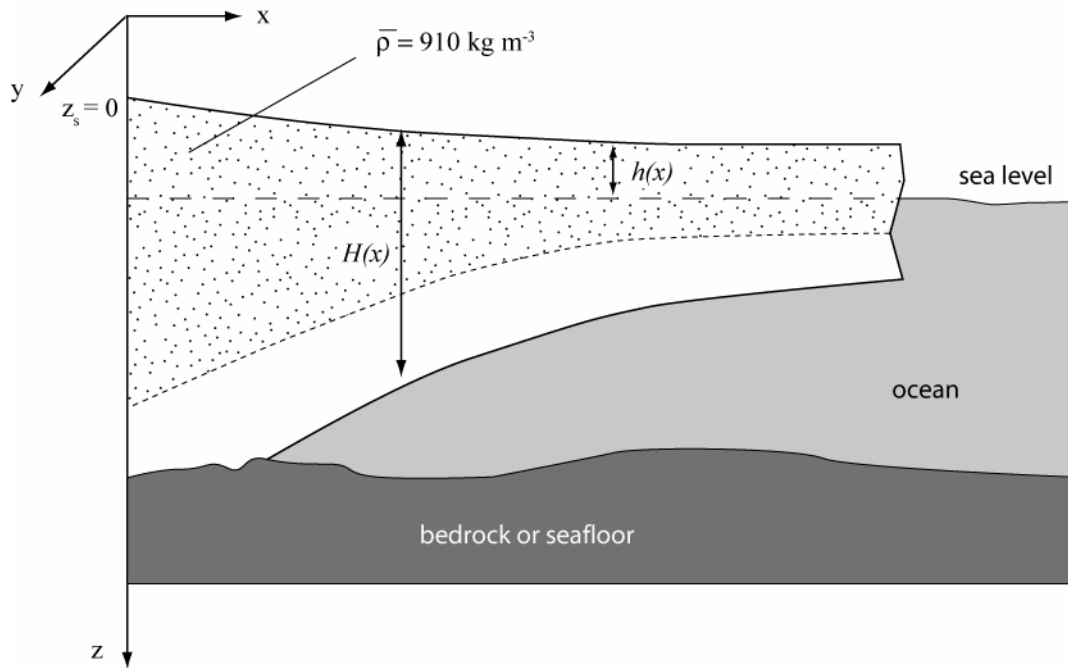


Figure 3.15 Side view of an ice shelf of non-uniform thickness (after Paterson, 1994, p. 293). The stippled area represents the upper two-thirds of the ice-shelf. $H(x)$ is the ice thickness, $h(x)$ is the surface elevation above sea level, and $\bar{\rho}$ is the depth-integrated ice density.

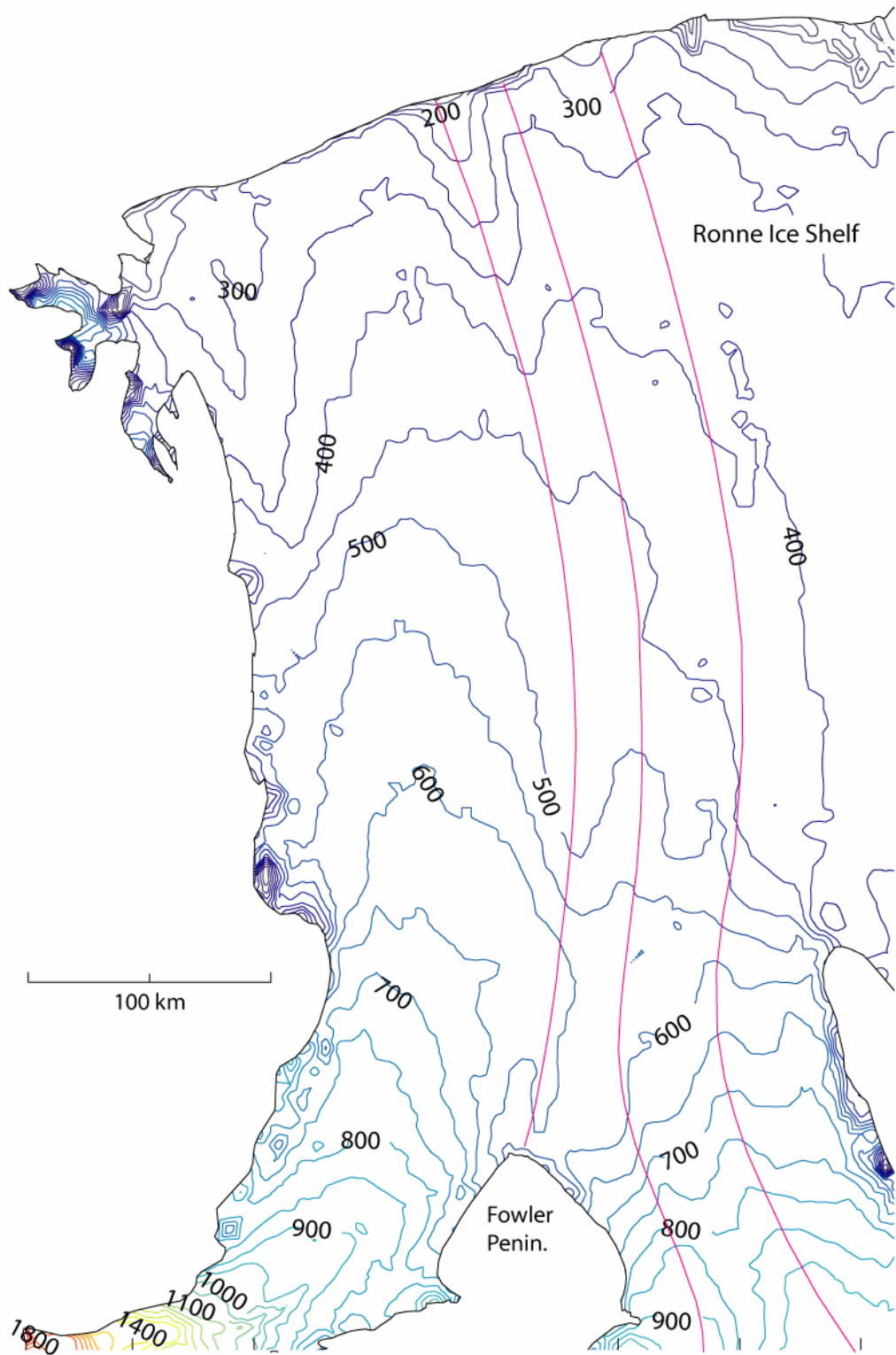


Figure 3.16 Ice thickness map of western Ronne Ice Shelf from BEDMAP (Lythe et al., 2000). Solid lines aligned with the flow direction separate different ice stream outflows. From left to right (west to east), the ice stream outflows are Evans, Carlson Inlet, Rutford, and Institute.

3.4 Model Inputs

Model inputs include boundary elements, boundary and remote stresses, elasticity constants, fracture toughness, and an observation grid.

Discretization of Model Domain

Each boundary element is defined using beginning and ending x - and y - coordinates in the global Cartesian reference frame. The boundary discretization required a step size greater than the grid spacing of computed stresses. Experiments showed that the minimum step size for boundary elements should be twice the grid spacing, or about 2 km. Discretization was automated using the step size and length of a model domain side or of a fracture boundary element. The selection of boundary geometry was guided by fracture geometries, principal stresses, material boundaries, and the spatial resolution of data sets. The DDM permits any geometry for the outer boundary. To minimize memory requirements, a simple box geometry was imposed with specified corner coordinates. Boundaries were selected to minimize the effects of the residual (after smoothing) non-random error in the stress field.

Two MATLAB tools, customizable through user input, were developed to facilitate experiment design. One tool provides a preview of the model domain or surrounding region, showing mean stress, components of the stress tensor, principal stresses, effective strain, or ice thickness, with an overlay of fracture geometry and ice shelf structural boundaries (*preview_boundary.m*, Appendix C). The other tool generates

boundary elements, computes fracture and boundary stress conditions, and generates the model domain grid required by Frac2D (*get_export.m*, Appendix C).

Boundary Stress Conditions

Boundary stress conditions must be specified such that modeled stresses throughout the domain resemble stresses in the ice shelf and in some cases, to determine the stress magnitude required to initiate propagation. To accomplish these objectives, principal deviatoric stresses $\{\tau_1, \tau_2\}$ may be scaled:

$$\{\tau_1, \tau_2\}_{\text{new}} = \mathfrak{S} \times \{\tau_1, \tau_2\} \quad [3.17]$$

in which \mathfrak{S} is the scaling factor. This method does not change the orientations of principal axes.

The scaling of deviatoric stresses during model initialization implicitly scales the full stresses as well. The full normal stresses are modified by amounts that are typically less than the scaling factor \mathfrak{S} (Table 3.1, Table 3.2). The effect on longitudinal stresses is greater due to the relatively greater magnitude of τ_{yy} compared to τ_{xx} in the ice shelf. The effect on σ_{yy} of reducing principal stresses by a factor \mathfrak{S} can be approximated by:

$$\{\sigma_{yy}\}_{\text{new}} = \left(\frac{\mathfrak{S}+1}{2}\right)\sigma_{yy} . \quad [3.18]$$

The effect on σ_{xx} depends on the sign and magnitude of the deviatoric stress τ_{xx} . If τ_{xx} is positive, then reducing it will decrease σ_{xx} by a small amount, typically 1-2%.

will increase by a similar amount if τ_{xx} is negative. The stress conditions for a boundary element are obtained for the midpoint of each element by averaging the stresses at the grid points nearest to the start and end coordinates of the element. Several other averaging methods were tried but did not improve the approximation of mean stress conditions for the midpoint. The stress tensor for the midpoint is resolved to the plane of the element by transforming it to shear and normal stresses acting on the boundary element.

Table 3.1 Example of stress magnitude changes for a location of minimal shear and positive τ_{xx} , using different scaling factors. (The data were taken from a grid point in the western part of the model domain for Experiment 2; Figure 4.9).

	<i>factor</i>	τ_1	τ_2	τ_{xx}	τ_{yy}	τ_{xy}	σ_{xx}	σ_{yy}
Stress Magnitude, kPa	<i>1.00</i>	1196	138	144	1191	-78	1187	2234
	<i>0.90</i>	1077	124	129	1072	-70	1172	2114
	<i>0.85</i>	1017	117	122	1012	-66	1165	2055
	<i>0.80</i>	957	111	115	953	-62	1158	1995
	<i>0.75</i>	897	104	108	893	-58	1151	1936
	<i>0.70</i>	837	97	101	833	-54	1144	1876
Percent Change, %		90	90	90	90	90	99	95
		85	85	85	85	85	98	92
		80	80	80	80	80	98	89
		75	75	75	75	75	97	87
		70	70	70	70	70	96	84

Table 3.2 Example of stress magnitude changes for a location of strong shear and negative τ_{xx} , using different scaling factors. (The data were taken from a grid point in the eastern part of the model domain for Experiment 2; Figure 4.9).

	<i>factor</i>	τ_1	τ_2	τ_{xx}	τ_{yy}	τ_{xy}	σ_{xx}	σ_{yy}
Stress Magnitude, KPa	1.00	1187	-441	-179	925	-599	747	1851
	0.90	1068	-397	-161	832	-539	765	1758
	0.85	1009	-375	-152	786	-509	774	1712
	0.80	950	-353	-143	740	-479	783	1666
	0.75	890	-331	-134	694	-449	792	1620
	0.70	831	-309	-125	647	-419	801	1573
Percent Change, %		90	90	90	90	90	102	95
		85	85	85	85	85	104	93
		80	80	80	80	80	105	90
		75	75	75	75	75	106	88
		70	70	70	70	70	107	85

Remote Stresses

Remote stresses for a given boundary were approximated by averaging stresses interpolated to the boundary from the computed stress field. Comparison with the mean boundary stresses distal to the problem domain showed agreement with the approximation obtained using the immediate boundary, indicating that the mean, or occasionally the median, of the immediate boundary was an adequate representation of large-scale remote stresses. The remote stresses M_{xx} , M_{xy} , and M_{yy} are assumed to be constant at all locations within the model domain.

Calibration of Elasticity Constants

The elasticity constants for ice were calibrated so that modeled stresses resemble ice shelf stresses. Values from the literature (Hutter, 1983; Mellor, 1975; Rist et al., 1999; Rist et al., 2002) for the modulus of elasticity E range from 8000 to 10,000 kPa (rubber is ~ 100 kPa) and for Poisson's ratio range from 0.3 to 0.33 (a perfectly incompressible material is 0.5). These values form the initial estimates from which calibrations were made. Changing one parameter at a time and holding all other conditions constant, the stress field was simulated in the absence of a fracture. The root-mean-square error (RMSE) of mean stresses was used to determine the best fit of parameters. This method was consistent with a visual comparison between observed and simulated mean stresses. In the present work, typical calibrated values are 0.27 and 0.28 for Poisson's ratio and 7500 and 8000 kPa for the modulus of elasticity.

Fracture Toughness

Fracture toughness K_{mC} is a material property representing the critical stress intensity factor beyond which a fracture of mode m propagates. Values from the literature suggest that K_{IC} for ice-shelf ice ranges from 0.1 – 0.3 MPa m^{1/2} (Rist et al., 2002).

Stress Conditions within Model Domain

Stress conditions were calculated at specified points within the model domain. The Frac2D program was not able to handle large, skewed grids due to memory requirements. Thus, a simple box geometry was adopted for the observation grid. Grid spacing was 0.5 km x 0.5 km.

3.5 Model Outputs

Model outputs include stress intensity factors K_I and K_{II} for each active fracture tip, propagation angle θ_0 , failure criteria leading to mixed-mode propagation, and stress conditions for the boundary, fracture(s), and specified observation grid points.

Fracture Propagation

Fractures grow according to principal stress directions in the region of the fracture and the stress intensity at the propagating tip. Following each iteration, propagation criteria for each active tip are evaluated. Propagation of a single-mode fracture is predicted by comparing the tip stress intensity factor K_m and the fracture toughness, K_{mC} . A mode I fracture will propagate whenever $K_I > K_{IC}$, as long as the process zone is small compared to the length of the fracture (Figure 2.6). When these conditions are no longer satisfied, propagation will cease. For mixed-mode propagation, fracture

growth depends on K_I , K_{II} , and K_{IC} . The stress intensity factors were computed using Equation [2.19]. The propagation criterion (Equation [2.21]) and the angle of propagation (Equation [2.27]) were computed using the maximum circumferential tensile stress theory.

Modeled fracture propagation occurs by incremental growth at the fracture tips following each iteration of computations. If the stress field is unchanged, each fracture increment begins at the previous element tip and grows in the same orientation. If the stress field changes, the orientation of the fracture increment adjusts to minimize shear loading. A method described by Ingraffea (1987, p. 99-100) for approximating the fracture increment length is employed. The fracture is allowed to propagate some amount Δa in the direction θ_0 , where Δa is $2a$. If multiple iterations are performed, the fracture may grow incrementally. At each iteration step, the stress-intensity factors are recomputed. Time rate of propagation is not computed.

Viewing Changes in Simulated Stress Conditions

Two MATLAB tools were developed to read, plot, and archive model results. One tool reads the text-based model results for each iteration, computes mean, deviatoric, and principal stresses from the modeled full stresses, separates original and incremental fracture elements, archives the model results by iteration number in auto-generated MATLAB data files, and plots mean or principal stresses (**read_output.m**, Appendix C). The other tool plots a number of variables (mean stresses, components of the stress

tensor, principal stresses, maximum shear stress, theta) for a specified iteration step using a shade-colored plot, contour plot with manual labeling, or principal directions plot (**plot_data.m**, Appendix C).

4 Experiments

The importance of structural boundaries in crack tip arrest is investigated by modeling the propagation behavior of fractures at distinct steps in their downstream evolution, identified by provinces of similar fracture geometry in the ice shelf (Figure 3.8). In the outflow of the Evans Ice Stream, fracture geometry is defined by (1) an upstream-pointing segment that initiates in the shear zone of an ice stream or an ice stream tributary, and (2) a transverse segment that develops as the fracture advects through a stress field favorable to propagation normal to ice flow (Figure 4.1).

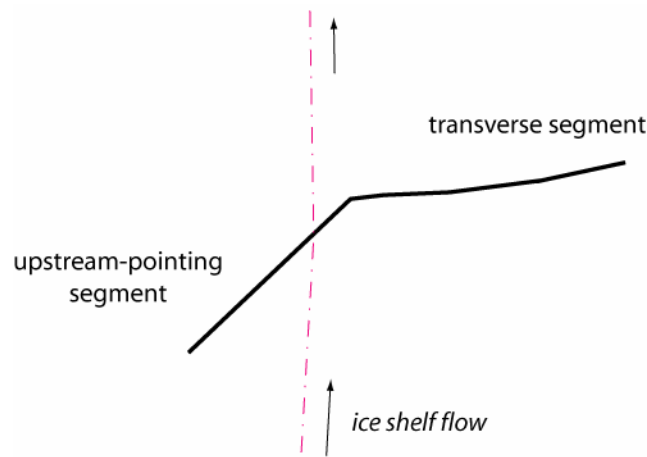


Figure 4.1 Fracture geometry is defined by an upstream-pointing segment, formed along a shear margin, and a transverse segment, formed as the fracture advects through a different stress field.

Propagation behavior is simulated to better understand controls on crack tip arrest and test the hypothesis that structural boundaries are important in the Ronne Ice Shelf. Experimentally-derived values for K_{IC} in Antarctic shelf ice range from 0.1 to 0.3 MPa $m^{1/2}$, with some scatter at shallow depths resulting in anomalously high values (Rist et

al., 2002). Rist et al. (1999) observed an approximately linear relationship between ice density and fracture toughness:

$$K_{IC} = 0.257\rho_i - 80.7 \quad (\text{kPa m}^{1/2}) \quad [4.1]$$

so that full density $K_{IC} = 0.155 \text{ MPa m}^{1/2}$ for the ice specimens of the study. For the present work, values for K_{IC} were 0.1, 0.15, and 0.3 $\text{MPa m}^{1/2}$. Following each iteration, the boundary stresses are re-computed. If the stresses encountered at the fracture tip are favorable to mixed-mode propagation, incremental growth occurs, which modifies the fracture geometry for the subsequent iteration. The iterative calculation is used only to simulate fracture geometry; there is no time component in the model. The longer a fracture becomes, the more likely it is to continue propagating in a given stress field. Several mechanisms may limit fracture growth: interaction among adjacent fractures, fracture length, inhomogeneities in the ice, and near-field stresses. In the present work, propagation is described as *unstable* if the fracture does not arrest until reaching the edge of the model domain. It is described as *episodic* if the fracture arrests and re-initiates when the stress field changes or fracture length increases during a simulation.

Five experiments, differentiated by location, test objectives, and fracture geometry, are described here (Figure 4.2). Test fractures, which are based on observed fracture geometry, are located in transitional zones between provinces of similar fracture geometry. Test fractures and, if appropriate, the observed fractures on which they are based, are mapped with principal deviatoric stresses (Figure 4.3).

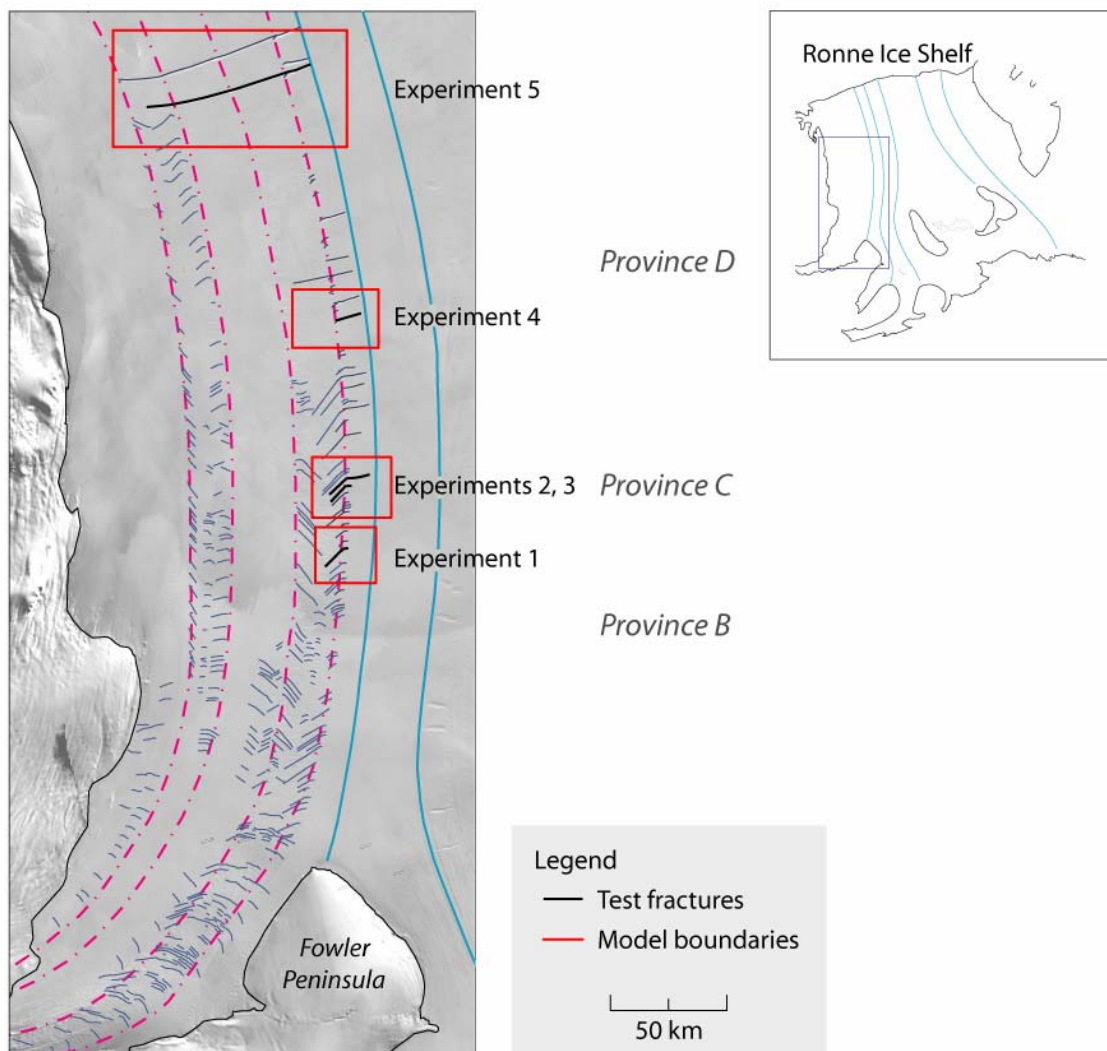


Figure 4.2 Overview map of experiment locations in the Evans Ice Stream outflow of the Ronne Ice Shelf.

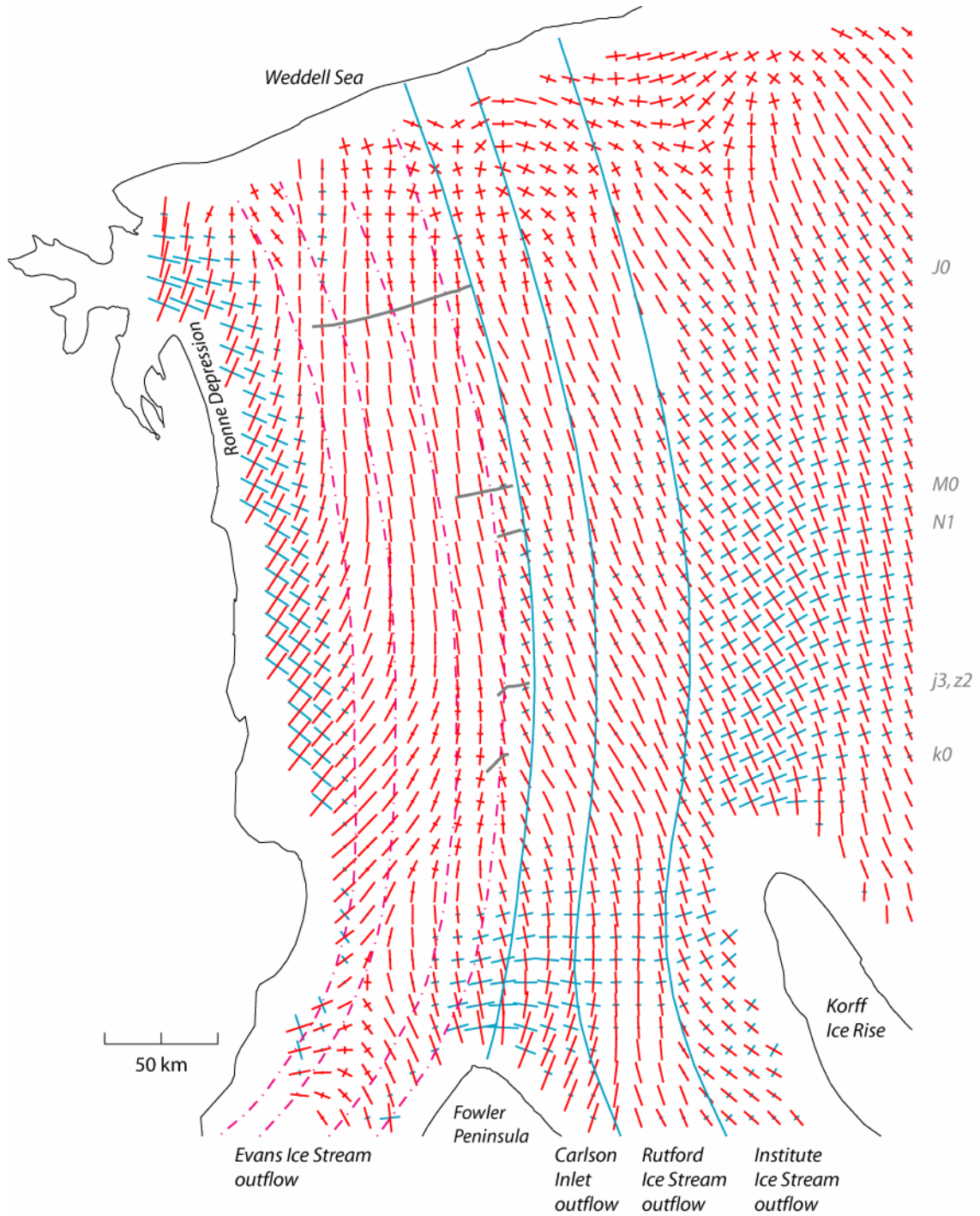


Figure 4.3 Principal stress orientations and relative magnitudes (red: extensive, cyan: compressive). Fracture labels at right correspond to dark lines in map representing test fractures.

4.1 Experiment 1

In *province B*, closely-spaced (1-2 km) fractures develop along the 4/5 suture zone in the wake of Fowler Peninsula (Figure 4.2). As these fractures advect downstream to the location of Experiment 1, some rotation occurs, the upstream-pointing segments become less visible in the satellite imagery, and the outboard geometry changes, with ~1 km growth observed normal to ice flow. Downstream of this location, propagation of the transverse tip is observed. The objectives of this experiment are: (1) to determine if the upstream-pointing fracture tip is active at this location, and (2) to find the stress conditions required to make the transverse tip grow. If the predicted growth orientation of the upstream-pointing fracture segment differs from the observed fracture geometry, it is reasonable to assume that the tip is inactive and that tip arrest must have occurred somewhere upstream.

Experiment 1 is located at the downstream end of *province B* in the ice shelf (Figure 4.4a). *Test fracture k1* is identical to an observed fracture but is shortened by ~8 km on its upstream-pointing, western side (Figure 4.4b). Both fracture tips are allowed to propagate. The principal stress map shows that *test fracture k1* is located ~10 km upstream of a zone of compression and increasing shear stress (Figure 4.5). In general, extensive stresses are observed to the west of the model boundary. The model area is 624 km².

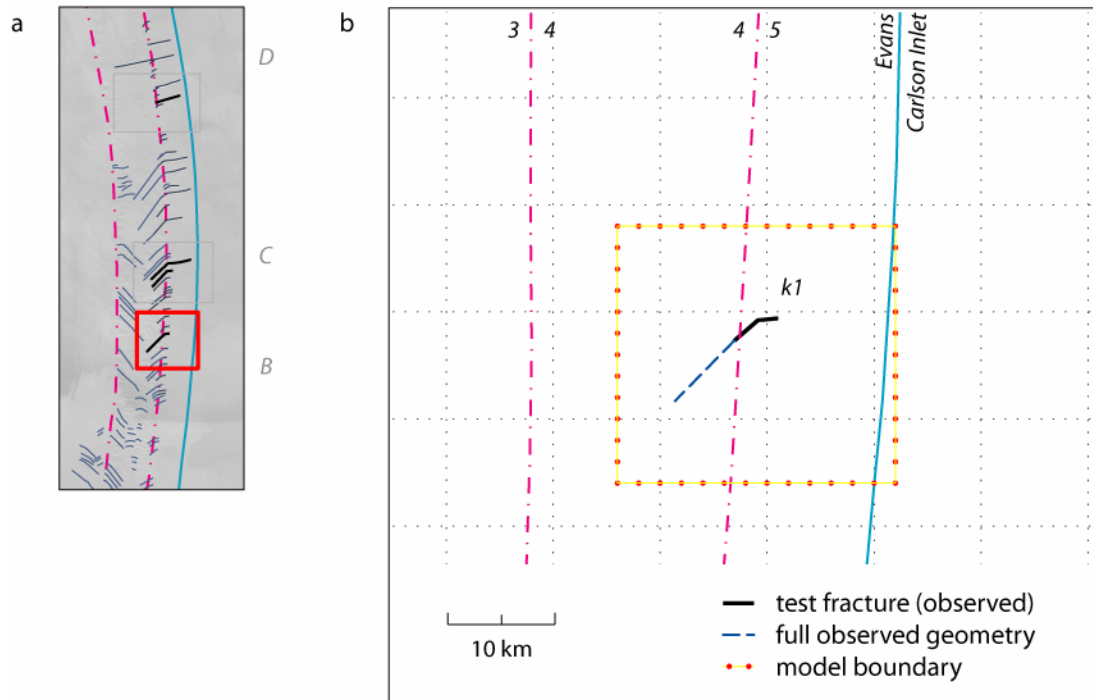


Figure 4.4 (a) Location of Experiment 1 in the ice shelf highlighted by solid box. (b) Model boundary showing *test fracture k1*. The dots along the model boundary mark endpoints of the boundary elements. Suture zones formed between ice from different tributaries are marked by dash-dotted lines and the suture zone between outflows of the Evans and Carlson Inlet Ice Streams is marked by a solid cyan line.

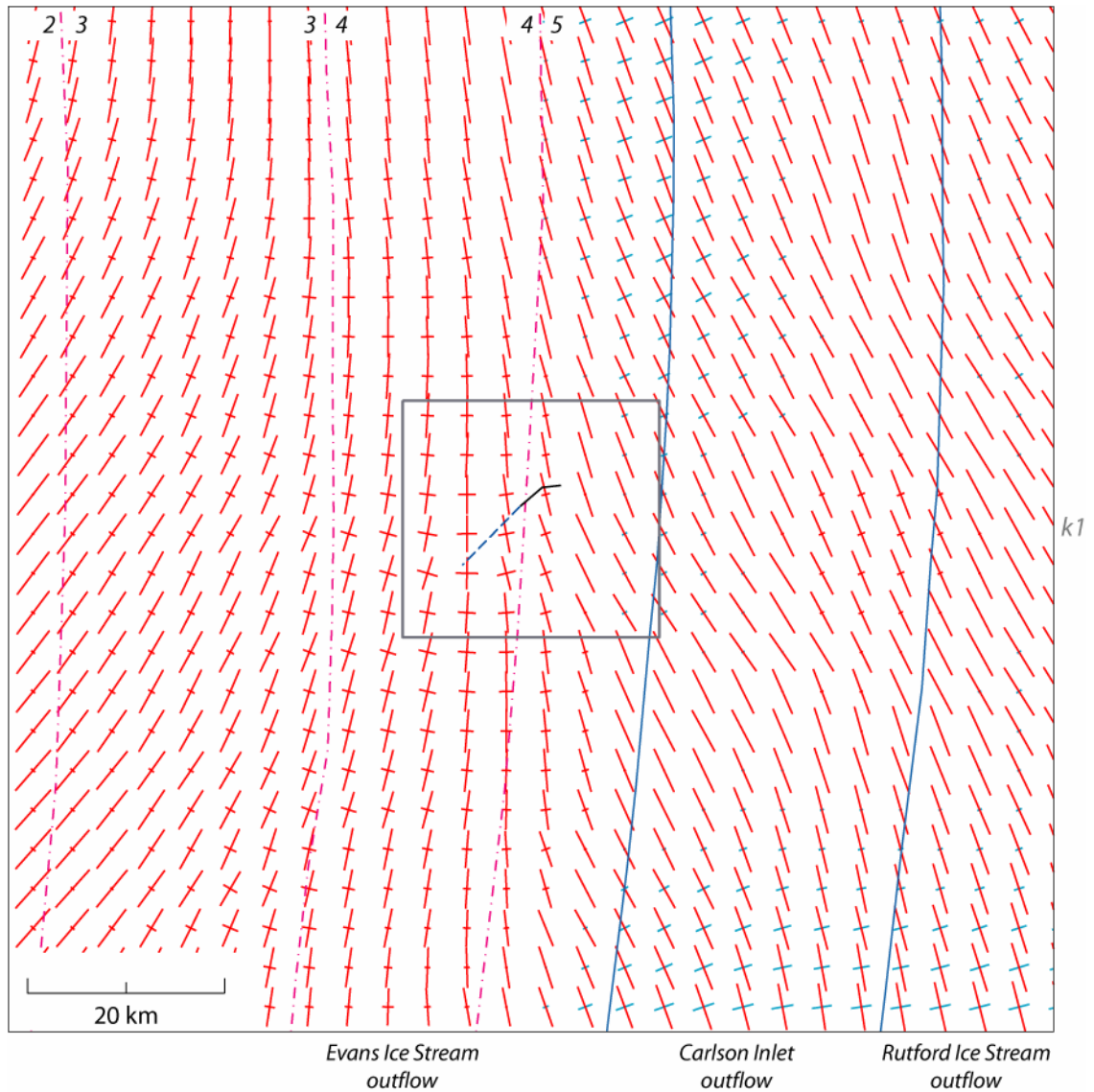


Figure 4.5 Experiment 1: Principal stress orientations and relative magnitudes (red: extensive, cyan: compressive). The trace of *test fracture k1*, model boundary, and suture zones are for reference only. The 2/3, 3/4, and 4/5 suture zones and ice stream outflows are labeled.

Experiment Calibration

The elasticity constants were calibrated for this location in the ice shelf by simulating stress conditions in the model domain in the absence of a fracture. The calibration for this location required satisfying two criteria: (1) to represent the overall

east to west increasing stress gradient, and (2) to replicate the observed mean stress magnitudes (Figure 4.6a). These are hereafter referred to as the *general calibration criteria*. The spatial stress gradients were most influenced by changes to the elasticity constants. The modulus of elasticity E varies with softening due to the strain history, depth, and other factors. Other studies with values similar to this study include Rist et al., (2002; $E = 9000$ - 1000 MPa near the central front of the Ronne), Hutter (1983; $E = 9200$ - 9400 MPa, $\nu=0.314$ in lab studies), and Stephenson (1984; $E = 9000$ GPa in field studies). Different values of E can be found in Vaughn (1995). Throughout the literature, $\nu=0.3$. Stress magnitudes were scaled by a factor \mathfrak{S} (Chapter 3, Model Inputs). For this experiment, the remote stresses were $M_{xx} = 1200$ kPa, $M_{yy} = 1900$ kPa, and $M_{xy} = -100$ kPa. The best representation of observed mean stress magnitudes was found by setting $\mathfrak{S} = 0.8$ (or 80% of principal deviatoric stresses computed from the observed velocity) for the model domain boundary stresses. The best approximation of observed mean stresses was obtained using $\nu=0.27$ and $E=7500$ MPa (RMSE = 78, Figure 4.6b, Table A.1). Two other calibration examples are shown for comparison (Figure 4.6c-d).

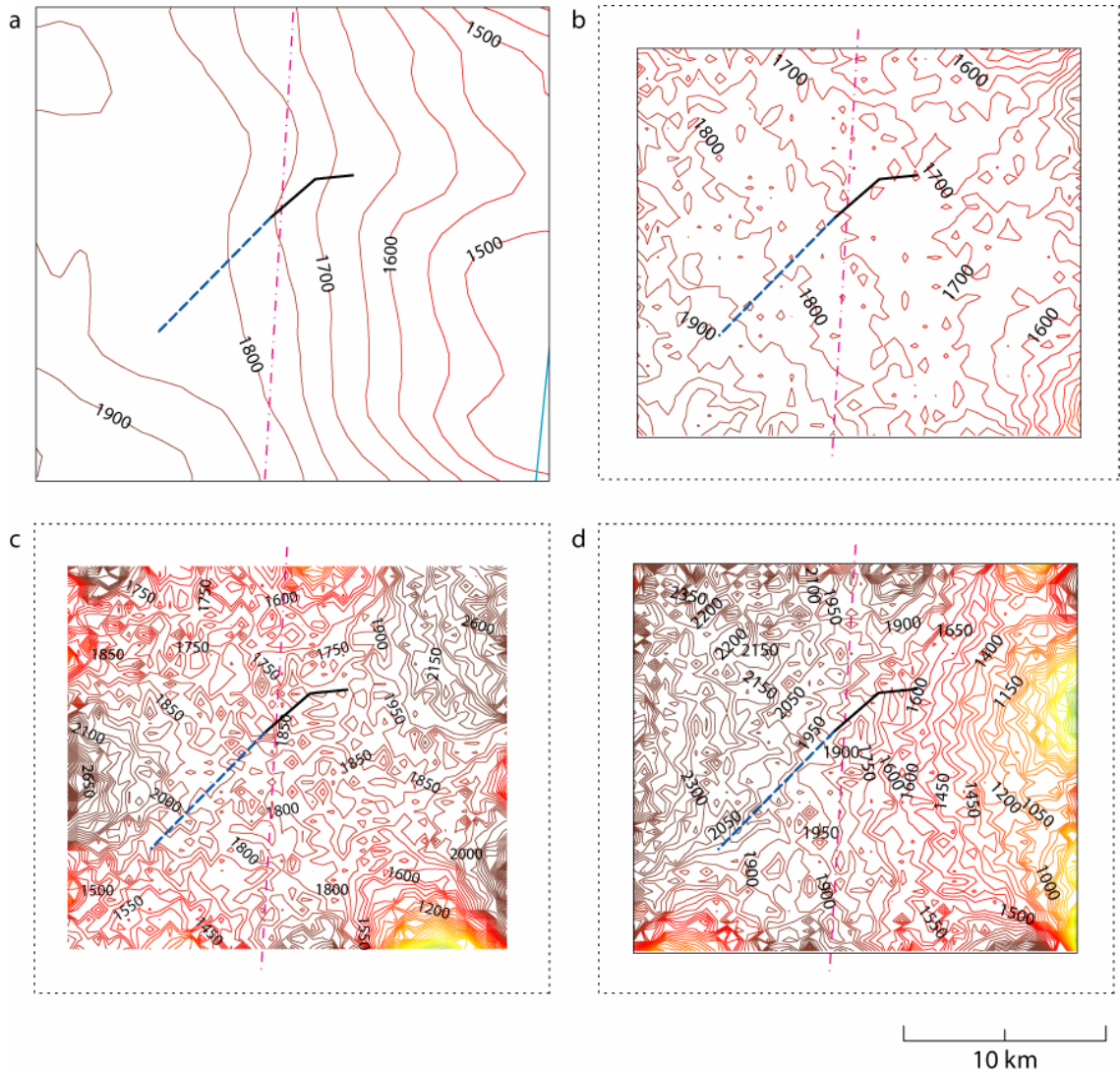


Figure 4.6 (a) Observed mean stresses. Contour interval is 50 kPa. (b-d) Mean stresses in the absence of a fracture simulated using remote stresses, $M_{xx} = 1200$ kPa, $M_{yy} = 1900$ kPa, and $M_{xy} = -100$ kPa, $\nu = 0.8$, and elasticity constants as noted (Table A.1). Contour interval is 50 kPa. The fracture trace drawn in each panel is for reference only. Stresses near the boundary are not easily available in the model output and are not contoured, resulting in white space around the perimeter of the model domain. (b) Best-fit calibration, $\nu = 0.27$, $E = 7500$ MPa, and RMSE = 78. (c) $\nu = 0.28$, $E = 7000$ MPa, and RMSE = 315. (d) $\nu = 0.28$, $E = 8000$ MPa, and RMSE = 334.

Fracture Propagation Results

Fracture propagation was investigated by incorporating *test fracture k1* as a boundary condition and using the calibrated boundary stresses and elasticity constants. Stress conditions along *test fracture k1* were scaled by a factor \mathfrak{S} to initiate fracture propagation. The fracture did not propagate under the best-fit model stress field using $K_{IC} = 0.1 \text{ MPa m}^{1/2}$ (Table B.1). The Mode I stress intensity factors at both tips were negative and $K_{II} = 0 \text{ MPa m}^{1/2}$. Reducing principal stresses along the fracture by 6.25% ($\mathfrak{S} = 0.75$ instead of 0.8) caused the fracture to propagate at both tips (Figure 4.7, Table B.2). At the right tip, $K_I = 0.36 \text{ MPa m}^{1/2}$ and $K_{II} = 0 \text{ MPa m}^{1/2}$, exceeding the fracture toughness $0.3 \text{ MPa m}^{1/2}$. At the left tip, $K_I = 0.47 \text{ MPa m}^{1/2}$ and $K_{II} = 0.41 \text{ MPa m}^{1/2}$. Propagation continued until intersection with the edge of the model domain. A relatively small change in stress conditions was required to drive the eastward propagation that is observed downstream. Because K_{II} was non-zero at the western tip, the stress field was not aligned with the orientation of the fracture tip and we conclude that the observed fracture geometry did not develop in this location but must have formed somewhere upstream.

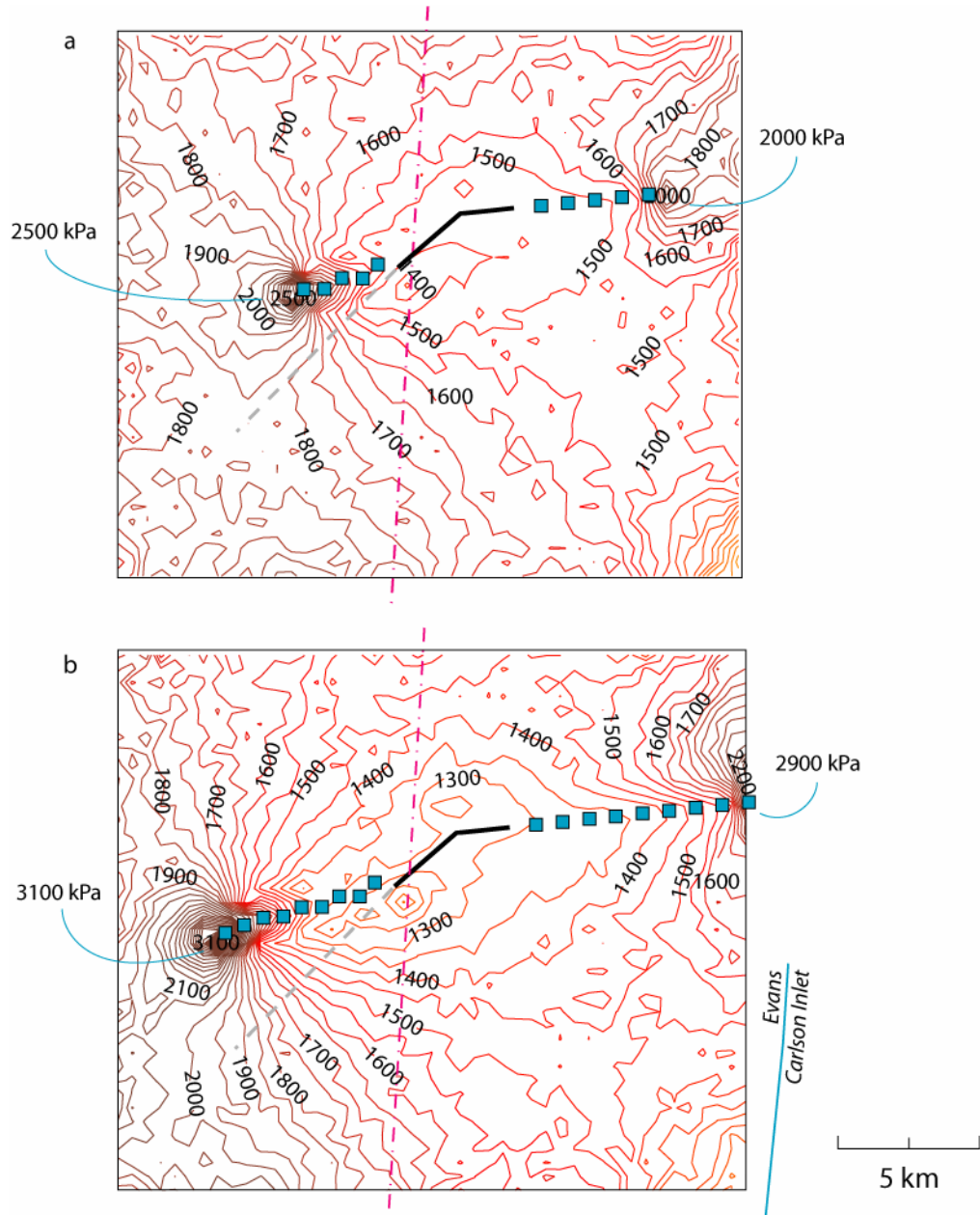


Figure 4.7 Experiment 1: Simulated propagation of test fracture *k1* and mean stresses within model domain. For these panels, $K_{IC} = 0.3 \text{ MPa m}^{1/2}$ and $\mathfrak{I} = 0.75$ for the fracture boundary stresses (Table B.2). Contour interval is 50 kPa. Mean stresses near the fracture trace were interpolated. (a) **Iteration 6**. At the eastern tip of *test fracture k1*, $K_I = 1.08 \text{ MPa m}^{1/2}$, $K_{II} = 0.0 \text{ MPa m}^{1/2}$, and the angle of propagation $\theta_0 = 0^\circ$. At the western tip, $K_I = 1.66 \text{ MPa m}^{1/2}$, $K_{II} = -0.41 \text{ MPa m}^{1/2}$, and $\theta_0 = 25.3^\circ$. (b) **Iteration 10**. The eastern tip intersected the model boundary ($K_I = 2.17 \text{ MPa m}^{1/2}$, $K_{II} = 0.0 \text{ MPa m}^{1/2}$, and $\theta_0 = 0^\circ$). At the western tip, $K_I = 3.10 \text{ MPa m}^{1/2}$, $K_{II} = 0.41 \text{ MPa m}^{1/2}$, and $\theta_0 = -14.7^\circ$.

4.2 Experiment 2

In *province C*, the transverse tips of observed fractures at the 4/5 suture zone propagate east before arresting at the structural boundary formed by the Evans and Carlson Inlet flows. Fractures are closely-spaced (distance between each is short relative to fracture length) and the upstream-pointing segment becomes less visible in the satellite imagery with distance downstream. Experiment 1 showed that the upstream-pointing tip is likely passive near this location, but does the geometry still matter? The objectives of this experiment are (1) to study interaction among adjacent fractures, (2) to determine if a non-propagating, upstream-pointing segment plays a role in the observed growth of the transverse tip, and (3) to determine if the structural boundary formed by the Evans-Carlson suture zone is important in crack tip arrest.

Experiment 2 is the first of two experiments located at the upstream end of *province C* (Figure 4.8a). To study the interaction among closely-spaced, subparallel fractures, two suture zone fractures of unequal lengths located ~25 km downstream of *test fracture k1* were investigated. The geometry of *test fracture g6*, which is identical to an observed fracture, is similar to that of *test fracture k1*. *Test fracture j3*, 3.4 km downstream of *test fracture g6*, is important because the fracture on which it is based propagated nearly 8 km beyond the easternmost tip of any upstream fracture. *Test fracture j3* is identical to the observed fracture but is shortened by ~5 km at its eastern tip. Two model boundaries are described here. The smaller model area is 832 km². The eastern boundary was extended 2 km to allow propagation through the eastern suture

zone and to minimize boundary effects on the stress field in this region. The extended-boundary area is 884 km².

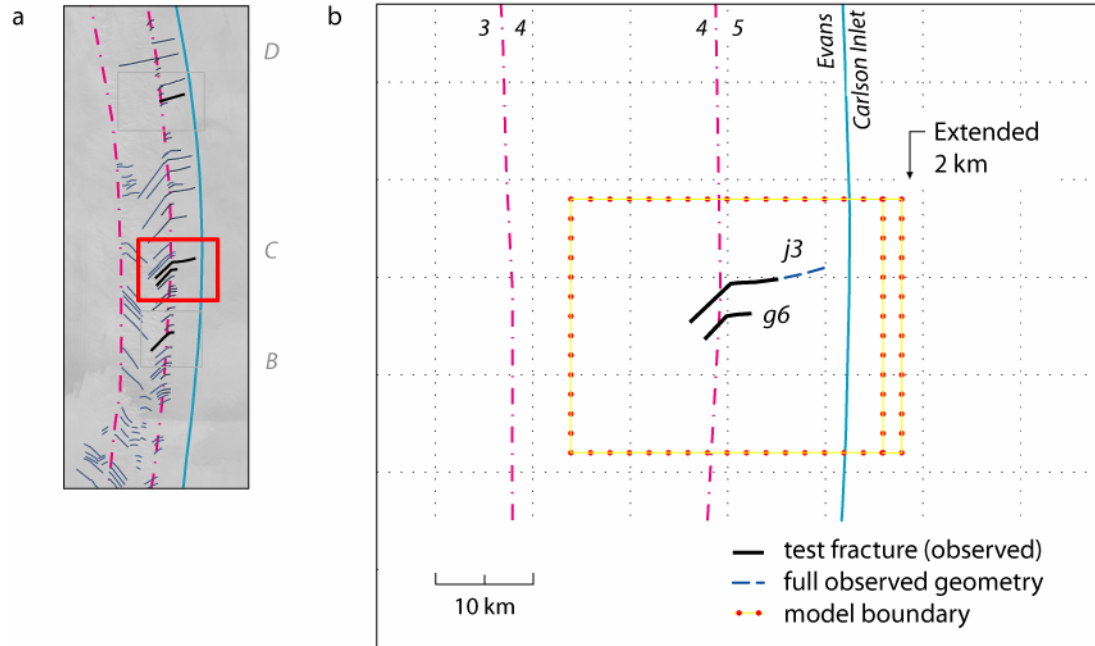


Figure 4.8 (a) Location of Experiment 2 in the ice shelf highlighted by dark box. (b) Model boundaries show fractures *g6* and *j3*. The two model boundaries are represented by dotted lines, where the dots represent element endpoints.

The principal compressive stresses at the eastern side of the model domain (Figure 4.9) suggest *a priori* that conditions may be favorable for growth of the transverse tip. The “glaciological” stress field and parameters with which the model is initialized do not accommodate small-scale variations that may arise due to the suture zone between the Evans and Carlson Inlet flows. Comparison between model and observed fracture geometry in the suture zone region can be interpreted in terms of the importance of the structural boundary to propagation. Downstream of this location, other fractures with geometry similar to that of *test fractures g6* and *j3* are observed to have propagated and

arrested at the suture zone. As larger fractures dominate, fracture spacing increases and smaller features such as *test fracture g6* become less visible in the satellite imagery.

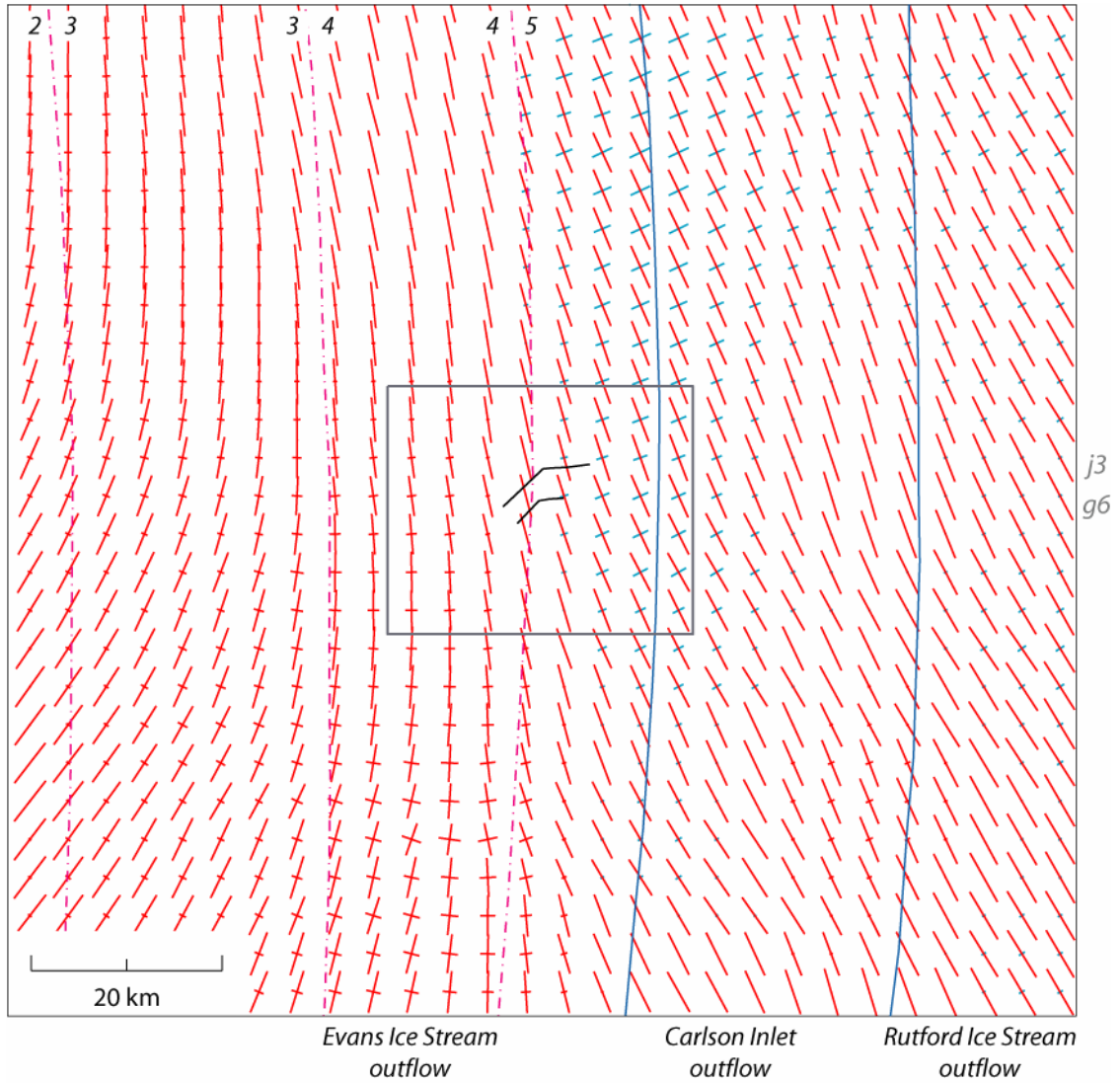


Figure 4.9 Experiment 2: Principal stress orientations and relative magnitudes (red: extensive, cyan: compressive). *Test fractures g6* and *j3* (labeled at right of map) are shown within smaller model boundary. Refer to Figure 4.5 for a description of labels.

Model Calibration

In addition to satisfying the general calibration criteria, model calibration required simulating higher stresses observed upstream and distal to the shear margin. The remote stresses were $M_{xx} = 900$ kPa, $M_{yy} = 1800$ kPa, and $M_{xy} = -300$ kPa (different from Experiment 1) and $\mathfrak{S} = 0.8$ for the model boundary. For the smaller boundary, the best approximation of observed mean stresses that satisfied the calibration criteria was obtained using $\nu = 0.29$ and $E = 8000$ MPa (RMSE = 85, Figure 4.10b, Table A.2). Two other examples demonstrate how small adjustments in elasticity constants may lead to unacceptable initial stress fields (Figure 4.10c-d).

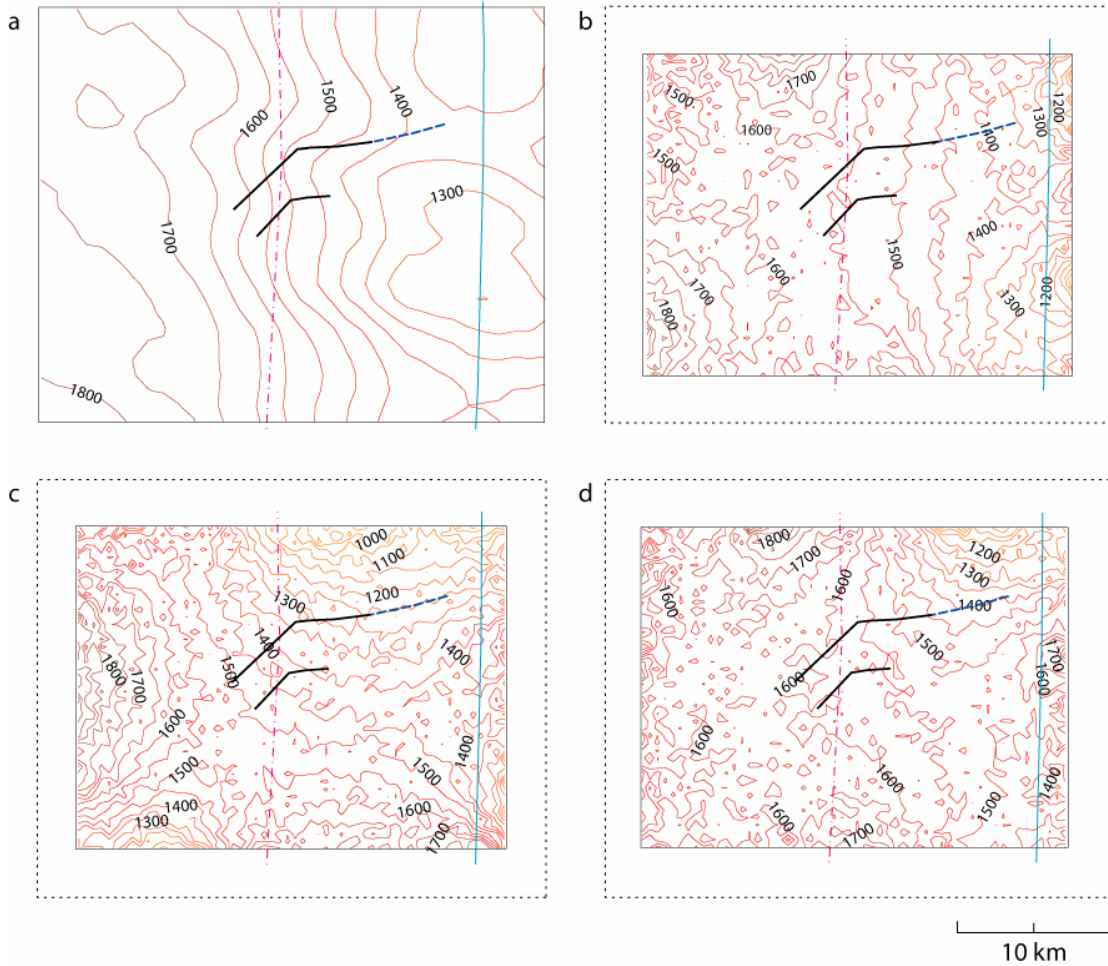


Figure 4.10 (a) Observed mean stresses. Contour interval is 50 kPa. (b-d) Mean stresses in the absence of a fracture simulated using remote stresses, $M_{xx} = 900$ kPa, $M_{yy} = 1800$ kPa, and $M_{xy} = -300$ kPa, $\mathfrak{I} = 0.8$, and elasticity constants as noted (Table A.2). Contour interval is 50 kPa. The fracture trace and suture zones drawn in each panel are for reference only. Refer to Figure 4.6 for an explanation about the dashed box. (b) Best-fit calibration, $\nu = 0.29$, $E = 8000$ MPa, and RMSE = 85. (c) Stress gradient increased from top to bottom, not east to west, $\nu = 0.28$, $E = 8000$ MPa, and RMSE = 185. (d) Stresses are concentrated along model boundary, $\nu = 0.29$, $E = 8500$ MPa, and RMSE = 128.

Calibration of the extended-boundary domain was less successful. Moving the boundary more than a few kilometers to the outboard side of the (eastern) suture zone introduced spatial gradients and stress concentrations that were inconsistent with observed mean stresses (Figure 4.11, Table A.3). The extended-boundary domain was not used in propagation simulations.

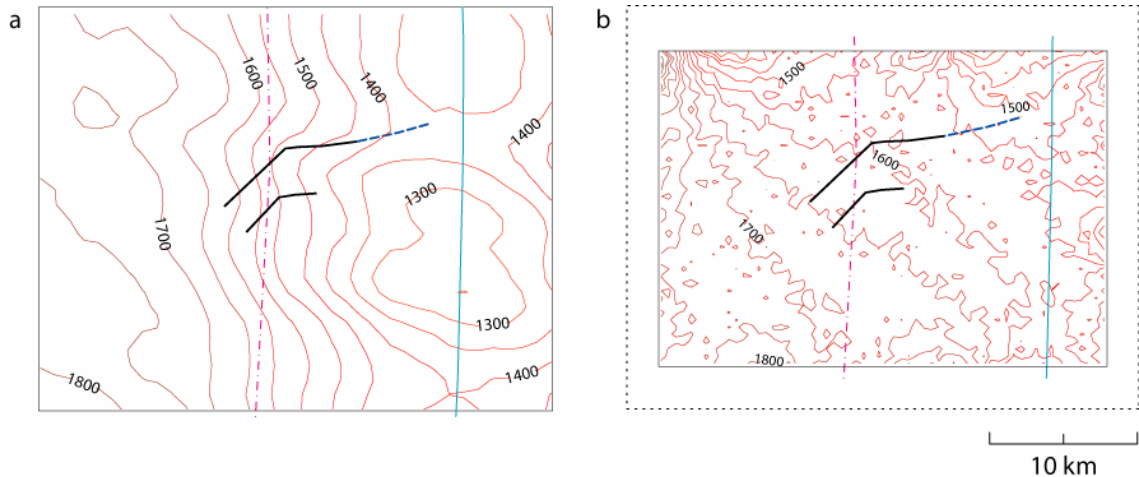


Figure 4.11 (a) Observed mean stresses for extended-boundary domain. Contour interval is 50 kPa. (b) Mean stresses in the absence of a fracture simulated using remote stresses, $M_{xx} = 900$ kPa, $M_{yy} = 1800$ kPa, $M_{xy} = -300$ kPa, and $\mathfrak{S} = 0.8$ (Table A.3). Elasticity constants were $\nu = 0.27$ and $E = 8000$ (RMSE = 170). Contour interval is 50 kPa. The fracture trace drawn in each panel is for reference only. Refer to Figure 4.6 for an explanation about the dashed box.

Fracture Propagation Results

Fracture propagation was investigated by incorporating *test fractures g6* and *j3* as boundary conditions for the smaller boundary. The upstream-pointing segments of the fractures are included as model boundaries but their tips are set to be inactive. This allows the complete fracture geometry to modify the near-field stresses while maintaining the non-propagating tips at their observed locations. Propagation was controlled by modifying the scaling factor \mathfrak{S} for the boundary stresses along the fracture. When $\mathfrak{S} = 0.8$ and $K_{IC} = 0.1 \text{ MPa m}^{1/2}$, the active fracture tips did not propagate (Table B.3). When principal stresses along the fracture were reduced by 6.25% ($\mathfrak{S} = 0.75$ instead of 0.8), *test fracture j3* propagated once to relieve shear stress before crack tip arrest ($K_{IC} = 0.3 \text{ MPa m}^{1/2}$, Figure 4.12, Table B.4).

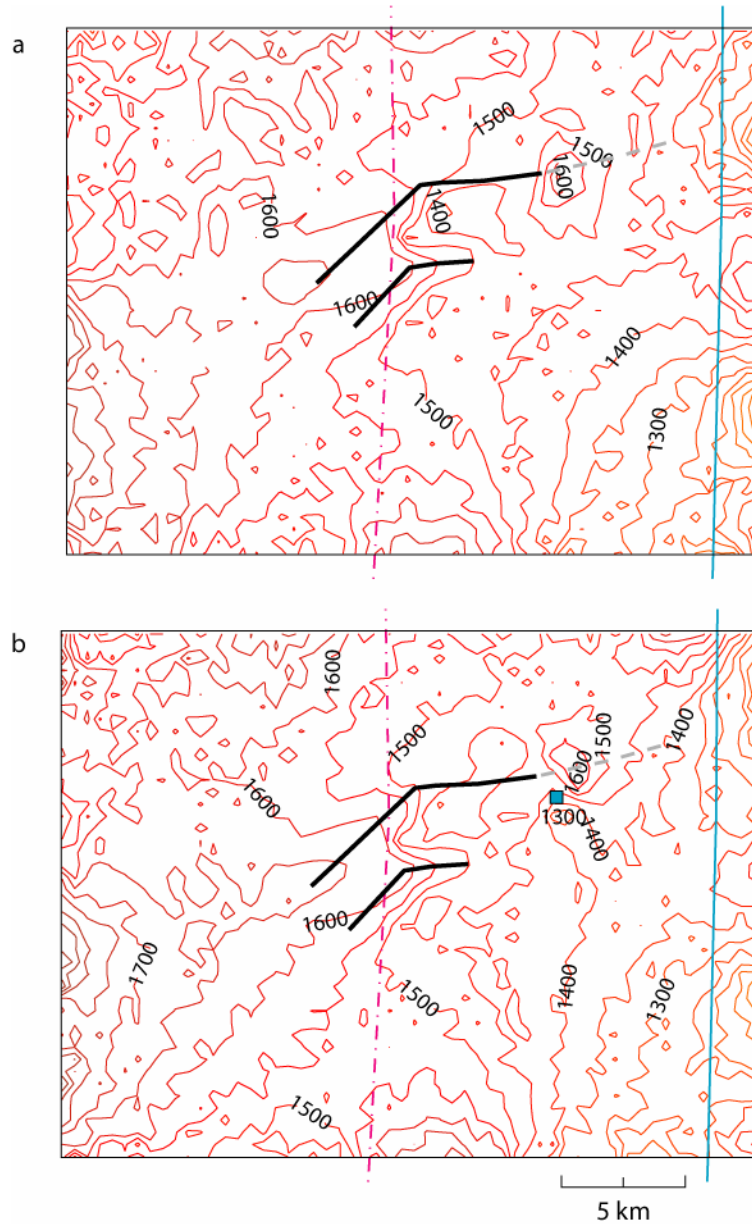


Figure 4.12 Experiment 2: Simulated propagation of *test fractures* $j3$ and $g6$ and mean stresses within model domain. For these panels, the fracture toughness $K_{IC} = 0.3 \text{ MPa m}^{1/2}$ and $\mathfrak{S} = 0.75$ for the fracture boundary stresses (Table B.4). Contour interval is 50 kPa. Mean stresses near the fracture trace were interpolated. (a) **Iteration 1.** (b) **Iteration 2.**

Setting $\mathfrak{S} = 0.7$, or reducing principal stresses along the fracture by 13%, caused unstable propagation of *test fracture* $j3$ and no growth of *test fracture* $g6$ ($K_{IC} = 0.3 \text{ MPa m}^{1/2}$, Table B.5). The computed stress intensity factors at the eastern tip of *test*

fracture j3 remained unchanged as the fracture propagated 5.5 km toward the Evans-Carlson suture zone, with the same orientation as the observed fracture geometry ($K_I = 0.70 \text{ MPa m}^{1/2}$ and $K_{II} = 0 \text{ MPa m}^{1/2}$, Figure 4.13a). At 1.5 km from the suture zone, a new propagation pattern developed that continued as the fracture crossed the suture zone (Figure 4.13b).

The role of the upstream-pointing segment of the fracture, or at a minimum, a non-propagating western tip, may be important in facilitating the observed growth of the transverse tip. Stress intensity factors are not computed for inactive fracture tips. Nevertheless, mean stresses suggest that stress intensity is higher at the western tip, increasing with fracture growth (1800 kPa compared to 1600 kPa in Iteration 5 as *test fracture j3* nears the eastern suture zone).

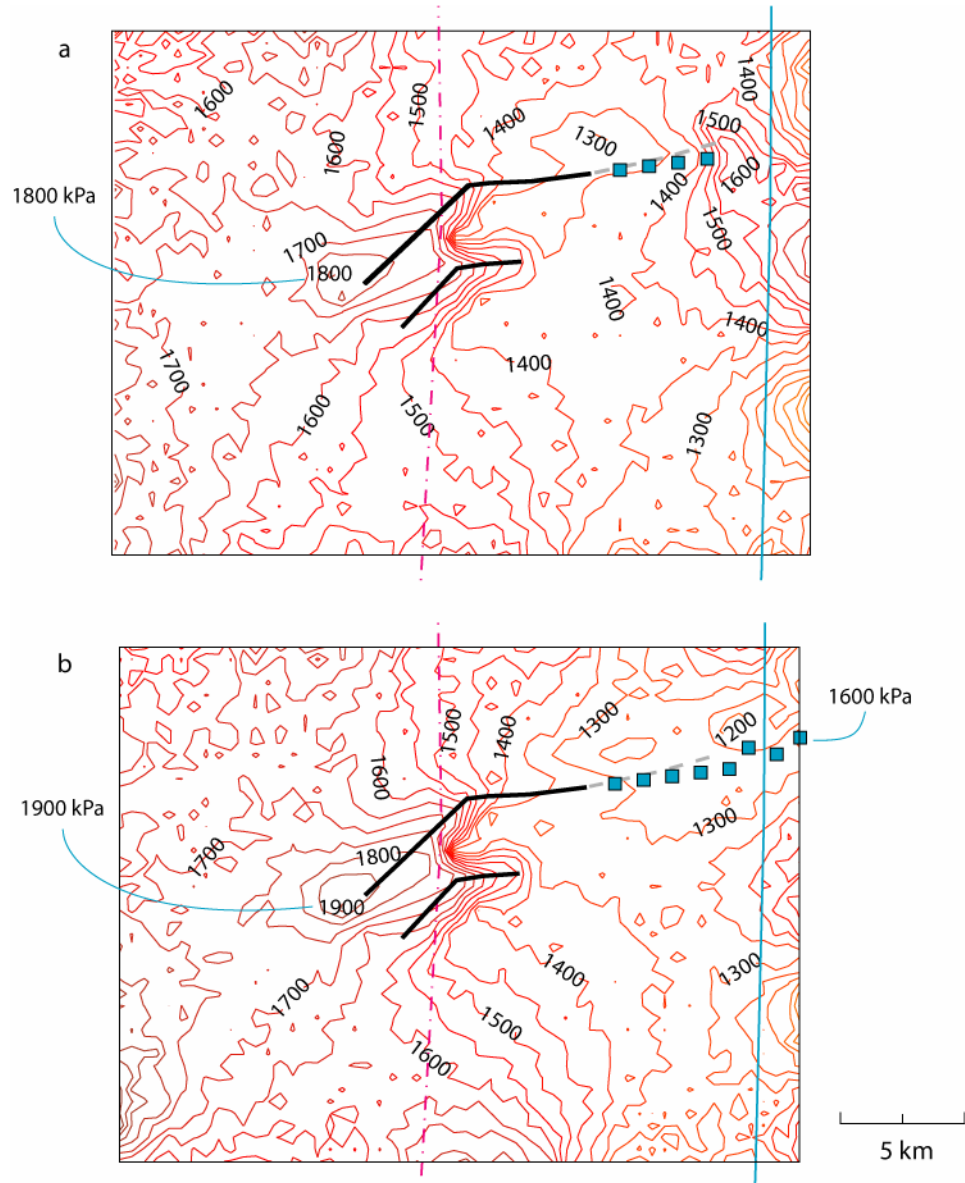


Figure 4.13 Experiment 2: Simulated propagation of *test fractures* $j3$ and $g6$ and mean stresses within model domain. For these panels, the fracture toughness $K_{IC} = 0.3 \text{ MPa m}^{1/2}$ and $\mathfrak{I} = 0.7$ for the fracture boundary stresses (Table B.5). Mean stresses near the fracture trace were interpolated. (a) **Iteration 5**. At the eastern tip of *test fracture* $j3$, $K_I = 0.70 \text{ MPa m}^{1/2}$, $K_{II} = 0.0 \text{ MPa m}^{1/2}$, and the angle of propagation $\theta_0 = 0^\circ$. At the eastern tip of *test fracture* $g6$, both K_I and $K_{II} = 0.0 \text{ MPa m}^{1/2}$. (b) **Iteration 9**. At the eastern tip of *test fracture* $j3$, $K_I = 0.44 \text{ MPa m}^{1/2}$, $K_{II} = 0.70 \text{ MPa m}^{1/2}$, and $\theta_0 = -59.2^\circ$. The stress intensity factors at the eastern tip of *test fracture* $g6$ were zero.

4.3 Experiment 3

Shear margin fracture geometries become less distinct in the remote-sensed imagery at the downstream end of *province C* (~30 km downstream of *test fracture j3*). The upstream-pointing segments of the fractures begin to disappear, presumably as the now-relict features fill with wind-blown snow. By ~80 km downstream of *test fracture j3*, the upstream-pointing segments are no longer visible in the MOA and the fracture tips appear to be located at the 4/5 boundary. At that location (Province *D* in Figure 4.2), a new episode of propagation begins, with a new propagation direction (to the west).

The objectives of this experiment are: (1) to assess the importance of the upstream-pointing segment, (2) to investigate crack tip arrest at the eastern suture zone, and (3) to determine the stress conditions required to induce propagation west beyond the 4/5 suture zone. The first objective is investigated by removing the upstream-pointing segment from the test fracture geometry. Experiment 2 showed that localized shear stresses in the eastern suture zone may reduce the mode I stress intensity factor at the eastern tip (Figure 4.12). The propagation behaviors of three fracture lengths are evaluated to determine if the presence of the upstream-pointing segment is required to permit eastward propagation. For the second objective, two outcomes are possible. If the eastern tip of a test fracture arrests before reaching the Evans-Carlson suture zone, then the stress field or adjacent fractures must control tip arrest. By contrast, if propagation is observed to cross the suture zone with little, if any, variation in preferred orientation, then inhomogeneities in the ice associated with the structural boundary must be responsible for the crack tip arrest observed at this location in the shelf.

Experiment 3 is the second of two experiments located at the upstream end of *province C* (Figure 4.14a). Because its geometry is characteristic of the fractures throughout *province C*, the fracture that forms the basis of the *test fracture j3* geometry is again investigated. Here, the geometry of *test fracture z2* is defined as the full transverse segment of the observed fracture, oriented approximately normal to ice flow. The western tip lies 1 km east of the 4/5 suture zone and the eastern tip is 2.3 km west of the Evans-Carlson suture zone (Figure 4.14b). By removing the upstream-pointing segment, the western tip of *test fracture z2* becomes aligned with principal compressive stresses (Figure 4.15). These stresses appear, *a priori*, to be favorable to growth at either fracture tip. The propagation behaviors of two other fracture lengths are also simulated. The western tips of both fracture lengths have an endpoint coincident with the western tip of *test fracture z2* near the 4/5 suture zone. From this tip, *test fracture s6* extends 2.6 km east and *test fracture s4* extends 5 km east, also coincident with the *test fracture z2* axis (Figure 4.14c).

Two model boundaries were used for the experiments presented here (Figure 4.14b). The downstream and eastern model boundaries are identical to those in Experiment 2. The upstream and western boundaries of the smaller domain were placed in closer proximity to the fractures (model area 336 km²). For the larger domain, the western boundary was extended 4 km, to better represent the behavior of *test fracture z2* near the 4/5 suture zone (model area 468 km²).

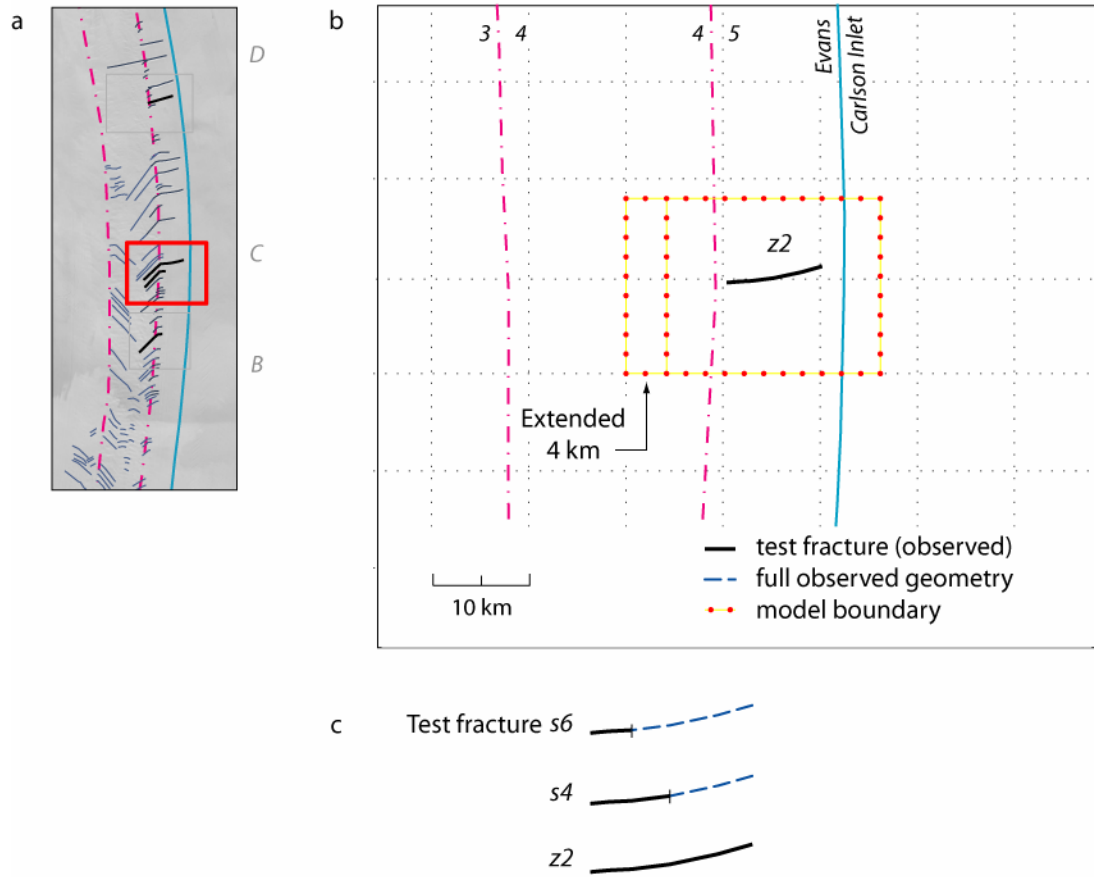


Figure 4.14 (a) Location of Experiment 3 in the ice shelf. (b) The model boundary is represented by dotted lines. (c) Three fracture lengths overlap and share a western endpoint.

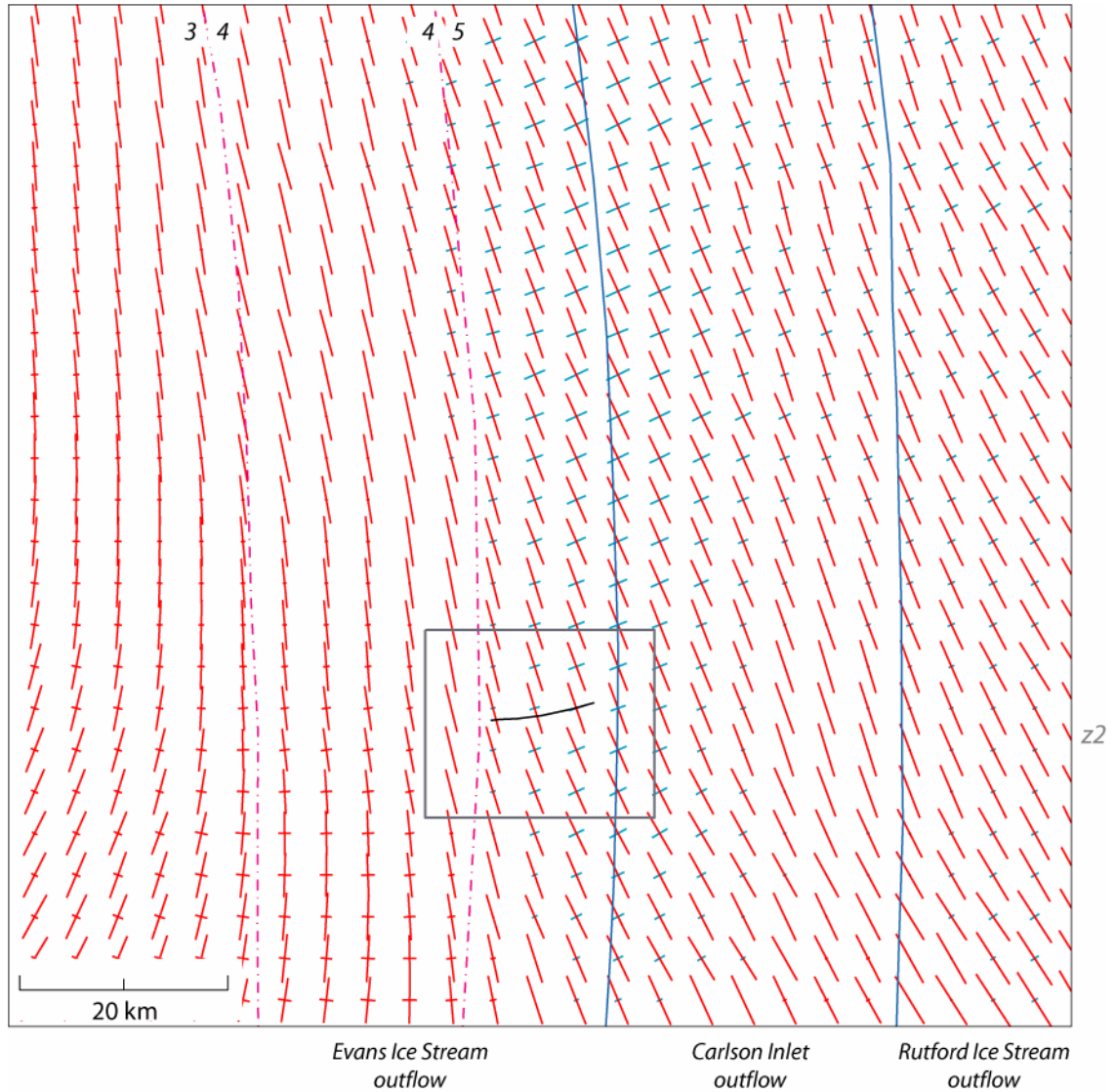


Figure 4.15 Experiment 3: Principal stress orientations and relative magnitudes (red: extensive, cyan: compressive). *Test fracture* z_2 is shown within smaller model boundary. The 3/4 and 4/5 suture zones are labeled.

Model Calibration

Calibration required satisfying the general calibration criteria outlined for Experiment 1. The remote stresses were $M_{xx} = 900$ kPa, $M_{yy} = 1800$ kPa, and $M_{xy} = -300$ kPa. For the smaller boundary, the best calibration satisfying the general calibration

criteria was obtained using $\mathfrak{I} = 0.8$, $\nu = 0.28$ and $E = 8000$ MPa (RMSE = 49, Figure 4.16b, Table A.4). Two other examples are shown for comparison (Figure 4.16c-d). The best calibration for the extended-boundary domain was obtained using $\mathfrak{I} = 0.9$ (different from the smaller boundary), $\nu = 0.27$, and $E = 8000$ MPa (RMSE = 47, Figure 4.17b, Table A.5).

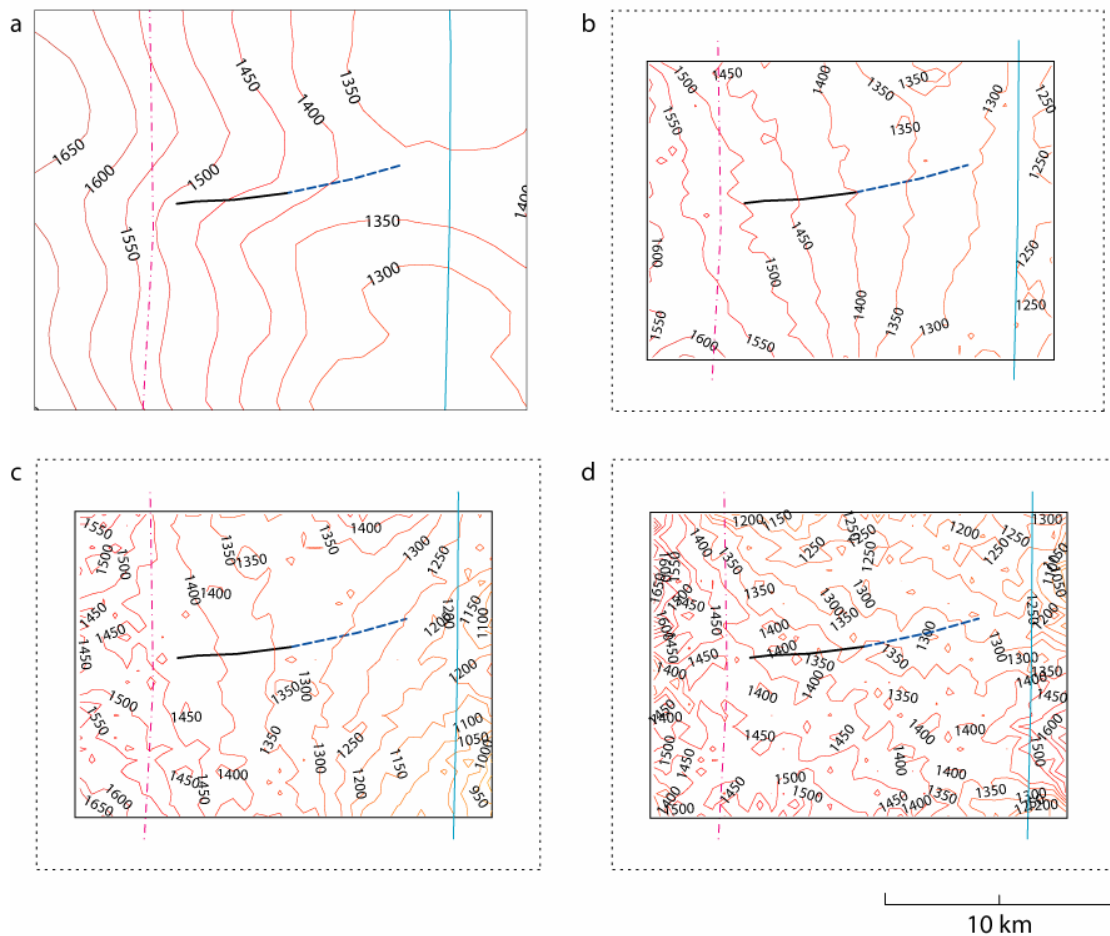


Figure 4.16 (a) Observed mean stresses for the smaller boundary. Contour interval is 50 kPa. (b-d) Mean stresses in the absence of a fracture simulated using remote stresses, $M_{xx} = 900$ kPa, $M_{yy} = 1800$ MPa, and $M_{xy} = -300$ kPa, $\mathfrak{I} = 0.8$, and elasticity constants as noted (Table A.4). Contour interval is 50 kPa. The fracture trace drawn in each panel is for reference only. Refer to Figure 4.6 for an explanation about the dashed box. (b) Best-fit calibration, $\nu = 0.28$, $E = 8000$ MPa, and RMSE = 49. (c) Stresses are concentrated at corners and along boundaries, $\nu = 0.3$, $E = 9000$ MPa, and RMSE = 107. (d) Stress gradient is incorrect, $\nu = 0.29$, $E = 8500$ MPa, and RMSE = 121.

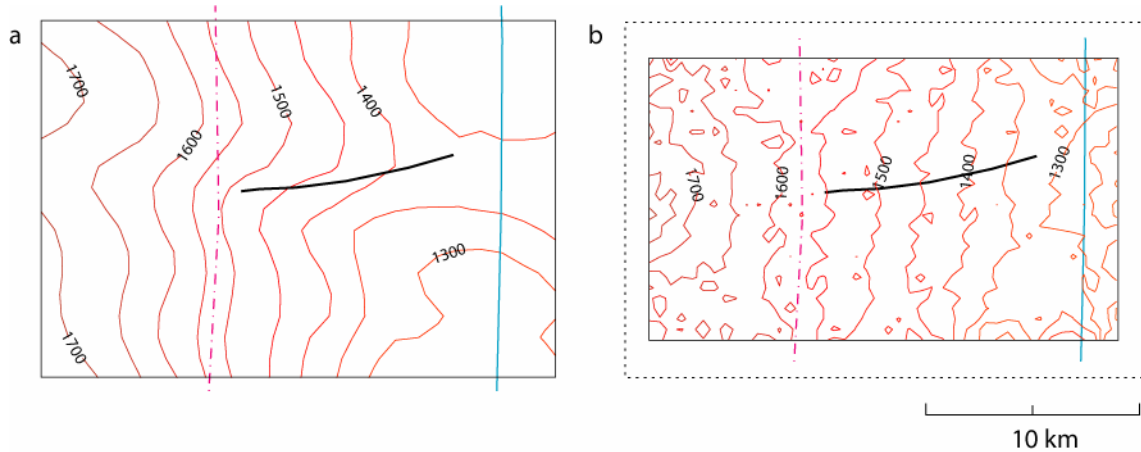


Figure 4.17 (a) Observed mean stresses for the boundary extended 4 km to the west. Contour interval is 50 kPa. (b) Mean stresses in the absence of a fracture simulated using remote stresses, $M_{xx} = 900$ kPa, $M_{yy} = 1800$ MPa, and $M_{xy} = -300$ kPa, and $\mathfrak{I} = 0.9$ (Table A.5). Elasticity constants were $\nu = 0.27$ and $E = 8000$ MPa (RMSE = 47). Contour interval is 50 kPa. The fracture trace drawn in each panel is for reference only. Refer to Figure 4.6 for an explanation about the dashed box.

Fracture Propagation Results

The propagation behaviors of the different fracture lengths— $s6$, $s4$, and $z2$ —were investigated by incorporating each separately as a boundary condition. The smaller boundary was used for *test fracture s6*. The extended boundary was used for *test fractures s4* and $z2$. Both fracture tips of each test fracture were active. Boundary stresses along each fracture were scaled to initiate propagation.

At the shortest length, *test fracture s6* did not propagate when $\mathfrak{I} = 0.8$ and $K_{IC} = 0.1$ MPa m^{1/2} (Table B.6) or when $\mathfrak{I} = 0.75$ and $K_{IC} = 0.3$ MPa m^{1/2} (Table B.8). The western tip propagated when $\mathfrak{I} = 0.75$ and $K_{IC} = 0.15$ MPa m^{1/2} ($K_I = 0.177$ MPa m^{1/2}, $K_{II} = 0.0$ MPa m^{1/2}, Figure 4.18, Table B.7). The western tip propagated ~1 km through the 4/5 suture zone before initiating a single episode of propagation at the eastern tip to

release accumulated shear stress along the fracture. The western tip continued to propagate as a mode I fracture.

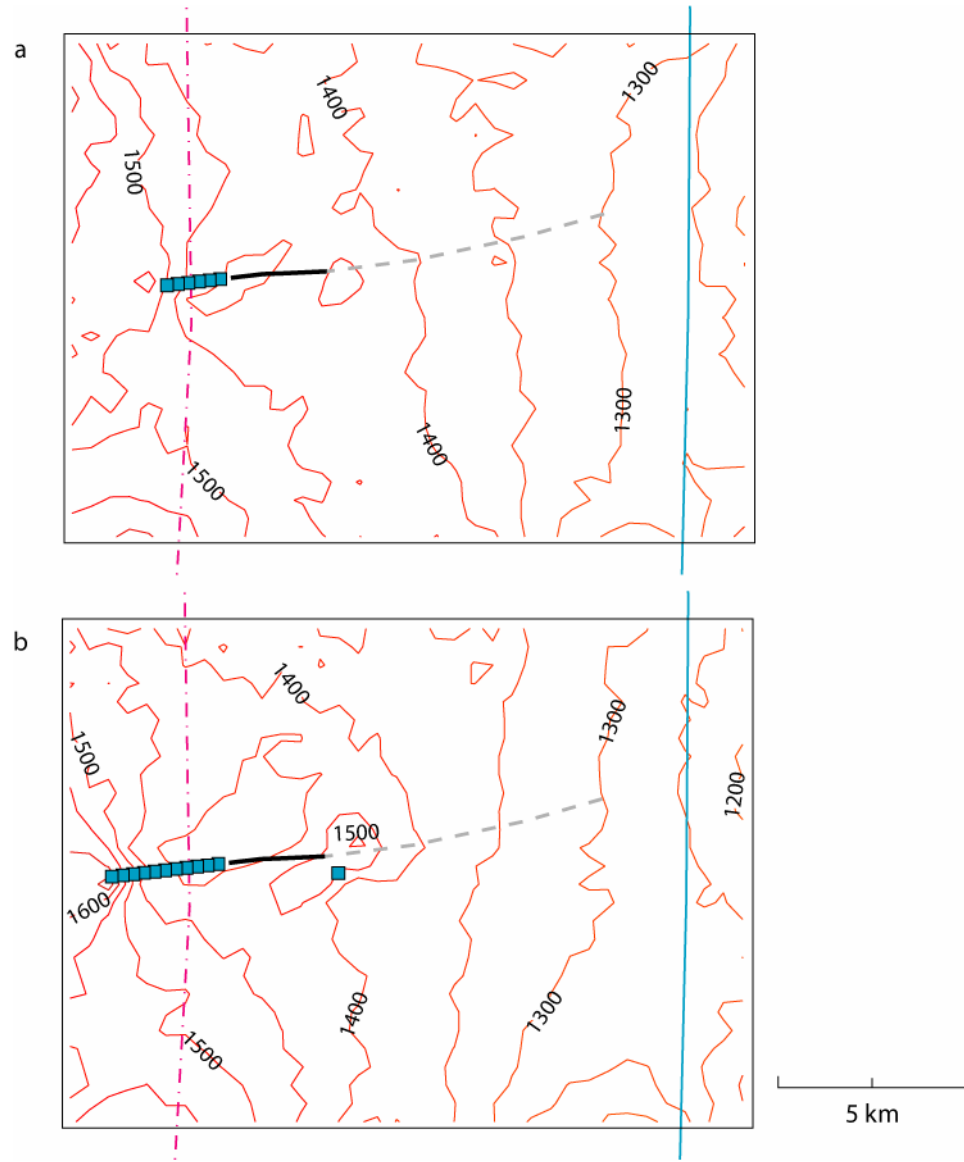


Figure 4.18 Experiment 3: Simulated propagation of *test fracture s6* and mean stresses within smaller model domain. The fracture toughness $K_{IC} = 0.15 \text{ MPa m}^{1/2}$ and $\mathfrak{I} = 0.75$ for the fracture boundary (Table B.7). (a) **Iteration 7.** (b) **Iteration 12.**

Test fracture s4, 2.4 km longer than *test fracture s6*, was investigated within the extended-boundary domain ($\mathfrak{S} = 0.9$ for domain stresses). When $\mathfrak{S} = 0.8$, which results in principal stresses along the fracture reduced by 11.1%, and $K_{IC} = 0.3 \text{ MPa m}^{1/2}$, *test fracture s4* propagated once at the eastern tip to relieve shear stress ($K_I = 0.245 \text{ MPa m}^{1/2}$, $K_{II} = -0.245 \text{ MPa m}^{1/2}$, and $\theta_0 = 53^\circ$). The western tip propagated 1.5 km through the 4/5 suture zone before arresting (Figure 4.19, Table B.9).

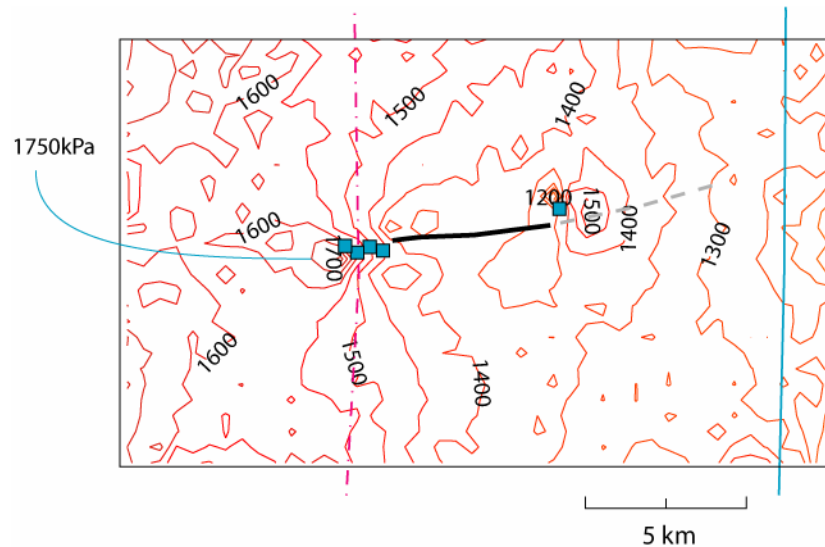


Figure 4.19 Experiment 3: Simulated propagation of fracture *s4* and mean stresses within extended-boundary domain. The fracture toughness $K_{IC} = 0.3 \text{ MPa m}^{1/2}$ and $\mathfrak{S} = 0.8$ (Table B.9). **Iteration 5.**

Unstable propagation of the western tip of *test fracture s4* and episodic propagation of the eastern tip occurred when $\mathfrak{S} = 0.75$, which results in principal stresses reduced by 17% ($K_{IC} = 0.3 \text{ MPa m}^{1/2}$, Figure 4.20, Table B.10). As the western tip approached the 4/5 suture zone ($K_I = 0.476 \text{ MPa m}^{1/2}$, $K_{II} = 0.575 \text{ MPa m}^{1/2}$), the eastern tip propagated twice before arresting (iteration 2, $K_I = 0.310 \text{ MPa m}^{1/2}$, $K_{II} = 0.980 \text{ MPa m}^{1/2}$). Figure 4.20a shows the mean stresses prior to the second period of episodic growth of the

eastern tip (iteration 6), which lasted for two iterations. The western tip propagated through the 4/5 suture zone and as fracture length increased (> 11 km), near-field stresses became concentrated at both fracture tips. Extensive deviatoric principal stresses at the western tip and small compressive principal stresses at the eastern tip (not shown) create a stress field favorable for growth at the eastern fracture tip (Figure 4.20b-c).

Because observed fractures propagate toward the eastern suture zone prior to propagating through the 4/5 suture zone, this test shows that the western tip must be inactive for eastward growth to occur. The western tip may be limited by upstream-pointing fracture geometry or inhomogeneities in the ice.

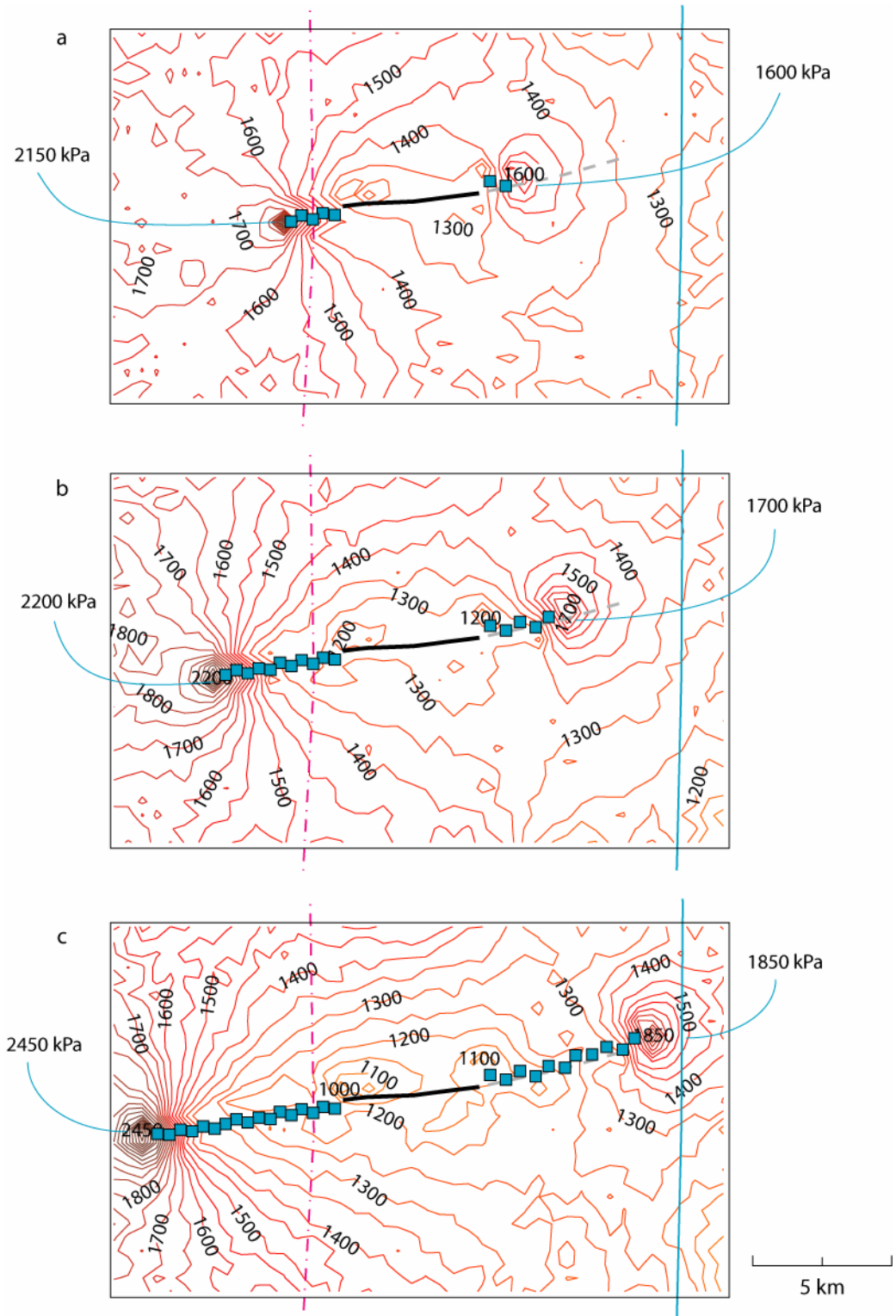


Figure 4.20 Experiment 3: Simulated propagation of *test fracture* s_4 and mean stresses within extended-boundary domain. The fracture toughness $K_{IC} = 0.3 \text{ MPa m}^{1/2}$ and $\mathfrak{I} = 0.75$ (Table B.10). (a) **Iteration 6.** (b) **Iteration 12.** (c) **Iteration 18.**

The last test in this experiment assumes that the starter fracture has propagated east the full observed extent. *Test fracture z2* is investigated within the extended-boundary domain. When $\mathfrak{S} = 0.85$, or reducing principal stresses 5.6% along the fracture boundary, the western tip propagated once to relieve shear stress ($K_{IC} = 0.3 \text{ MPa m}^{1/2}$, Figure 4.21, Table B.11). When $\mathfrak{S} = 0.8$, which results in principal stresses reduced by 11.1% along the fracture boundary, near-field shear stresses at the eastern tip remain important. The western tip propagated nearly 2 km through the 4/5 suture zone before initiating a single episode of propagation at the eastern tip to relieve accumulated shear stress along the fracture ($K_{IC} = 0.3 \text{ MPa m}^{1/2}$, Figure 4.22, Table B.12). Following this release of shear stress, the western tip continued to propagate until it reached the edge of the model domain.

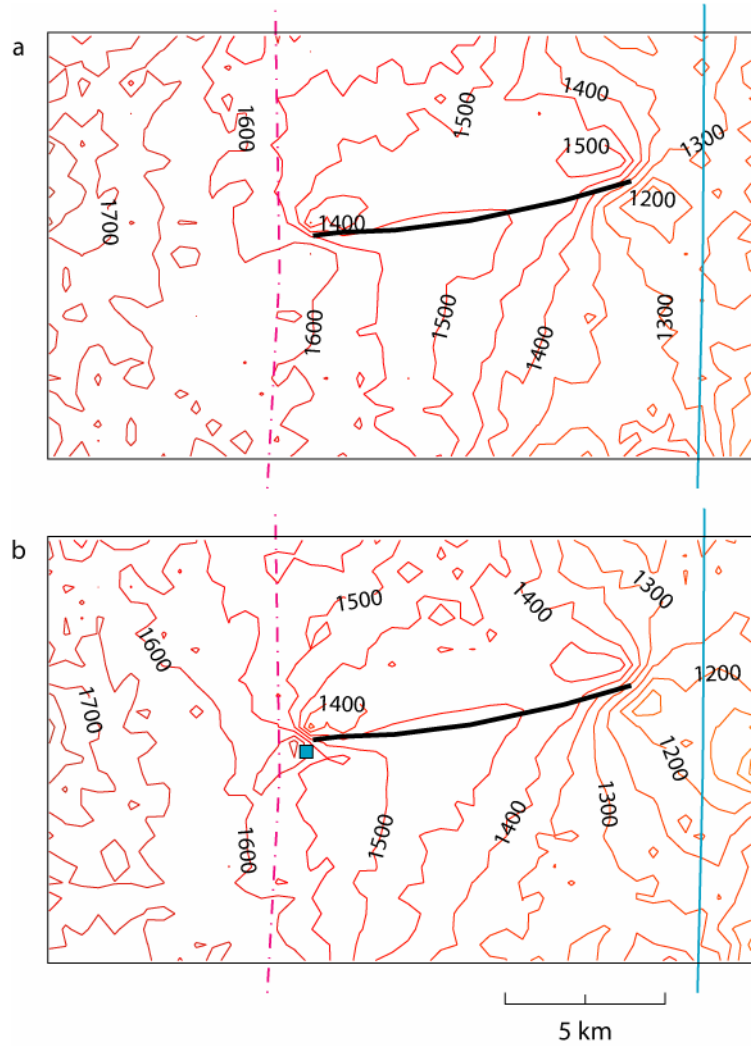


Figure 4.21 Experiment 3: Simulated propagation of *test fracture* z_2 and mean stresses within extended-boundary domain. The fracture toughness was $K_{IC} = 0.3 \text{ MPa m}^{1/2}$ and $\mathfrak{I} = 0.85$ (Table B.11). (a) **Iteration 1.** (b) **Iteration 2.**

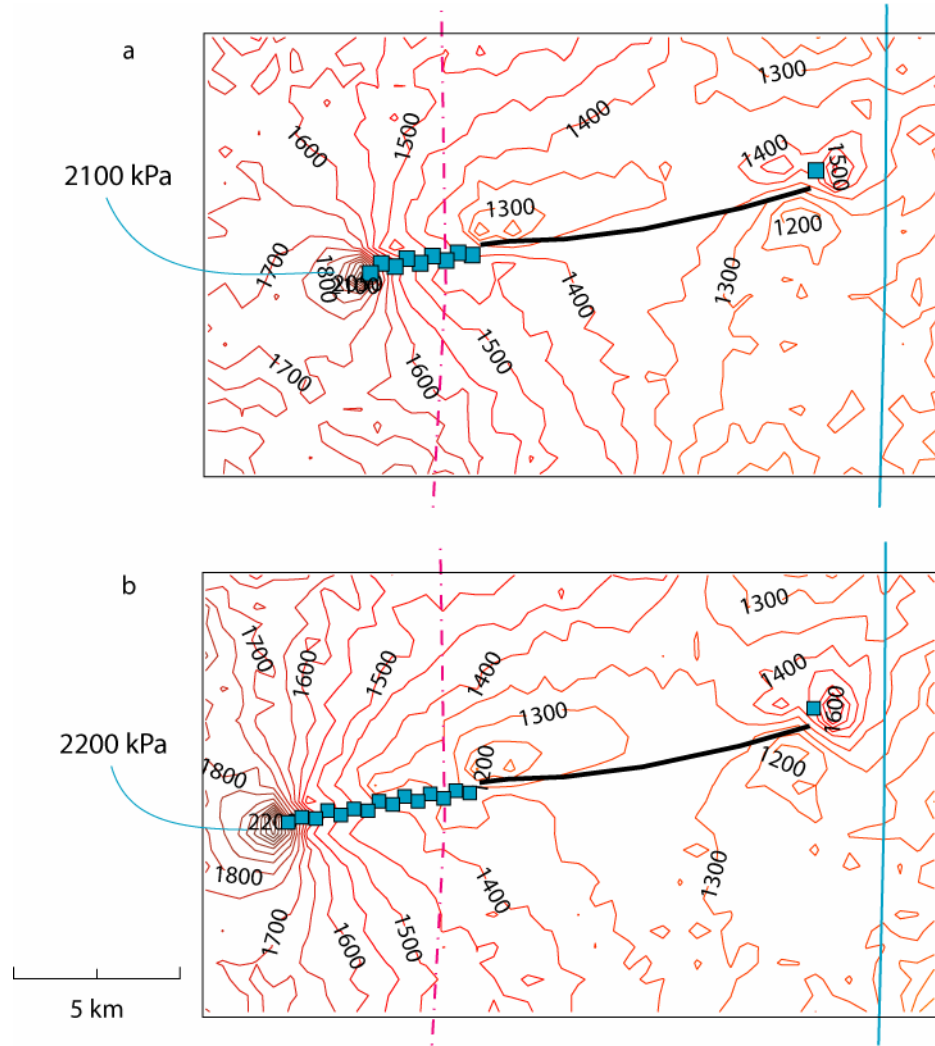


Figure 4.22 Experiment 3: Simulated propagation of *test fracture* z_2 and mean stresses within extended-boundary domain. The fracture toughness was $K_{IC} = 0.3 \text{ MPa m}^{1/2}$ and $\mathfrak{S} = 0.8$ (Table B.12). (a) **Iteration 10.** (b) **Iteration 16.**

4.4 Experiment 4

In *province D*, the 4/5 suture zone is breached by a few large fractures that propagate to the west. Near the shelf front, fractures may exceed 100 km in length. Here, we are interested in simulating the evolution of an observed fracture that is ~25 km in length and located ~185 km from the shelf front. *Fracture M0* is the first fracture observed to breach the 4/5 suture zone (Figure 4.23b). The objective of this experiment is to determine the stress conditions required to induce propagation through the 4/5 suture zone.

Experiment 4 is located at the upstream end of *province D* (Figure 4.2). The model boundary contains *test fracture N1*, which is defined using the endpoints and orientation of the observed *fracture N0* (~11 km upstream of observed *fracture M0*) and moving the fracture 10 km upstream (Figure 4.23a). Calibration of a second model boundary located 10 km downstream was unsuccessful (Tables A.7 and A.8). The model area is 1125 km².

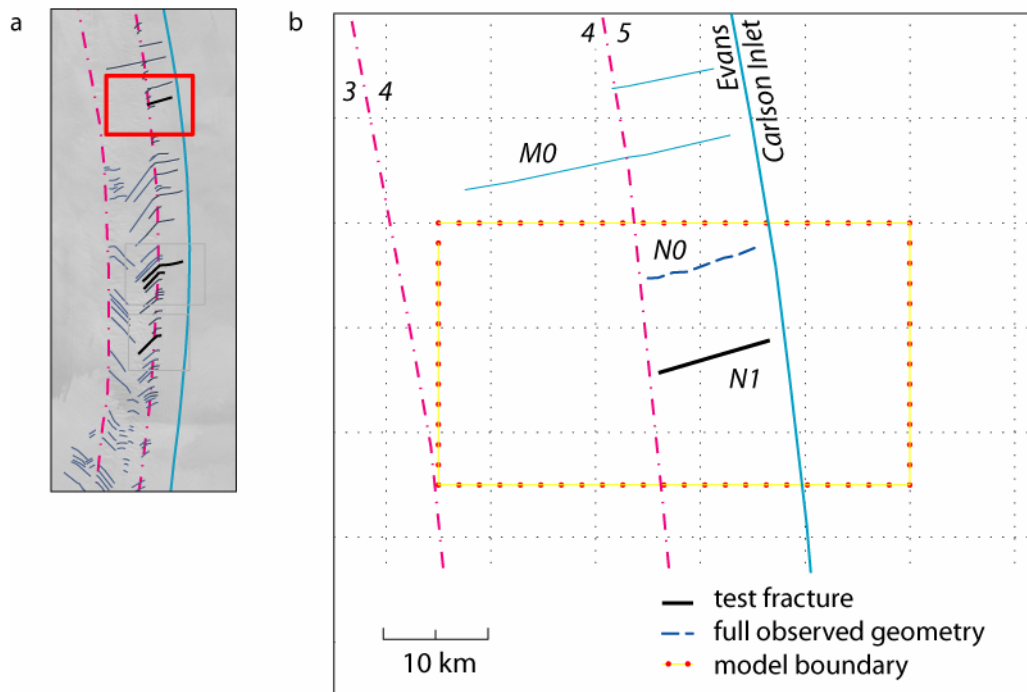


Figure 4.23 (a) Location of Experiment 4 in the ice shelf. (b) Model boundary showing *test fracture* *N1* in dark line, which is based on the observed *fracture* *N0* in dashed line. Observed *fracture* *M0* is labeled. The model boundary is represented by dotted lines, where the dots represent element endpoints.

The principal stresses in the surrounding ice shelf differ from the previous experiments (Figure 4.24). To the west of the model boundaries, lateral extensive principal stresses are relatively small. To the east, left-lateral shear is observed. The axis of *test fracture* *N1* is approximately aligned with compressive principal stresses.

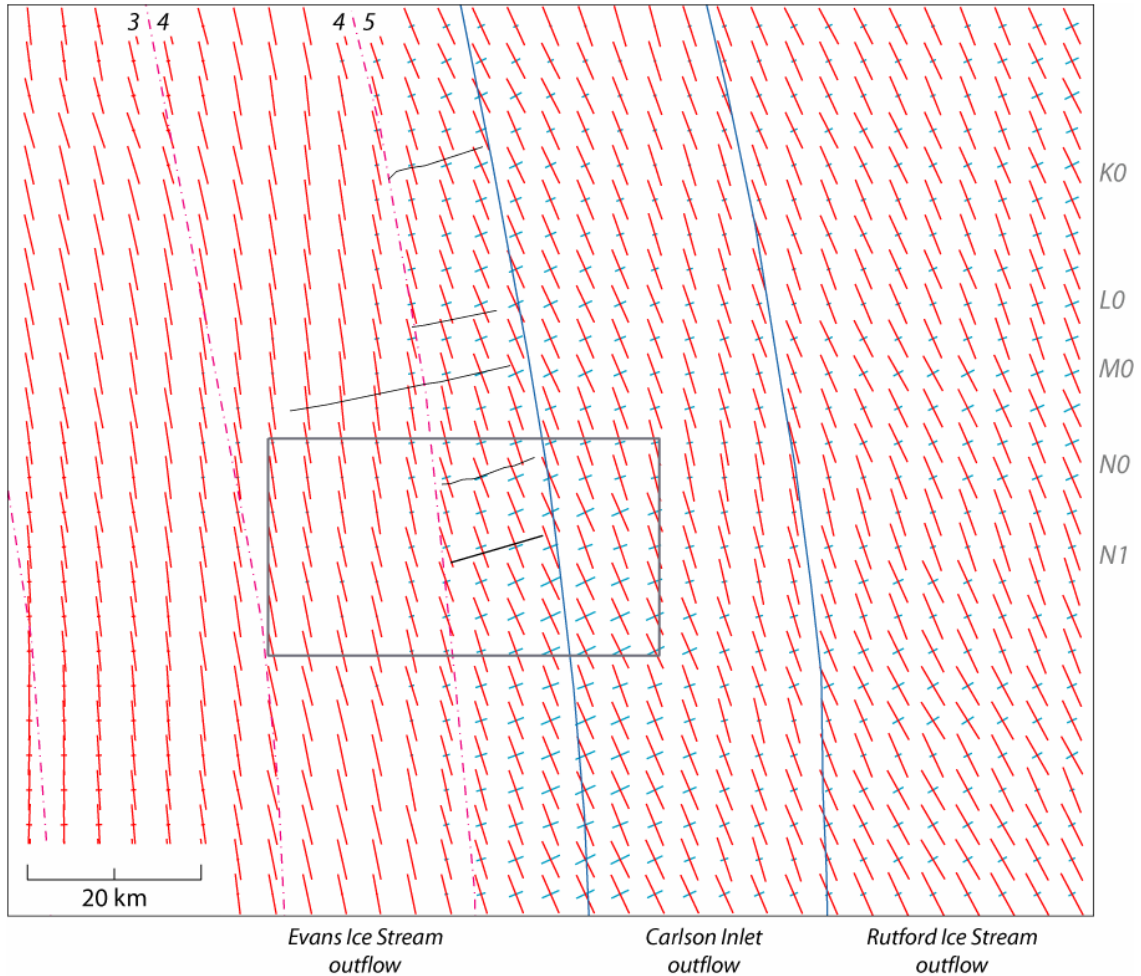


Figure 4.24 Experiment 4: Principal stress orientations and relative magnitudes (red: extensive, cyan: compressive). *Test fracture N1* is highlighted by straight line segment within model boundary (fracture labels at right of map). The *3/4* and *4/5* suture zones are labeled.

Experiment Calibration

Larger model boundaries become challenging to calibrate at this location, but are required to simulate propagation of larger fractures. Calibration of the model boundary required satisfying the general calibration criteria. Banding due to the non-random error in the velocity data is present in mean stresses for the boundary, becoming most noticeable along the shear margin. The remote stresses were $M_{xx} = 900$ kPa, $M_{yy} = 1800$

kPa, and $M_{xy} = -300$ kPa. For the boundary, $\mathfrak{I} = 0.85$. The best approximation of mean stresses that satisfied the calibration criteria was obtained using $\nu = 0.27$ and $E = 7500$ MPa (RMSE = 111, Figure 4.25b, Table A.6).

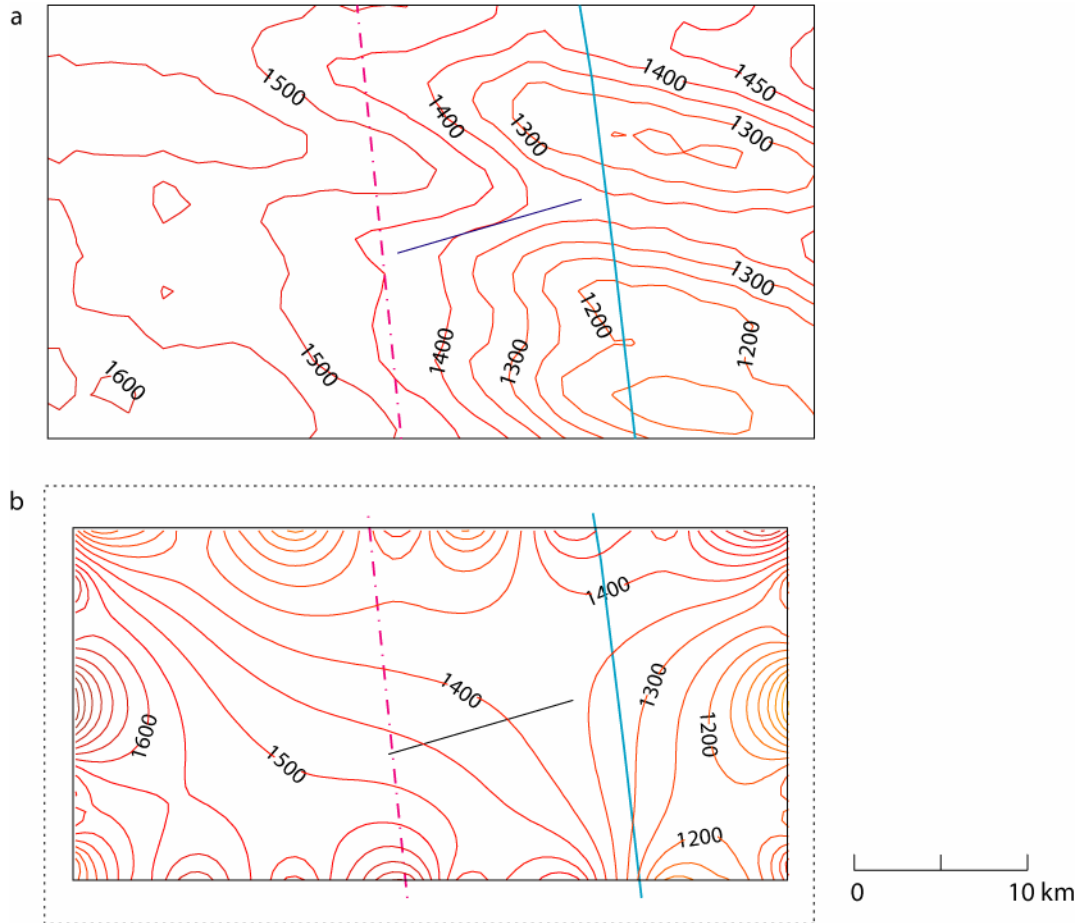


Figure 4.25 (a) Observed mean stresses. Contour interval is 50 kPa. (b) Mean stresses in the absence of a fracture simulated using remote stresses, $M_{xx} = 900$ kPa, $M_{yy} = 1800$ kPa, and $M_{xy} = -300$ kPa, and $\mathfrak{I} = 0.85$ (Table A.6). Elasticity constants were $\nu = 0.27$ and $E = 7500$ MPa (RMSE = 111). Contour interval is 50 kPa. The fracture trace drawn in each panel is for reference only. Refer to Figure 4.6 for an explanation about the dashed box.

Fracture Propagation Results

Fracture propagation was investigated by incorporating *test fracture N1* as a boundary condition. Both fracture tips were active and the fracture toughness K_{IC} was $0.3 \text{ MPa m}^{1/2}$. Boundary stresses along the fracture were scaled to initiate propagation. When $\mathfrak{S} = 0.8$, which results in principal stresses along the fracture reduced by 5.9%, the western tip of *test fracture N1* propagated once to relieve shear stress (Figure 4.26, Table B.13). Reducing principal stresses along the fracture by 11.8% ($\mathfrak{S} = 0.75$) caused unstable propagation of the western tip until it reached the model boundary and the episodic growth of the eastern tip as fracture length increased (Figure 4.27, Table B.14). In the first iteration, the western tip propagated ($K_I = 0.617 \text{ MPa m}^{1/2}$, $K_{II} = 0.878 \text{ MPa m}^{1/2}$) and the eastern tip grew one increment to relieve shear stress before arresting ($K_I = 0.350 \text{ MPa m}^{1/2}$, $K_{II} = 1.001 \text{ MPa m}^{1/2}$). Following this growth, the western tip propagated over 10 km. With each incremental increase in fracture length, the mode I stress intensity factor at the eastern tip increased until it was sufficient to exceed the mixed-mode propagation criteria (iteration 16, $K_I = 0.026 \text{ MPa m}^{1/2}$, $K_{II} = -0.786 \text{ MPa m}^{1/2}$). Then, the eastern tip of *test fracture N1* reinitiated propagation. Near-field stresses at the western tip remained more favorable to fracture growth than at the eastern tip. At iteration 25, the stress intensity factors were greater at the western tip ($K_I = 3.489 \text{ MPa m}^{1/2}$, $K_{II} = 1.268 \text{ MPa m}^{1/2}$) than at the eastern tip ($K_I = 0.651 \text{ MPa m}^{1/2}$, $K_{II} = 0.803 \text{ MPa m}^{1/2}$).

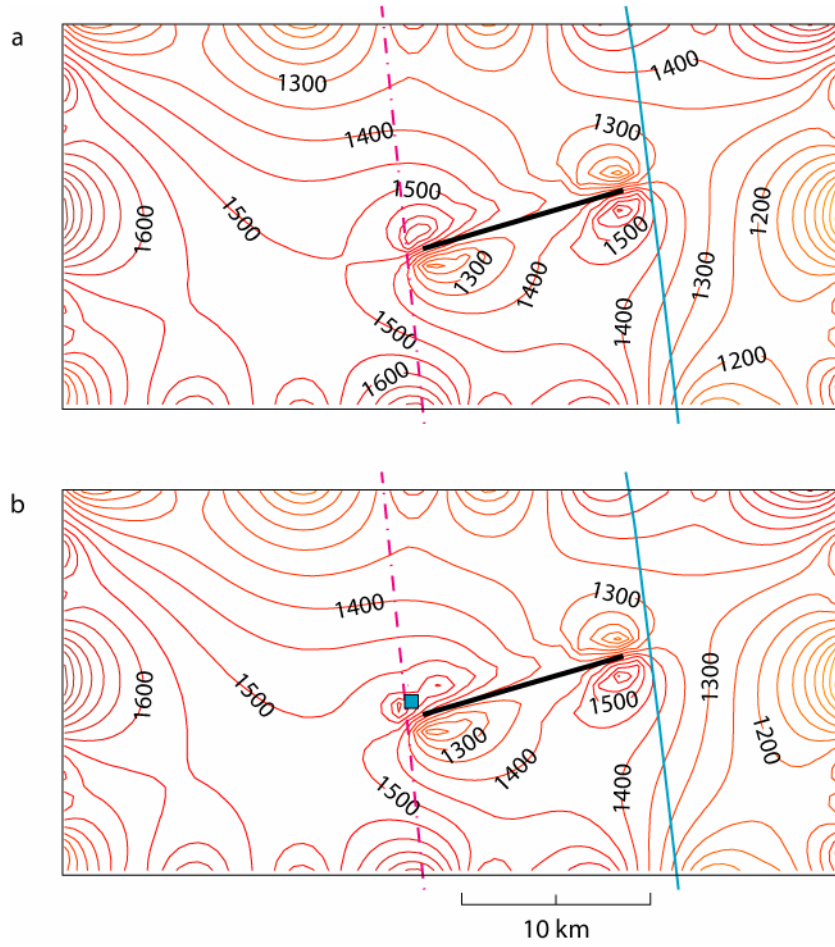


Figure 4.26 Experiment 4: Simulated propagation of *test fracture NI* and mean stresses within model domain. The fracture toughness was $K_{IC} = 0.3 \text{ MPa m}^{1/2}$ and $\mathfrak{S} = 0.8$ (Table B.13). (a) **Iteration 1.** (b) **Iteration 2.**

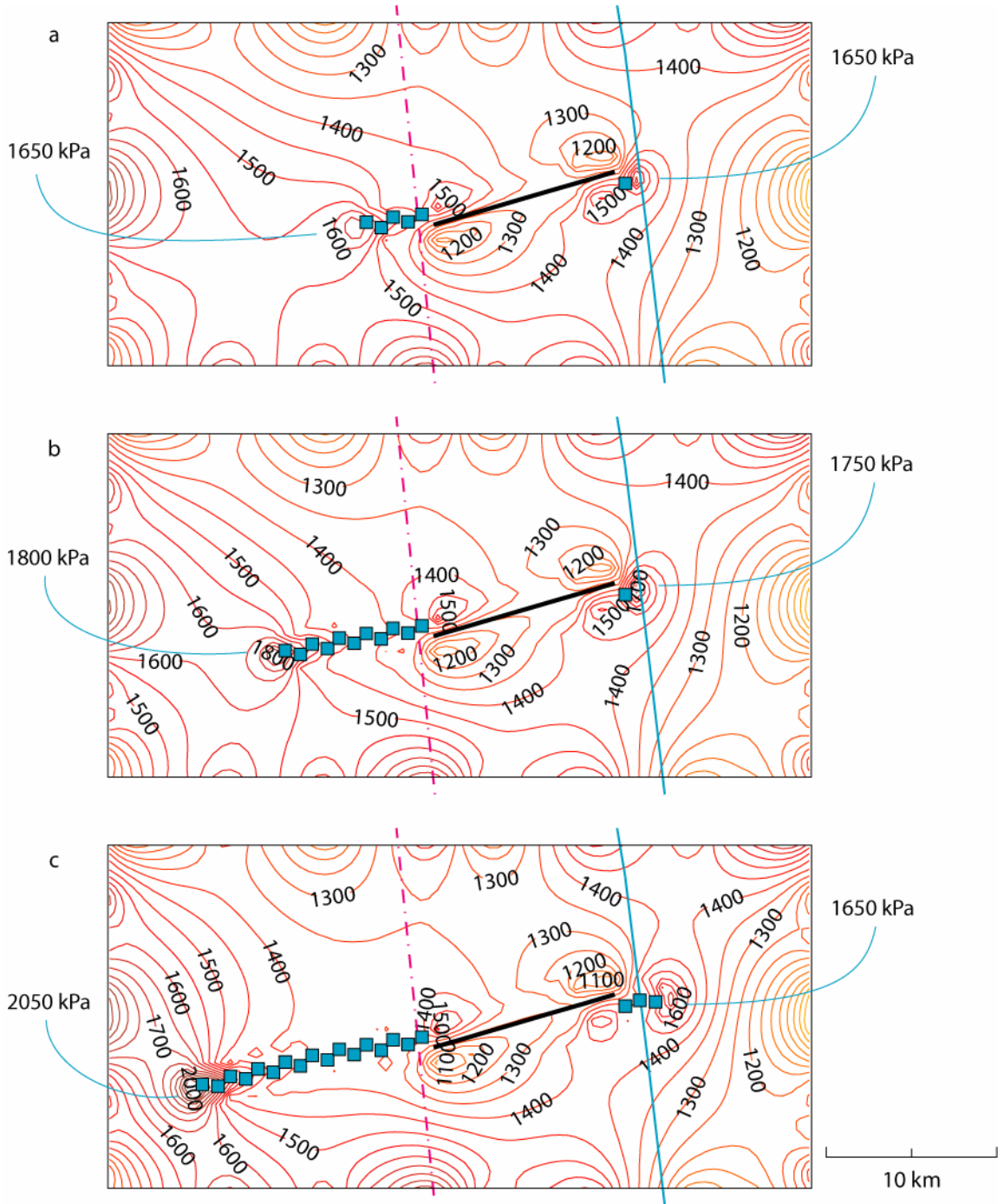


Figure 4.27 Experiment 4: Simulated propagation of *test fracture NI* and mean stresses within model domain. The fracture toughness was $K_{IC} = 0.3 \text{ MPa m}^{1/2}$ and $\mathfrak{I} = 0.75$ (Table B.14). (a) **Iteration 6.** (b) **Iteration 12.** (c) **Iteration 18.**

4.5 Experiment 5

Near the downstream end of *province D*, fractures are observed to propagate through several structural boundaries but still do not breach the Evans-Carlson suture zone. Near the shelf front, fractures may exceed 100 km in length. The objectives of this experiment are: (1) to determine the stress conditions required to induce propagation west through the ice shelf, (2) to simulate mechanical interaction between fracture tips, and (3) to assess the challenges in applying the model to a large domain near the ice-shelf front.

The downstream end of experiment 5 is located ~80 km from the shelf front in *province D*. In this location, two closely-spaced, subparallel fractures (~15 km separation) exceed 70 km in length. These features may extend through the full ~400 m thickness of the ice shelf. The upstream fracture is selected for investigation. Observed *fracture J0* is located ~90 km downstream of observed *fracture M0*, which was investigated in experiment 4, and ~95 km from the shelf front (Figure 4.28). *Test fracture J5* is defined as the easternmost 22 km of the observed *fracture J0*. To minimize boundary effects and increase the likelihood of successful calibration, the western side of the model boundary was selected to lie east of the western shear margin of the Ronne Ice Shelf. The model area is 6,000 km², over 5 times larger than the model area of Experiment 4. A second test was conducted to study mechanical interaction between *test fracture J7*, which is defined as the easternmost 35 km of the observed *fracture J0*, and *test fracture A4*, which is defined by placing the western 13 km of a

shelf-front corner fracture (left side of image in Figure 4.29) within the model domain at distance relative to *test fracture J7* that is similar to observations at the shelf front.

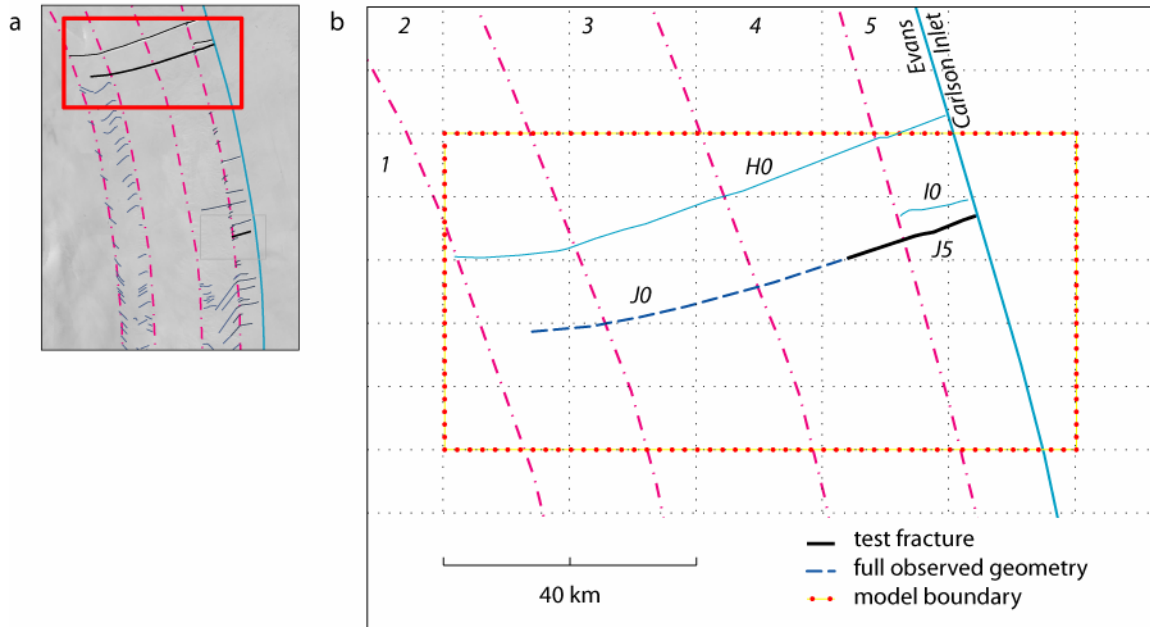


Figure 4.28 (a) Location of Experiment 5 in the ice shelf. (b) Model boundary showing *test fracture J5* in dark line, which is based on the observed *fracture J0* in dashed line. The model boundaries are represented by dotted lines, where the dots represent element endpoints.

At this location in the ice shelf, deviatoric principal stresses become relatively uniform, except near the margins and the shelf front (Figure 4.29), and effective strain is relatively small (Figure 4.30). The tips of observed *fractures H0* and *J0* are aligned with least extensive principal stress directions (deviatoric). As the fractures near the shelf front, deviatoric stress magnitudes decrease and more variability is observed. It is helpful here to view principal stresses due to full glaciological stress (Figure 4.31). The tips of observed *fractures H0* and *J0* remain aligned with least extensive principal glaciological stress directions. Lateral spreading is observed near the central front of the Ronne Ice Shelf, east of the Evans-Carlson suture zone in Figure 4.31.

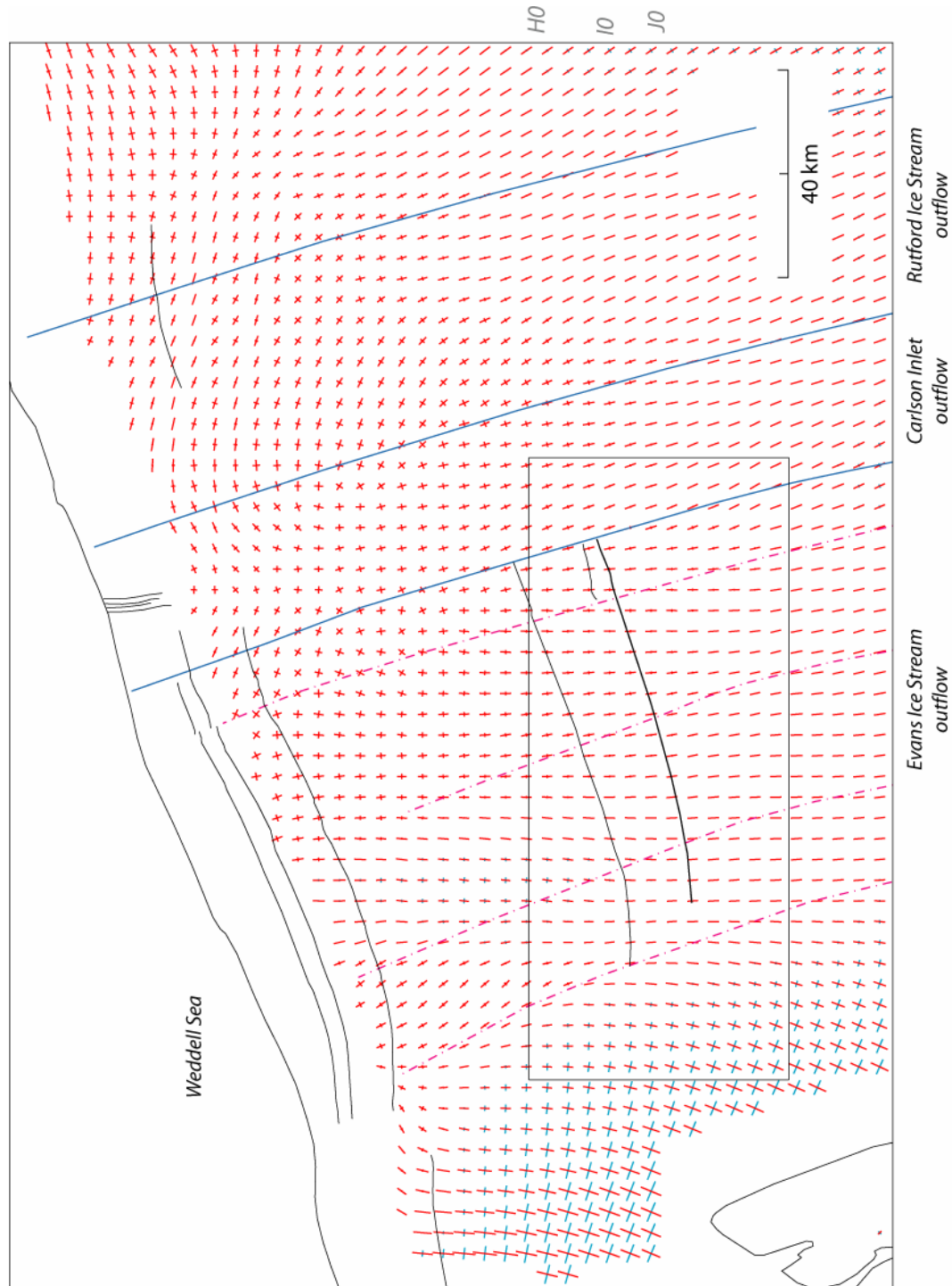


Figure 4.29 Experiment 5: Principal stress orientations and relative magnitudes for deviatoric stresses (red: extensive, cyan: compressive). *Observed fracture J_0* is highlighted (fracture labels at right of map).

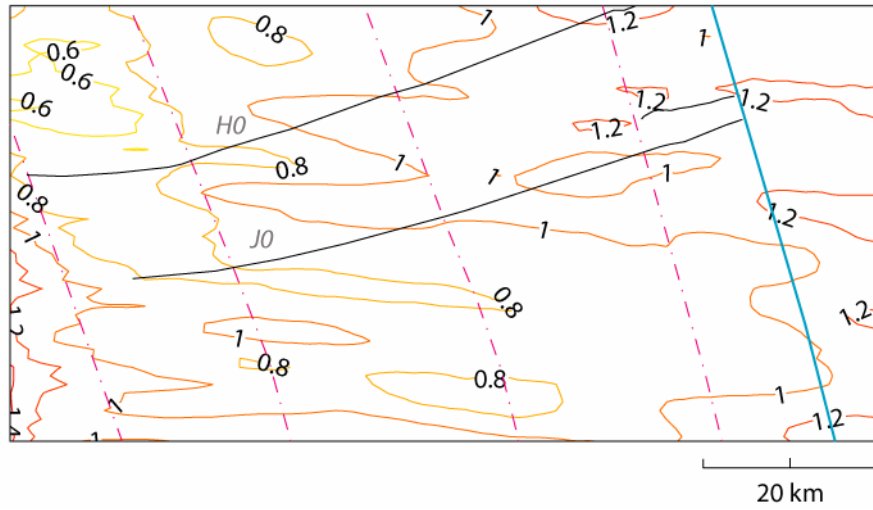


Figure 4.30 Experiment 5, effective strain rate, a^{-1} . The effective strain rate in this region of the ice shelf is relatively small.

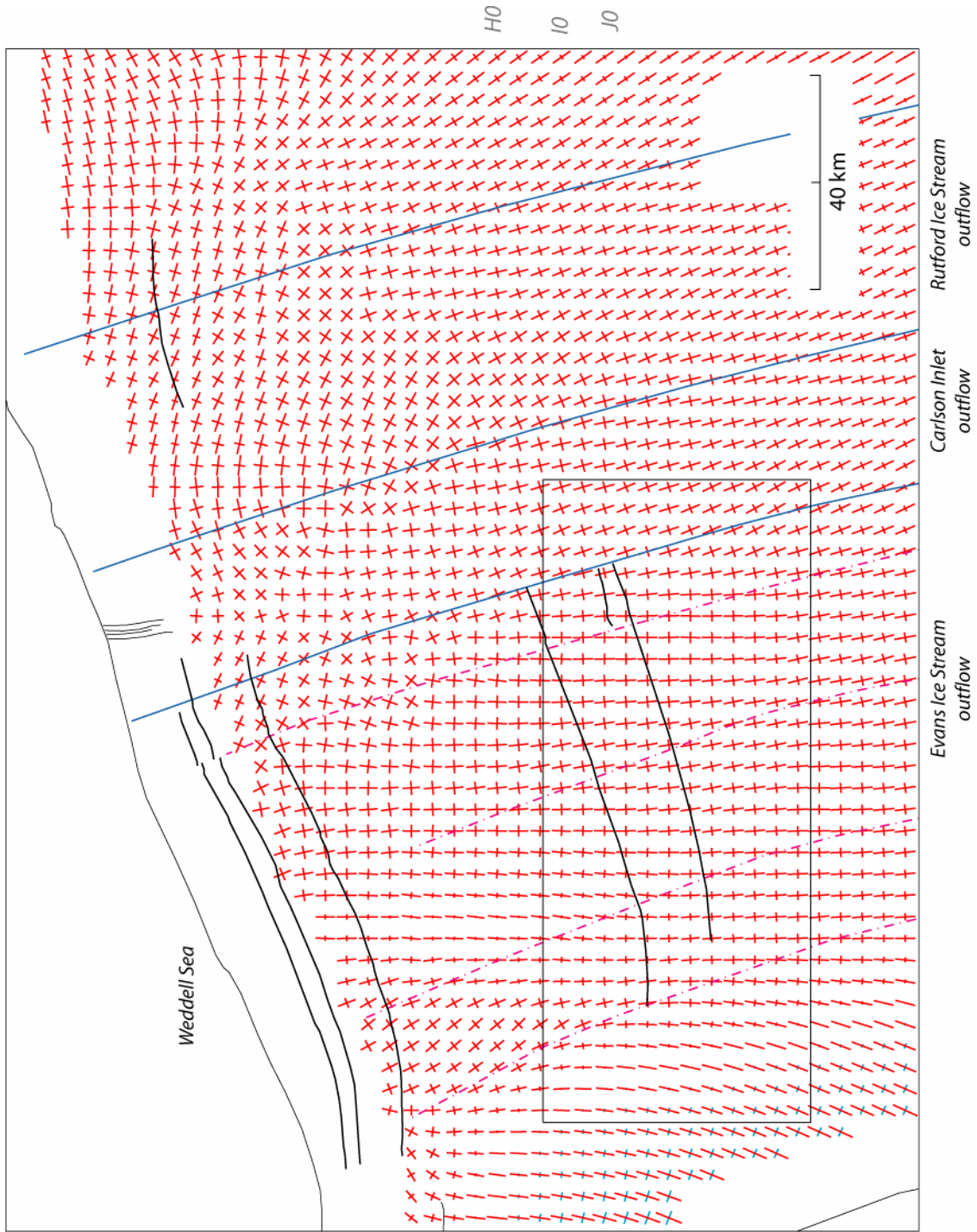


Figure 4.31 Experiment 5: Principal stress orientations and relative magnitudes for full glaciological stresses, deviatoric plus overburden pressure (red: extensive, cyan: compressive). (Fracture labels at right of map).

Experiment Calibration

Larger model domains can be challenging to calibrate because they span significant variations in shear stress. Here, the western boundary of the model domain is near the western margin of the Ronne Ice Shelf and the eastern boundary is near the Evans-Carlson suture zone. Calibration of the model boundary required: (1) minimizing boundary effects (high stress intensity concentrated along the boundary), and (2) generating a stress field with minimal variations in the eastern two-thirds of the model domain. The best approximation of mean stresses that minimized the boundary effects was obtained using remote stresses $M_{xx} = 900$ kPa, $M_{yy} = 1600$ kPa, and $M_{xy} = -100$ kPa (different from previous experiments) and scaling factor $\mathfrak{S} = 0.8$. The elasticity parameters were $\nu = 0.27$ and $E = 7500$ MPa (RMSE = 122, Figure 4.32, Table A.9). The average magnitude of the non-varying stress field was ~ 100 kPa lower than observed mean stresses, which was acceptable given the difficulty of calibrating the large boundary.

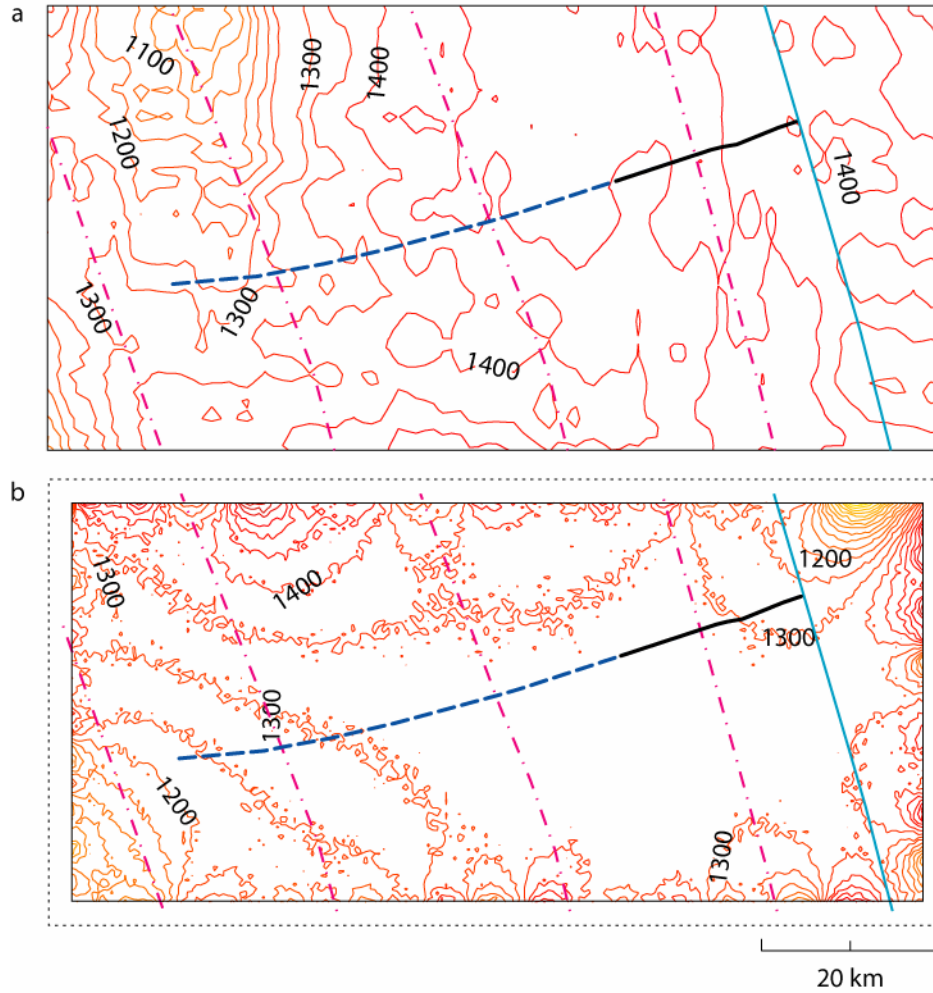


Figure 4.32 (a) Observed mean stresses. Contour interval is 50 kPa. (b) Mean stresses in the absence of a fracture simulated using remote stresses, $M_{xx} = 900$ kPa, $M_{yy} = 1600$ kPa, and $M_{xy} = -100$ kPa, and $\mathfrak{S} = 0.8$ (Table A.9). Elasticity constants were $\nu = 0.27$ and $E = 7500$ MPa (RMSE = 122). Contour interval is 50 kPa. The fracture trace drawn in each panel is for reference only. Refer to Figure 4.6 for an explanation about the dashed box.

Fracture Propagation Results

Fracture propagation was investigated by incorporating *test fracture J5* as a boundary condition. Both fracture tips were active and the fracture toughness K_{IC} was $0.3 \text{ MPa m}^{1/2}$. Boundary stresses along the fracture were scaled to initiate propagation. Using the best-fit model stress field ($\mathfrak{S}_{\text{fracture}} = \mathfrak{S}_{\text{boundary}} = 0.8$), both tips of *test fracture J5* propagated (Figure 4.33, Table B.15). In the first iteration, the stress intensity factors at the western tip ($K_I = 1.413 \text{ MPa m}^{1/2}$, $K_{II} = -0.442 \text{ MPa m}^{1/2}$) were greater than at the eastern tip ($K_I = 0.704 \text{ MPa m}^{1/2}$, $K_{II} = -0.176 \text{ MPa m}^{1/2}$). The mode I stress intensity factor at the eastern tip remained unchanged as the tip propagated through the eastern suture zone (recall that the suture zone is not represented in the model). The eastern tip propagated, adjusting orientation to form a gradual kink, until it reached the model boundary (iteration 17). As the western tip propagated and fracture length increased, the mode II stress-intensity factor at the western tip decreased, reaching zero as the total fracture length neared 70 km. *Test fracture J5* was also simulated with an inactive eastern tip, as observed in the ice shelf (Figure 4.34).

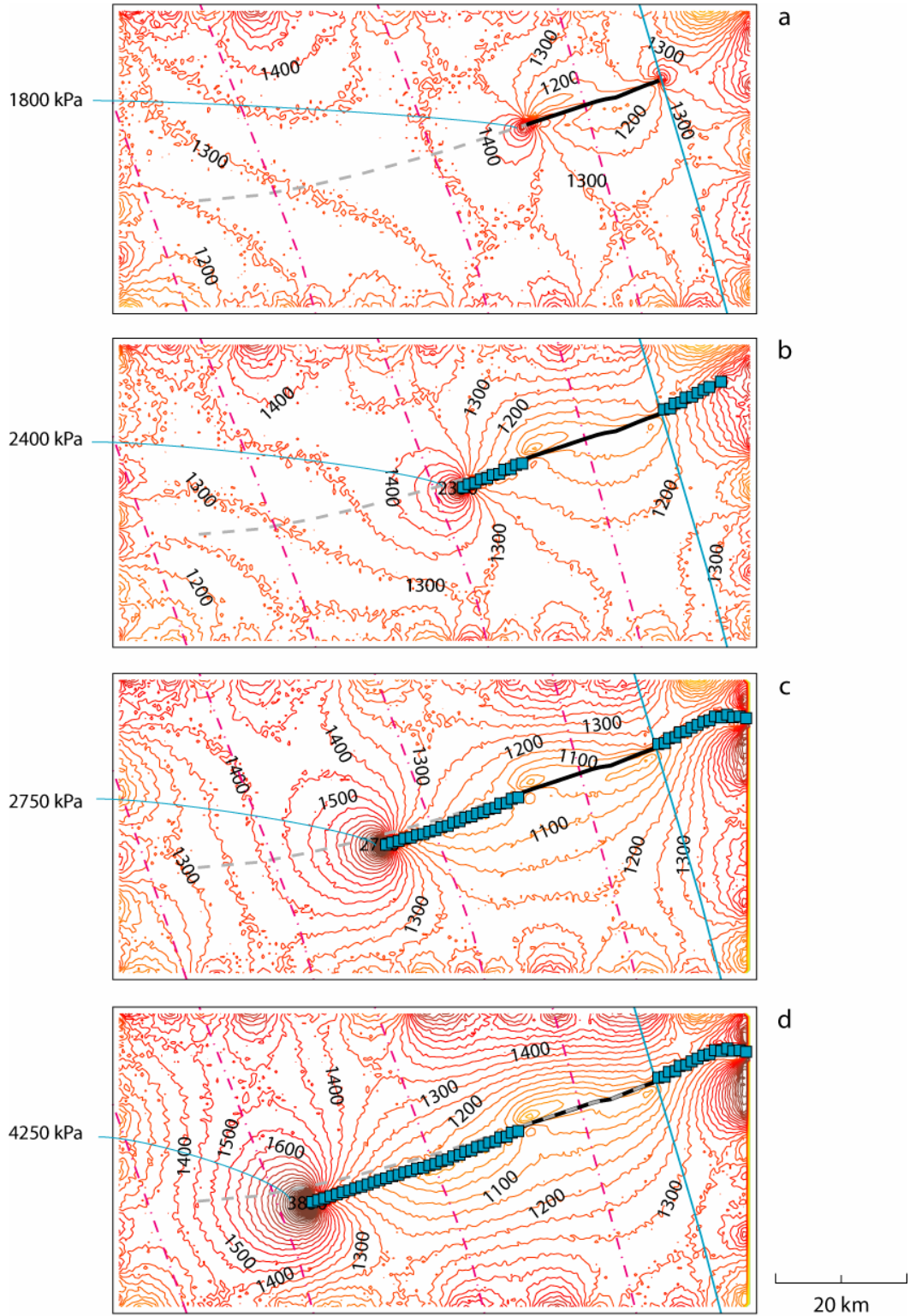


Figure 4.33 Experiment 5: Simulated propagation of *test fracture J5* and mean stresses. The fracture toughness was $K_{IC} = 0.3 \text{ MPa m}^{1/2}$ and $\mathfrak{I}=0.8$ (Table B.15). (a) **Iteration 1.** (b) **Iteration 12.** (c) **Iteration 24.** (d) **Iteration 36.**

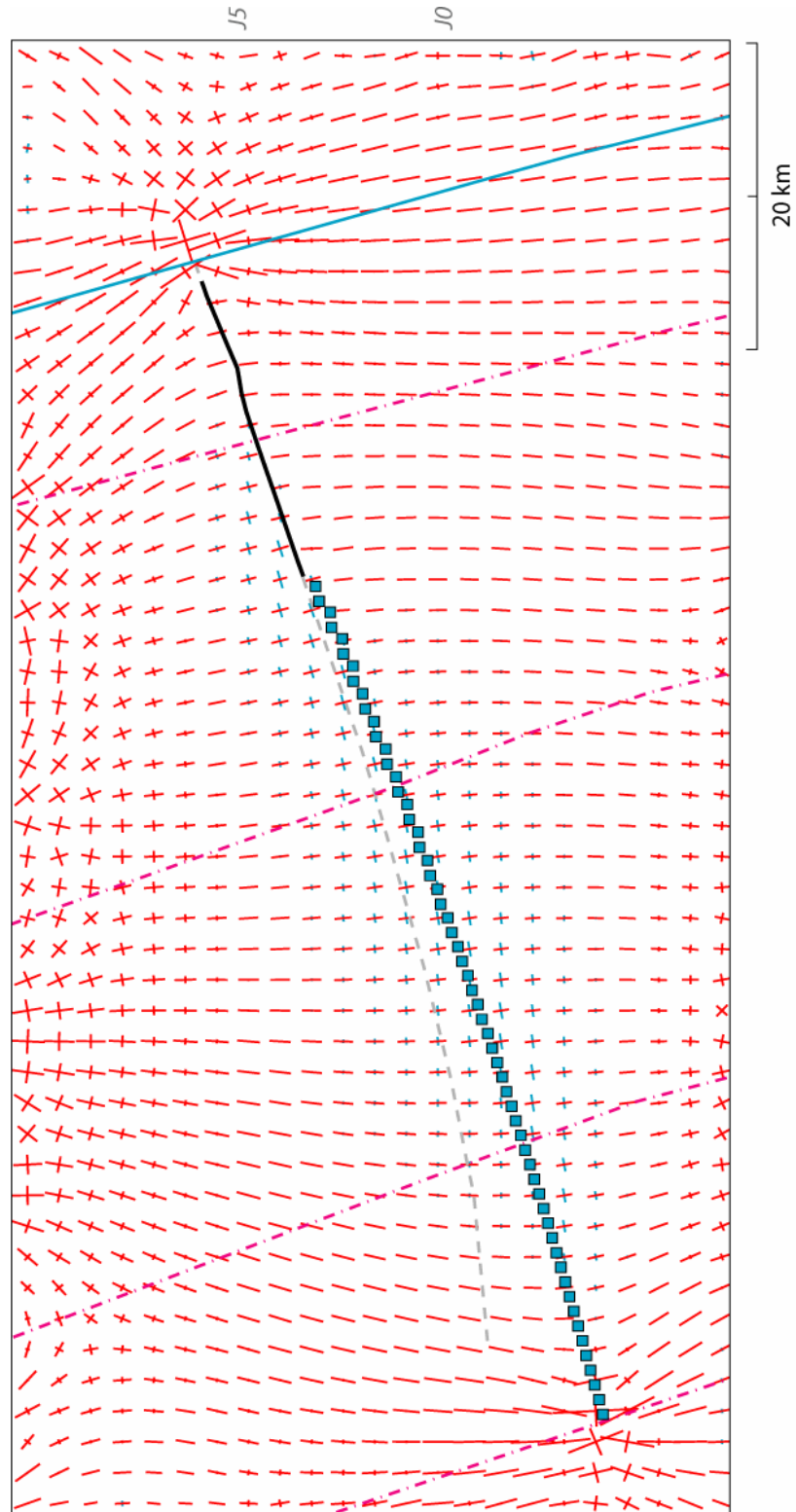


Figure 4.34 Experiment 5: Principal stress orientations and relative magnitudes for deviatoric stresses (red: extensive, cyan: compressive) based on simulation of *test fracture J5* and inactive eastern tip. (Fracture labels at right of map).

Using the same experiment setup ($\mathfrak{S}_{\text{fracture}} = \mathfrak{S}_{\text{boundary}} = 0.8$ and $K_{IC} = 0.3 \text{ MPa m}^{1/2}$), mechanical interaction between fracture tips was investigated by incorporating *test fractures J5* and *A4* as boundary conditions (Figure 4.35, Table B.16). In the first iteration, the eastern tip of *test fracture A4* propagated once to relieve shear stress, then arrested. Both tips of *test fracture J7* propagated. As the western tip of *test fracture J7* approached the eastern tip of *test fracture A4*, tensile stresses were induced in the vicinity of each other's tips (Figure 4.36). In response to the favorable stress conditions, the eastern tip of *test fracture A4* re-initiated growth. As the fracture tips overlapped, stress intensities increased and tensile stresses caused the tips to diverge (Figure 4.37). The highest stress intensity factors of the simulation were observed at the western tip of *test fracture J7* during this phase of interaction, consistent with large principal tensile stresses (Figure 4.38). As the test fractures continued propagating, stress intensities at the tips of *test fracture J7* increased until the tip intersected *test fracture A4*. *Test fracture A4* arrested.

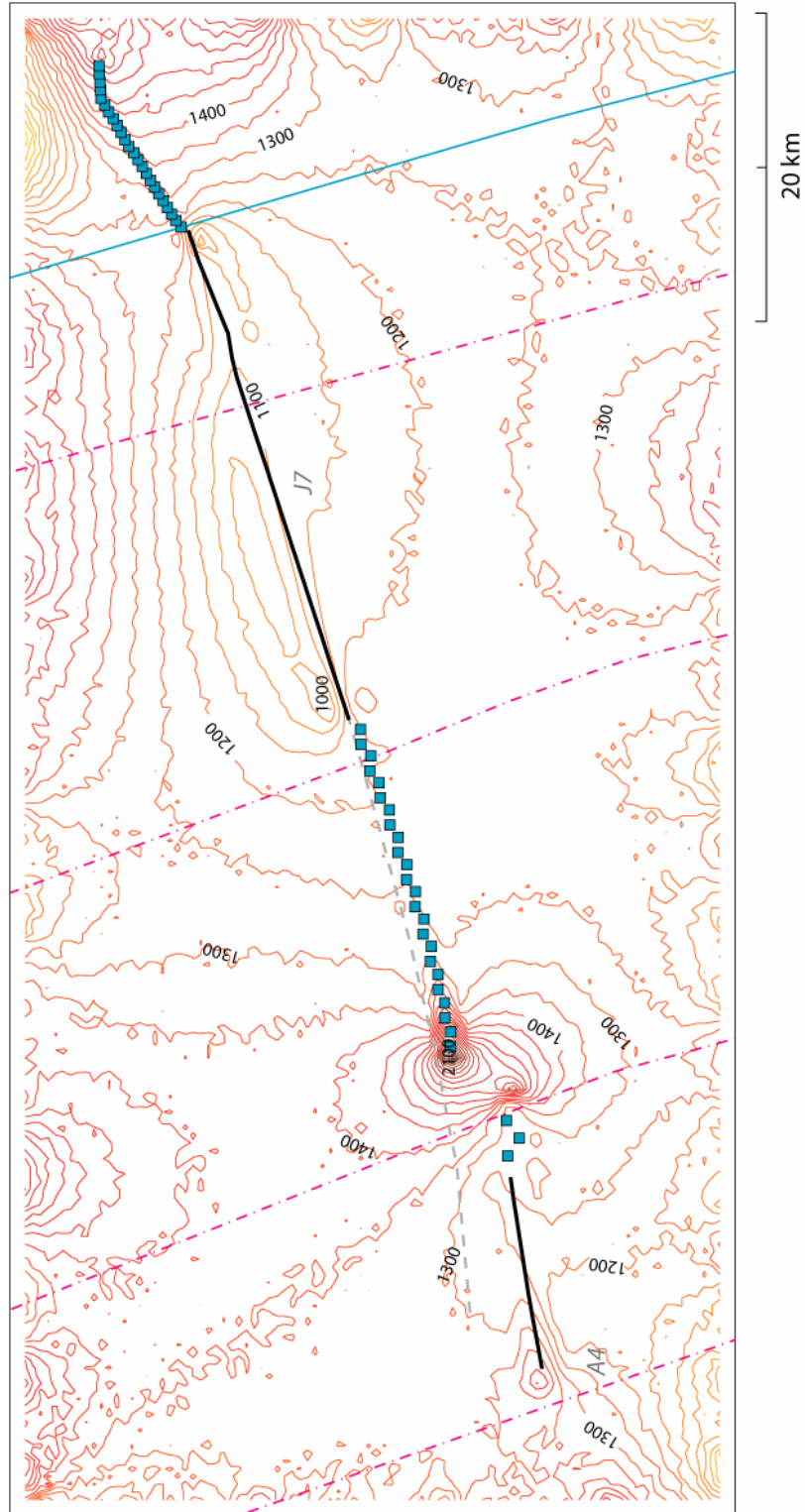


Figure 4.35 Experiment 5: Mean stresses and propagation based on simulation of mechanical interaction between *test fracture A4* and *J7*, **iteration 25**. The eastern tip of *test fracture A4* initiated growth as the larger *test fracture J7* approached it.

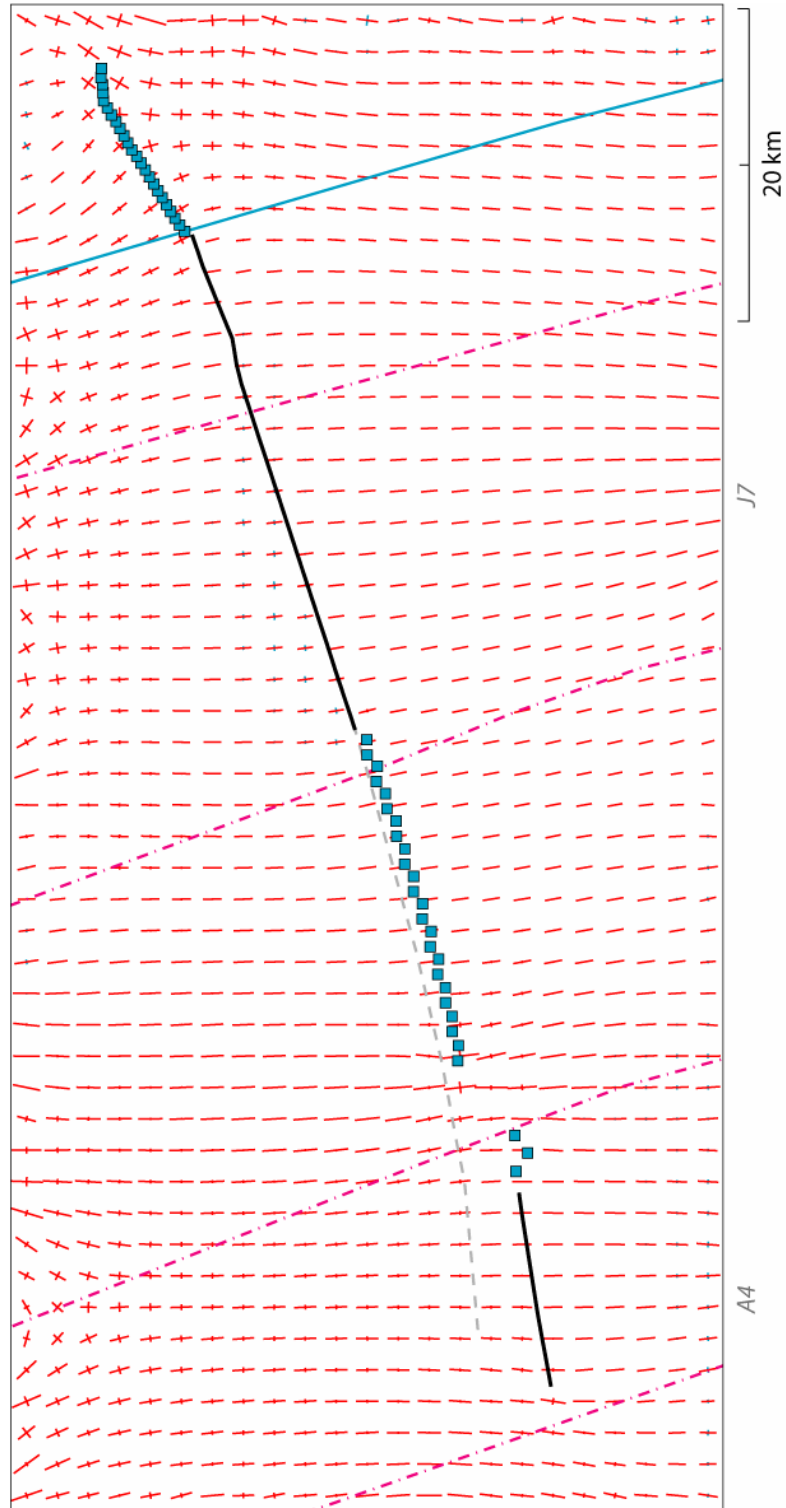


Figure 4.36 Experiment 5: Principal stress orientations and relative magnitudes for deviatoric stresses (red: extensive, cyan: compressive) based on simulation of mechanical interaction between *test fractures* A4 and J7, **iteration 25**. (Fracture labels at the bottom of the map).

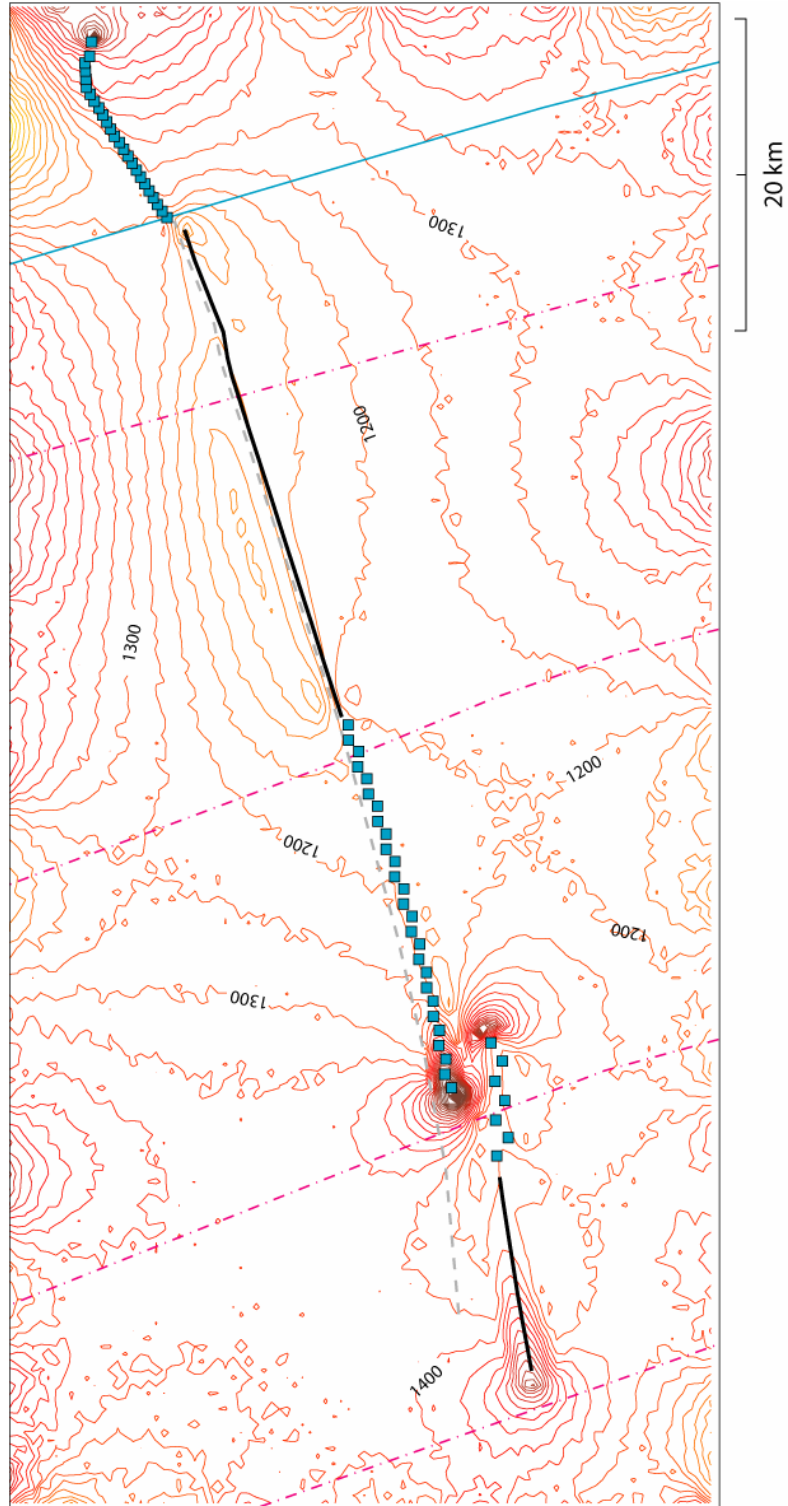


Figure 4.37 Experiment 5: Mean stresses and propagation based on simulation of mechanical interaction between test fractures A4 and J7, **iteration 28**.

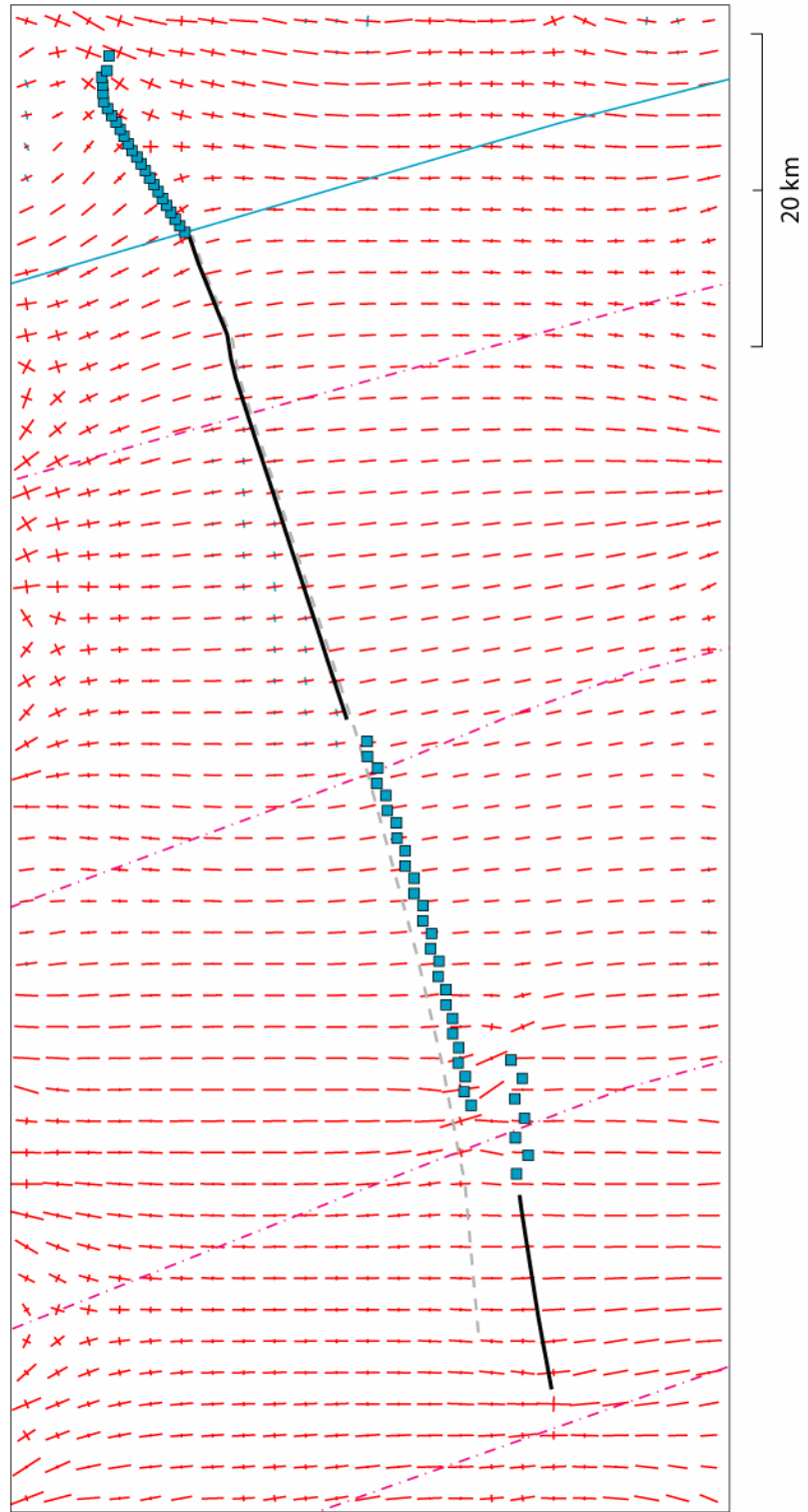


Figure 4.38 Experiment 5: Principal stress orientations and relative magnitudes for deviatoric stresses (red: extensive, cyan: compressive) based on simulation of mechanical interaction between *test fractures* A4 and J7, **iteration 28**.

5 Discussion

The fracture mechanics models developed here allow the hypothesis that structural boundaries within the Ronne Ice Shelf play an important role in fracture propagation to be tested. They also demonstrate other important aspects of fracture propagation in the ice shelf environment. The discussion has three parts: (1) experimental evidence for the role of structural boundaries in crack tip arrest, (2) other insights gained from the model experiments, and (3) limitations in model implementation.

5.1 Role of Suture Zones

Suture zones that form where shear margins from adjacent ice streams merge become structural boundaries within the ice shelf into which the streams flow. These boundaries appear to influence the horizontal propagation of fractures in the ice shelf (tips are observed to arrest at these boundaries). Mapped fractures and structural boundaries show that propagating fractures arrest near prominent suture zones in the Ronne Ice Shelf (Figure 5.1). That mapped fractures arrest at the suture zone formed by the Evans and Carlson Inlet flows—and do not propagate through this boundary until within 50 km of the shelf front—suggests that material properties within this suture zone must be important in crack tip arrest. To the west, the 4/5 zone contains highly fractured ice from the eastern shear margin of the Evans Ice Stream (*tributary 5a*). Few fractures in *province D* are observed to propagate west through the 4/5 suture zone, and in no case does westward propagation occur before the eastern fracture tips reach the suture zone formed by the Evans and Carlson Inlet flows.

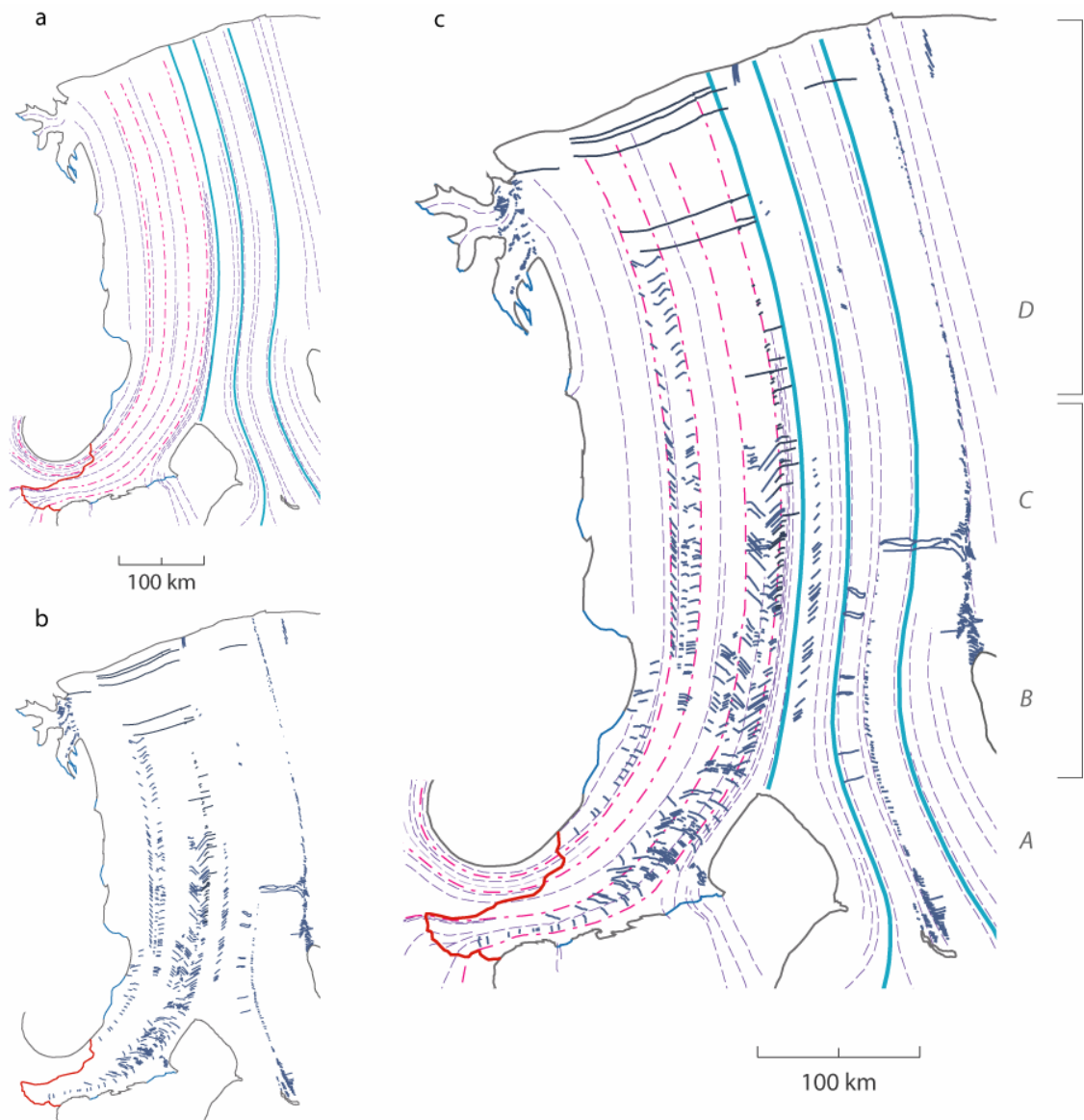


Figure 5.1 Outflow from Evans Ice Stream and neighboring ice streams (left to right: Carlson Inlet, Rutford Ice Stream, and Institute Ice Stream). (a) Structural boundaries. (b) Fractures. (c) Structural boundaries and fractures. Letters correspond to provinces of similar fracture geometry. Brackets identify upstream and downstream fracture groups.

Suture zones are clearly associated with the arrest of propagating fracture tips. Yet in each experiment, unless localized shear stress arrested growth, fractures did not arrest

in suture zone locations (Table 5.1). Because the models use far-field glaciological stresses and associated material properties (variations due to the presence of a suture zone are not treated) we can infer that suture zones play an important role in fracture mechanics within the ice shelf. Experiments further show that fracture lengths in *province D* (>60 km for *test fracture J5*) generate tip stress intensities that would be sufficient to continue propagation (Table 26), but tip arrest is observed near the *1/2* suture zone (Figure 4.30). In the absence of suture zones, fractures propagate. We thus conclude that these structural boundaries in the ice must be responsible for the observed crack tip arrest.

Table 5.1 Experiments that demonstrate the importance of suture zones in fracture tip arrest. In these experiments, test fractures do not arrest at the Evans-Carlson suture zone.

Experiment Number	Test Fracture	Province	Figure Reference
1	<i>k1</i>	B	4.7b
2	<i>j3</i>	C	4.13b
3	<i>s4</i>	C	4.21c
4	<i>N1</i>	D	4.29c
5	<i>J5</i>	D	4.33c

There are two possible roles for suture zones in crack tip arrest. First, enhanced shear within these suture zones may reduce the mode I stress intensity at fracture tips. Second, past shear experienced by this ice may modify its mechanical properties (fracture toughness, elasticity constants). Near the surface, cold air ponds in crevasses, cooling the ice and making it more brittle while at depth, the ice may be relatively warm and less brittle due to its shear history (Harrison et al., 1998). The ice fabric may have a preferred crystal orientation due to its strain history. Once a crack tip has arrested at a

suture zone, microfracturing in the process zone (to dissipate energy when propagation is not possible) may further modify ice rheology.

When tip arrest occurs, three outcomes are possible. First, the tip arrests and the fracture becomes a passive feature in the shelf, possibly filling in with wind-blown snow. Second, propagation may initiate at the other tip of the fracture. Third, if neither tip is able to propagate but the propagation criterion is satisfied, the fracture may increase the displacement between fracture walls (greater width), which may indirectly lead to vertical propagation.

Examples of vertical propagation to relieve stress where lateral propagation is not possible are observed in the outflow of the fast-flowing Rutford Ice Stream. Here, fractures form downstream of two grounded features—Korff Ice Rise and Kershaw Ice Rumples (Figure 5.2). Fractures formed at the downstream end of Korff Ice Rise advect away from the ice rise, forming a crevasse train that becomes a structural boundary in the shelf. Large fractures on the western side of the boundary are not observed to propagate through it. Instead, longitudinal stretching appears to “open” the fractures, some of which penetrate the full thickness of the ice shelf. A similar scenario is observed downstream of Kershaw Ice Rumples.

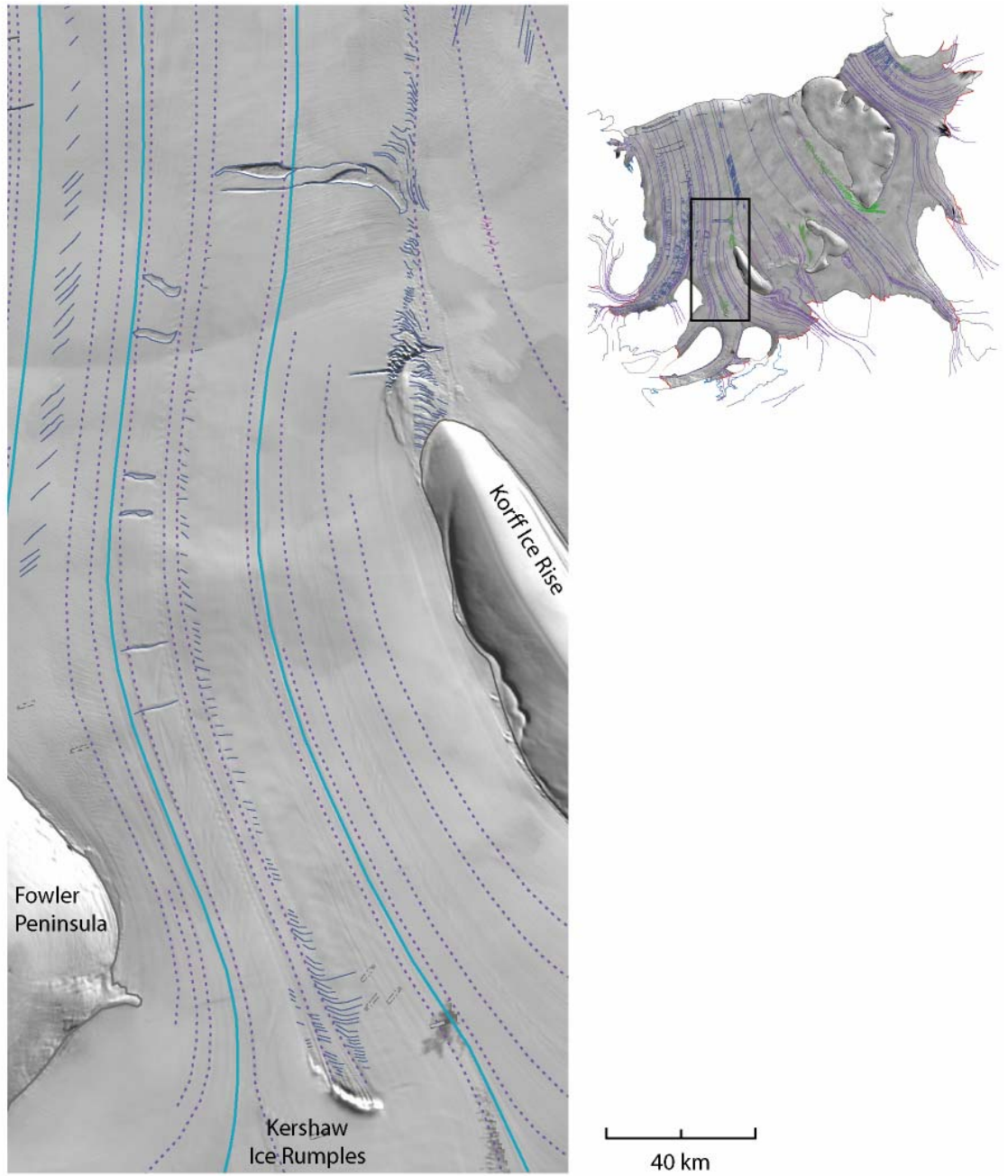


Figure 5.2 Crevasses at the downstream ends of Kershaw Ice Rumples and Korff Ice Rise, in the outflow of the Rutford Ice Stream. Shadows cast by the northern walls fall on a rift-filling mélange of sea ice and snow.

5.2 Other Insights

The fracture propagation experiments yield other interesting details about fracture propagation in the ice shelf. These details include the following: shear at the fracture tips, modification of near-field stresses by adjacent fractures, the role of fracture length in episodic propagation, controls on propagation near the shelf-front, and what it means when stresses along the fracture are scaled from best-fit model stresses ($\mathfrak{I}_{\text{fracture}} < \mathfrak{I}_{\text{boundary}}$).

Fracture Mechanics

The fracture tip propagates in an orientation determined by stress-intensity factors at the tip. For a pure mode I fracture, in-plane growth occurs ($\theta = 0^\circ$). A pure mode II fracture will propagate at $\pm 70.5^\circ$ to the existing fracture plane. The growth orientation of a mixed-mode fracture lies between these two angles. A special mixed-mode case occurs when $|K_I| = |K_{II}|$, in which case the growth orientation is $\pm 53.13^\circ$ to the existing fracture plane. In response to shear stress, the fracture endpoints may propagate at abrupt angles that depend on the sense of shear (left- or right-lateral; Figure 5.3a, b). Left-lateral shear, which is consistent with the eastern suture zone, is observed in the propagation behavior of *test fracture z2* (Experiment 3; Figure 5.3c or Figure 4.24). Right-lateral shear, which becomes relatively more important near the shelf front, is observed in the propagation of *test fracture N1* in (Experiment 4; Figure 5.3d or Figure 4.29). When fractures are small (<20 km), experimental results suggest that shear

induced by fracture growth may lead to arrest of a propagating tip, as in *test fracture s6* (Experiment 3; Figure 4.19c). Smaller scale spatial variation in shear may cause a small adjustment to tip geometry as the fracture seeks optimal orientation with respect to principal stresses, as in Experiment 3's *test fracture s4* (Figure 4.20) and *test fracture z2* (Figures 4.23 and 4.24).

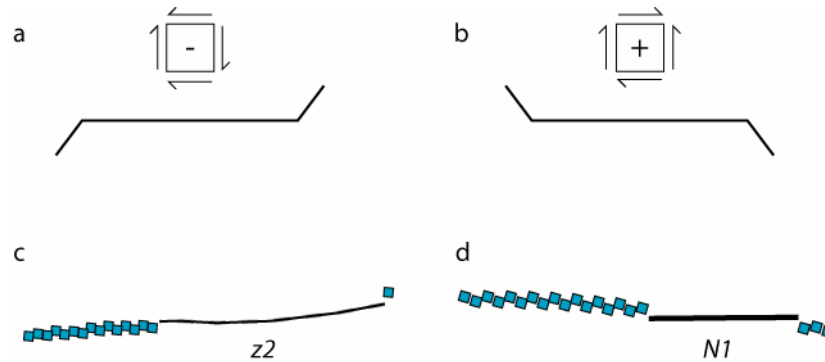


Figure 5.3 Propagation orientation of fractures subject to shear stress. (a) Left-lateral shear. (b) Right-lateral shear. (c) Left-lateral propagation of *test fracture z2*, rotated and scaled. (d) Right-lateral propagation of *test fracture N1*, rotated and scaled.

The change in propagation direction may be abrupt, as in *test fracture z2* (Figure 5.3c or Figure 4.24) or gradual, as in *test fracture J5* (Figure 4.29 or 4.33). Observed *fracture J0* has a gradual curve at its western tip that is consistent with right-lateral shear. This is the result of shear near the western margin of the ice shelf. The simulated fracture has only a gradual reorientation. The western margin was not part of the model domain.

To understand mechanical interaction among fractures, we must consider conservation of energy. Adjacent fractures of equal lengths must share the available propagation energy G_i . This energy is identical for both fractures but less than that for

an isolated fracture in the same far-field stress field (Pollard and Aydin, 1988). Indirect evidence of mechanical interaction among fractures is provided by *test fracture k1* (Experiment 1; Figure 4.7). Simulated stresses at the upstream-pointing tip of the isolated test fracture are large enough for continued growth but the observed fracture does not propagate in the ice shelf. We infer that the inhibited growth is due to the effect of many closely-spaced, adjacent fractures in this area (refer to *province C* in Figure 3.10).

As the length ratio between the two fractures increases, the propagation energy of the longer fracture approaches that of an isolated fracture, while the energy of the shorter fracture approaches zero (Pollard and Aydin, 1988). Experiment 2 provides direct evidence of this stress shadow effect. The eastern tip of *test fracture g6* is in the “shadow” cast by the longer *test fracture j3*, enabling the latter to act as an isolated fracture (Figure 4.13b, Table 15). This effect depends on the relative fracture lengths and orthogonal spacing, among other factors.

As the length of the lead fracture increases, the propagation of more distal fractures is inhibited and spacing increases between fractures allowed to propagate (Pollard and Aydin, 1988). Indeed, fracture spacing increases in *province D*, where orthogonal spacing approaches $\sim 1.5a$ for $a = 35$ km (observed *fractures H0* and *J0*, Figure 4.28b). For this spacing, observed *fractures H0* and *J0* are treated as a “set” of fractures, as are the set of three fractures at the shelf front (Figure 4.31). Given the stress shadow effect, it is curious that observed *fractures H0* and *J0* are so closely spaced. They may have been of similar lengths and propagated together as they advected through the shelf.

Propagation would be inhibited for distal fractures in the shadow cast by the *HO* and *JO* set. A similar stress shadow may be cast by the fractures at the shelf front. As the fractures continue to advect through the shelf, two events may occur: (1) the downstream fracture of a set may become longer (more favorable stress conditions), casting its own shadow on the upstream fracture (as in observed *fracture HO* on *JO*), or (2) with proximity to the shelf-front, stress conditions may be large enough to allow even “small” fractures, those arrested at the 4/5 suture zone, to propagate.

Mechanical interaction between fracture tips may enhance or inhibit fracture propagation. Experiment 5 provides direct evidence of enhanced propagation behavior (Figures 4.35-4.38). Another test conducted using variations of these fractures by setting them at similar lengths resulted in inhibited growth within the same model domain (not shown).

Fracture length plays an important role in continued propagation and re-initiation of growth at an arrested tip. Episodic propagation, growth characterized by tip arrest followed by re-initiation, may occur when fracture length increases, near-field stresses change, or ice material properties change. Two experiments demonstrate the role of fracture length in episodic propagation, Experiment 3 (*test fracture s4*, Figure 4.21) and Experiment 4 (*test fracture N1*, Figure 4.29). The latter experiment is a likely scenario of growth re-initiation in the ice shelf. Here, the eastern tip propagated once to relieve shear stress and then arrested. Although the eastern tip had arrested, the fracture lengthened due to propagation of the western tip. Increases in fracture length steadily

increased the mode I stress intensity (propagation energy) at the eastern tip until it was large enough for propagation to re-initiate and maintain growth.

Near the shelf front, glaciological stresses are large enough to propagate fractures without requiring stresses along the fracture to be scaled from best-fit model stresses. In simulations of lateral propagation, this may be due to several factors: relative homogeneity of ice thickness along the fracture (Figure 5.4) and propagation energy associated with large fractures (~21 km for *test fracture J5*, Figure 5.4). In addition, near-shelf front rifts extend through the full ice thickness. These rifts may contain seawater, which enhances propagation (Larour et al., 2004; Scambos et al., 2000).

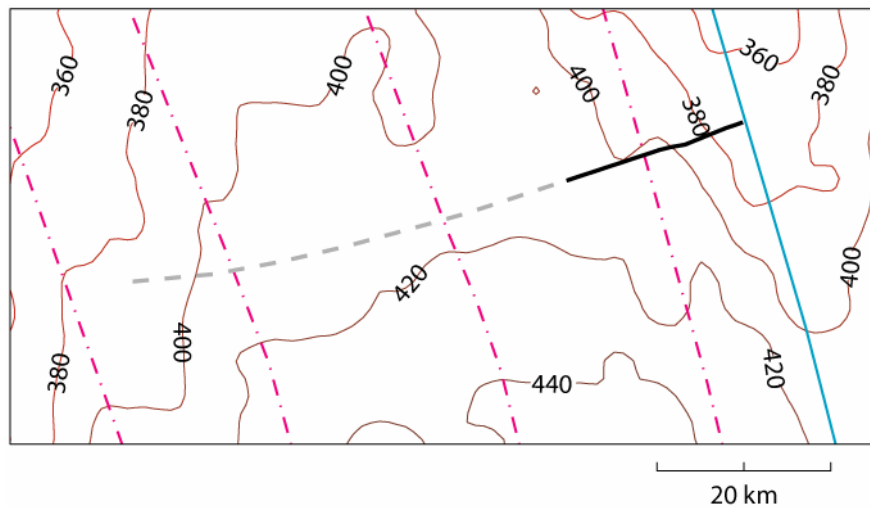


Figure 5.4 Ice shelf thickness. Contour interval is 20 m. Observed *fracture J0* in gray dashed line; *test fracture J5* in black solid line. The fracture trace and suture zone drawn in the panel are for reference only.

When principal deviatoric stresses are modified by a factor \mathfrak{I} , what does $\mathfrak{I}_{\text{fracture}} < \mathfrak{I}_{\text{boundary}}$ mean? First, for a mode I fracture, mean normal stresses decrease along the fracture axis, concentrating at the fracture tips (Pollard and Segall, 1987, p.

312). Thus, some decrease in stress magnitude from the best-fit model stresses may be expected and we do observe that principal stresses decrease along the length of a simulated propagation. Second, we do not consider any stress shadow effects that may be due to adjacent fractures outside the model, effects that would also modify stresses along the fracture.

5.3 Model Implementation

Model implementation is limited by error in the observational data used to initialize each model, assumptions required by the numerical method, and imperfections in the calibration of model parameters. The non-random error in the velocity data required a smoothing filter, implemented using a 20 km x 20 km square window size. Noise was greatly reduced but some banding persists. A single inverse rate factor was used in all experiments, though it may vary across the study area (Larour et al., 2005). Similarly, elasticity constants were assumed constant for any given experiment.

The most important requirements for model implementation are that model assumptions must be satisfied and calibration successful. We assume that LEFM adequately describes the propagation of fractures in the ice shelf (that is, that the viscous component of ice deformation may be ignored). This is reasonable because near the surface (most fractures in this study are not through-cutting) and on medium-length time scales (days to months), glacier ice behaves elastically and undergoes brittle fracture at sufficiently large stresses (compressive stresses close fractures at depth, ignoring basal fractures). To study lateral propagation of fractures, the plane strain

assumption is reasonable because the horizontal shelf geometry, or even the width of an ice stream outflow, is much greater than the ice thickness. The steady-state assumption, which permits the study of the evolution of a set of fractures, is reasonable due to agreement between flow features and velocity azimuths.

Successful calibration of each model requires careful boundary selection. The presence of shear stresses makes boundary selection challenging in some locations. For example, the boundary for Experiment 5 had to be selected to lie east of a shear zone, limiting the model area but making simulation possible. Model area was also limited in *province C* due to locally large shear stresses ($|\sigma_{xy}| \geq 0.5|\sigma_{xx}|$). In the present work, for model areas $< 1000 \text{ km}^2$, an acceptable RMSE score typically followed the guideline:

$$RMSE \leq 0.14qA \quad [5.1]$$

in which the model area A has units of km^2 and the constant q is 1 km^{-2} . For larger model areas, an RMSE value below 130 is acceptable. These guidelines may be useful in implementing the model at another location in the Ronne-Filchner Ice Shelf, or in another ice shelf.

6 Conclusions

Ice shelves around Antarctica are characterized by abundant fractures (see, for example, the MOA <http://nsidc.org/data/moa>). A subset of these fractures become the planes along which large, tabular icebergs calve. Calving is the primary means of ice mass loss in the Antarctic and on large ice shelves and tabular iceberg calving is the dominant form of calving. Of interest then is to understand how an initial population of fractures evolves to become the large near-front rifts along which tabular icebergs calve, in particular what limits their propagation. The Ronne Ice Shelf is an ideal location for this study due to its simple flow history. We conclude from the experiments presented here that the far-field “glaciological” stress is sufficient to drive horizontal propagation in most locations but that propagation is limited by structural boundaries in the ice shelf and modification of the stress field by adjacent fractures.

The large fractures we track from near the grounding line to the shelf front are the fractures that become the planes along which tabular icebergs calve (for example, icebergs A43 and A44 in the year 2000). For most of their evolution, fracture propagation is limited by inhomogeneities in the shelf. Only near the front do fractures grow to lengths required to produce large icebergs. The same spatiotemporal pattern is observed for large rifts near the central shelf front.

An important goal in studying the propagation of ice shelf fractures is the development of a “calving criterion” that can be used in simulation of ice shelf and ice sheet evolution over long time scales. Existing calving criteria, developed for tidewater

calving glaciers, rely on empirical correlations between quantities such as water depth and front location (Meier, 1994; van der Veen, 1996) with an incomplete representation of the physical processes involved in iceberg production. Similar developments for the large, embayment filling ice shelves associated with marine ice sheets remain elusive. At present, the development of such criteria follows parameterizations developed for tidewater glaciers in that empirical relationships between longitudinal strain rates and calving rates are used (Alley et al., 2007; Bassis, 2007). This approach implicitly emphasizes vertical propagation (Fastook and Schmidt, 1982; Hughes, 1983; Reeh, 1968). The work presented here suggests a different view is warranted, at least in the case of relatively wide, embayed ice shelves such as the Ronne and Ross.

To support our framework, we must establish that horizontal, not vertical propagation governs the production of tabular icebergs. Consider the mode I fracture diagram from Chapter 2 (Figure 2.1) in two orientations (Figure 6.1). For a tidewater glacier, *fracture length* \sim *ice thickness* and longitudinal stretching favors “opening” of the fracture and vertical propagation. For a transverse ice shelf fracture, *fracture length* \gg *ice thickness* and longitudinal stretching favors lateral propagation (mixed-mode behavior is also present).

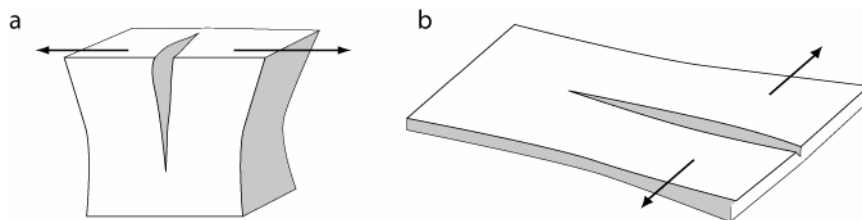


Figure 6.1 Idealization of mode I fracture propagation for (a) *fracture length* \sim *ice thickness* (cross-section, e.g. tidewater glacier) and (b) *fracture length* \gg *ice thickness* (e.g. ice shelf).

The likelihood of vertical propagation can also be evaluated by calculating stress intensity at the vertical tip of a typical fracture in the near-front environment. Following van der Veen (1998) and Scambos et al. (2000), the stress intensity for mode I opening in a dry fracture is the sum of the effect of tensile stress and the effect of the lithostatic stress, which tends to close the fracture. The first component is defined:

$$K_m^{(1)} = f(\lambda) \tau_{yy} \sqrt{\pi d} \quad [6.1]$$

in which $f(\lambda)$ is the ratio of crevasse depth d to ice thickness H and τ_{yy} is the deviatoric stress normal to the fracture plane. The lithostatic component is:

$$K_m^{(2)} = \frac{2\rho_i g}{\sqrt{\pi d}} \int_0^d \left[-b + \frac{\rho_i - \rho_s}{\rho_i C} (1 - e^{-Cb}) \right] G(\gamma, \lambda) db \quad [6.2]$$

in which ρ_i represents the ice density, ρ_s is the density of the surface snow, C is a constant taken to be 0.02 m^{-1} , and G is a numerically-derived function of λ and $\gamma = b/d$. Using the same parameter values as Scambos et al. (2000), along with geometry, ice thickness, and stresses for *fracture J0* (Figure 4.31), and a fracture depth of 50 meters (following Fricker et al., 2005), the resulting stress intensity factors in the region of *fracture J0* are negative ($\sim -16 \text{ MPa m}^{1/2}$), indicating that vertical propagation is not favorable in this region.

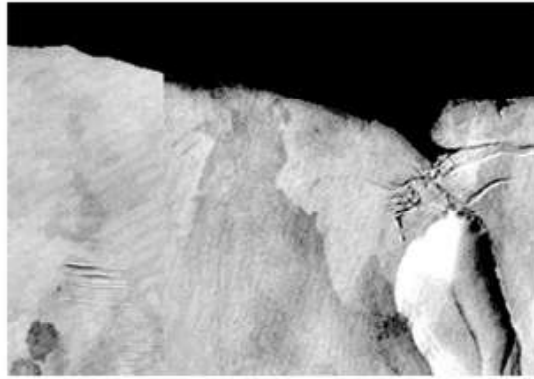
Other evidence for the importance of horizontal propagation comes from the mechanical interaction of fractures near the shelf front. As the tips of large fractures approach each other, which is observed near the shelf front (Figure 1.3), they induce

tensile stresses in the vicinity of each other's tips, enhancing propagation (Pollard and Aydin, 1988).

The large fractures we observe near the front of the Ronne Ice Shelf will at some future time play a part in iceberg calving, as such features have been observed to do in the past (Lazzara et al., 1999). Detailed documentation of fracture propagation preceding a major calving event is limited by satellite image resolution, availability, and cloud cover. One reasonably well observed event is the calving of iceberg B-15 from the eastern front of the Ross Ice Shelf in March 2000 (Figure 6.2). In that event, large fractures like the near-front fractures examined here, connected with fractures generated by shear at the corner of the ice shelf front to form the 300 km long and 40 km wide iceberg. Both the pre-existing fractures and new fractures forming at the front corner of the ice shelf were necessary (but neither alone was sufficient) to generate the massive calving event.

It is not possible, in the framework of whole-ice sheet models, to resolve the fine scale features that we find to govern fracture length but it may be possible to develop a criterion that can be used to identify a position toward which the shelf front will tend. In that such a criterion would emphasize the tendency of the front to advance or retreat toward the minimum condition for a steady geometry, it would be similar to relationships developed for tidewater glacier calving (van der Veen, 1996; Vieli et al., 2001). The basis for the criterion would be, however, distinct from those generally used for tidewater glaciers in that it would employ principles from fracture mechanics, not an empirical correlation. Such a formation should, according to the present work, follow

the far-field principal stresses in the framework of mode I and mode II propagation in the horizontal plane. The criterion may reasonably assume that large fractures will, periodically, be present near the front (depending on a spacing defined in part by their length, and thus by structural properties of the ice shelf). Those fractures are necessary but not sufficient to initiate large calving events. The second requirement is large fractures propagating from the corners of the front, driven by the relatively large shear stresses at the corners (Figure 4.29). It is the second requirement that should be used to develop a front-position criterion for ice shelves in wide embayments.



1983



1992



1996



2000

Figure 6.2 AVHRR scenes from the National Snow and Ice Data Center track development of fractures in the eastern Ross Ice Shelf that resulted in the calving of a large iceberg in March 2000. Note that the 1992 image is a composite of images with several sun illumination angles, such that more features are apparent than in a single scene.

LITERATURE CITED

- Airy, G. B., 1863, On the Strains in the Interior of Beams: Philosophical Transactions of the Royal Society of London, v. 153, p. 49-79.
- Alley, R. B., Joughin, I., Horgan, H., Dupont, T. K., Parizek, B. R., Anandakrishnan, S., and Cuffey, K. M., 2007, A calving law for ice shelves: spreading-rate control of calving rate, 2007 WAIS/FRISP Workshop.
- Aydin, A., and Johnson, A. M., 1978, Development of faults as zones of deformation bands and as slip surfaces in sandstone: Journal of Pure and Applied Geophysics, v. 116, no. 4-5, p. 931-942.
- Bassis, J. N., 2007, When iceberg calving matters: An investigation into the feedback between iceberg calving and dynamic changes in the flow of inland ice, 2007 WAIS/FRISP Workshop.
- Bassis, J. N., Coleman, R., Fricker, H. A., and Minster, J. B., 2005, Episodic propagation of a rift on the Amery Ice Shelf, East Antarctica: Geophysical Research Letters, v. 32, no. 6, p. L06502.
- Canadian Centre for Remote Sensing, 2000, The Calving of Icebergs A-43 and A-44, Ronne Ice Shelf, Antarctica, http://ccrs.nrcan.gc.ca/radar/marine/calv00_e.php.
- Cotterell, B., and Rice, J. R., 1980, Slightly curved or kinked cracks: International Journal of Fracture, v. 16, no. 2, p. 155-169.
- Crouch, S. L., and Starfield, A. M., 1983, Boundary element methods in solid mechanics: London, George Allen & Unwin, 322 p.
- Dahm, T., 2000, Numerical simulations of the propagation path and the arrest of fluid-filled fractures in the Earth: Geophysical Journal International, v. 141, no. 3, p. 623-638.
- Davis, R. O., and Selvadurai, A. P. S., 1996, Elasticity and geomechanics: Cambridge, Cambridge University Press, 201 p.
- Degraff, J. M., and Aydin, A., 1987, Surface morphology of columnar joints and its significance to mechanics and direction of joint growth: Geological Society of America Bulletin, v. 99, no. 5, p. 605-617
- Erdogan, F., and Sih, G. C., 1963, On the crack extension in plates under plane loading and transverse shear: Journal of Basic Engineering, v. 85, p. 516-27.
- Fahnestock, M. A., Scambos, T. A., Bindshadler, R. A., and Kvaran, G., 2000, A millennium of variable ice flow recorded by the Ross Ice Shelf, Antarctica: Journal of Glaciology, v. 46, no. 155, p. 632-664.
- Fastook, J. L., and Schmidt, W. F., 1982, Finite element analysis of calving from ice fronts: Annals of Glaciology, v. 3, p. 103-106.

- Ferrigno, J. G., Foley, K. M., Swithinbank, C., Williams, R. S. J., and Dailide, L. M., 2005, Coastal-Change and Glaciological Map of the Ronne Ice Shelf Area, Antarctica: 1974-2002: USGS, I-2600-D.
- Fleming, R. W., and Johnson, A. M., 1989, Structures associated with strike-slip; Faults that bound landslide elements: *Engineering Geology*, v. 27, p. 39-114.
- Fricker, H. A., Bassis, J. N., Minster, J. B., and MacAyeal, D. R., 2005, ICESat's new perspective on ice shelf rifts: The vertical dimension: *Geophysical Research Letters*, v. 32, no. 23.
- Giovinetto, M. B., and Zwally, H. J., 2000, Spatial distribution of net surface accumulation on the Antarctic ice sheet: *Annals of Glaciology*, v. 31, p. 171-178.
- Griffith, A. A., 1921, The Phenomena of Rupture and Flow in Solids: *Philosophical Transactions of the Royal Society of London*, v. A221, p. 163-198.
- Hambrey, M. J., and Müller, F., 1978, Structures and ice deformation in the White Glacier, Axel Heiberg Island, Northwest Territories, Canada: *Journal of Glaciology*, v. 20, no. 82, p. 41-66.
- Haran, T., Bohlander, J., Scambos, T. A., and Fahnestock, M., 2005, MODIS mosaic of Antarctica (MOA) image map: National Snow and Ice Data Center, Boulder, Colorado.
- Harrison, W. D., Echelmeyer, K. A., and Larsen, C. F., 1998, Measurement of temperature in a margin of the Ice Stream B, Antarctica: Implications for margin migration and lateral drag: *Journal of Glaciology*, v. 44, no. 148, p. 615-624.
- Hooke, R. L., 1998, Principles of glacier mechanics: Upper Saddle River, New Jersey, Prentice Hall, 248 p.
- Hughes, T., 1983, On the disintegration of ice shelves: the role of fracture: *Journal of Glaciology*, v. 29, no. 101, p. 98-117.
- Hughes, T. J. R., 2000, The finite element method: linear static and dynamic finite element analysis: Mineola, NY, Dover, 682 p.
- Hutter, K., 1983, Theoretical glaciology : material science of ice and the mechanics of glaciers and ice sheets: Boston Dordrecht 510 p.
- Inglis, C. E., 1913, Stresses in a plate due to the presence of cracks and sharp corners: *Transactions of the Institute of Naval Architects*, v. 55, p. 219-241.
- Ingraffea, A. R., 1987, Theory of crack initiation and propagation in rock, in Atkinson, B. K., ed., *Fracture mechanics of rock*: London, Academic Press, p. 71-110.
- Irwin, G. R., 1957, Analysis of stresses and strains near the end of a crack traversing a plate: *Journal of Applied Mechanics*, v. 24, p. 361-364.
- Jacobs, S. S., Hellmer, H., Doake, C. S. M., Jenkins, A., and Frolich, R., 1992, Melting of ice shelves and the mass balance of Antarctica: *Journal of Glaciology*, v. 38, no. 130, p. 375-387.

- Jenkins, A., and Doake, C. S. M., 1991, Ice-ocean interaction on Ronne Ice Shelf, Antarctica: *Journal of Geophysical Research*, v. 96, p. 791– 813.
- Jones, P. C., Johnson, A. C., von Frese, R. R. B., and Corr, H., 2002, Detecting rift basins in the Evans Ice Stream region of West Antarctica using airborne gravity data: *Tectonophysics*, v. 347, no. 1, p. 25-41.
- Joughin, I., and Padman, L., 2003, Melting and freezing beneath the Filchner-Ronne Ice Shelf, Antarctica: *Geophysical Research Letters*, v. 30, no. 9, p. 4.
- Kanninen, M. F., and Popelar, C. H., 1985, *Advanced Fracture Mechanics*: New York, Oxford University Press, 563 p.
- King, E. C., and Bell, A. C., 1999, Deep crustal seismic investigation of the Evans Ice Stream and Haag Nunataks, Antarctica [abs.], in *Eighth International Symposium on Antarctic Earth Sciences*, Wellington, New Zealand, July 5-9, 1999, p. 171.
- Larour, E., Rignot, E., and Aubry, D., 2004, Modelling of rift propagation on Ronne Ice Shelf, Antarctica, and sensitivity to climate change: *Geophysical Research Letters*, v. 31, no. L16404.
- Larour, E., Rignot, E., Joughin, I., and Aubry, D., 2005, Rheology of the Ronne Ice Shelf, Antarctica, inferred from satellite radar interferometry data using an inverse control method: *Geophysical research letters*, v. 32, no. 5, p. L05503.
- Lawn, B. R., and Wilshaw, T. R., 1975, *Fracture of brittle solids*: Cambridge, Cambridge University Press.
- Lazzara, M. A., Jezek, K. C., Scambos, T. A., MacAyeal, D. R., and van der Veen, C. J., 1999, On the recent calving of icebergs from the Ross Ice Shelf: *Polar Geography*, v. 23, no. 3, p. 201-212.
- Lythe, M. B., Vaughan, D. G., and Consortium, t. B., 2000, BEDMAP bed topography of the Antarctic 1:10,000,000 scale: *British Antarctic Survey (Misc) 9*.
- Meier, M. F., 1994, Columbia Glacier during rapid retreat: interactions between glacier flow and iceberg calving dynamics, in *Proceedings, Workshop on the Calving Rate of West Greenland Glaciers in Response to Climate Change*, N. Reeh (Ed.), Danish Polar Center, Copenhagen, p. 171.
- Mellor, M., 1975, A Review of Basic Snow Mechanics, *Snow Mechanics Symposium; Proceeding of the Grindelwald Symposium, Grindelwald, Bernese Oberland (Switzerland) April 1974: International Association of Hydrological Sciences Publication No. 114*, p. 251-291.
- Mercer, J. H., 1978, West Antarctic ice sheet and CO₂ greenhouse effect: a threat of disaster: *Nature*, v. 271, p. 321 - 325.
- Merry, C. J., and Whillans, I. M., 1993, Ice-flow features on Ice Stream B, Antarctica, revealed by SPOT HRV imagery: *Journal of Glaciology*, v. 39, no. 133, p. 515-527.

- Muskhelishvili, N. I., 1963, Some basic problems of the mathematical theory of elasticity; fundamental equations, plane theory of elasticity, torsion, and bending: Groningen, Holland, P. Noordhoff Ltd., 718 p.
- Nemat-Nasser, S., Oranratnachai, A., and Keer, L. M., 1979, Spacing of water-free crevasses *Journal of Geophysical Research*, v. 84, no. B9, p. 4611-4620.
- Nye, J. F., 1953, The Flow Law of Ice from Measurements in Glacier Tunnels, Laboratory Experiments and the Jungfraufirn Borehole Experiment: *Proceedings of the Royal Society of London. Series A, Mathematical and Physical Sciences*, v. 219, no. 1139, p. 477-489.
- , 1957, The Distribution of Stress and Velocity in Glaciers and Ice-Sheets: *Proceedings of the Royal Society of London. Series A, Mathematical and Physical Sciences*, v. 239, no. 1216, p. 113-133.
- Olson, J., and Pollard, D. D., 1989, Inferring paleostresses from natural fracture patterns: A new method: *Geology*, v. 17, no. 4, p. 345-348.
- Palmer, A. C., and Rice, J. R., 1973, The growth of slip surfaces in the progressive failure of over-consolidated clay: *Proceedings of the Royal Society of London. Series A, Mathematical and Physical Sciences*, v. 332, no. 1591, p. 527-548.
- Paris, P. C., and Sih, G. C., 1965, Stress analysis of cracks, in *Fracture Toughness Testing and Its Applications: ASTM Special Technical Publication*, v. 381, p. 30-76.
- Paterson, W. S. B., 1994, *The physics of glaciers: Woburn, Butterworth Heinemann.*
- Pollard, D. D., and Aydin, A., 1988, Progress in understanding jointing over the past century: *GSA Bulletin*, v. 100, no. 8, p. 1181 - 1204.
- Pollard, D. D., and Segall, P., 1987, Theoretical displacements and stresses near fractures in rock: with applications to faults, joints, veins, dikes, and solution surfaces, in Atkinson, B. K., ed., *Fracture mechanics of rocks: London, Harcourt Brace Jovanovich*, p. 277-349.
- Reeh, N., 1968, On the calving of ice from floating glaciers and ice shelves: *Journal of Glaciology*, v. 7, no. 50, p. 215-232.
- Rignot, E., 2001, Evidence for rapid retreat and mass loss of Thwaites Glacier, West Antarctica: *Journal of Glaciology*, v. 47, no. 157, p. 213-222.
- Rist, M. A., Sammonds, P. R., Murrell, S. A. F., Meredith, P. G., Doake, C. S. M., Oereter, H., and Matsuki, K., 1999, Experimental and theoretical fracture mechanics applied to Antarctic ice fracture and surface crevassing: *Journal of Geophysical Research*, v. 104, no. B2, p. 2973-2987.
- Rist, M. A., Sammonds, P. R., Oereter, H., and Doake, C. S. M., 2002, Fracture of Antarctic shelf ice: *Journal of Geophysical Research*, v. 107, no. 0.
- Sandhager, H., Vaughan, D. G., and Lambrecht, A., 2004, Meteoric, marine, and total ice thickness maps of Filchner-Ronne-Schelfeis, Antarctica, FRISP Report No. 15:

- Bremerhaven, Germany, Alfred-Wegener Inst. für Polar und Meeresforsch., p. 22-30.
- Scambos, T. A., Hulbe, C., Fahnestock, M., and Bohlander, J., 2000, The link between climate warming and break-up of ice shelves in the Antarctic Peninsula: *Journal of Glaciology*, v. 46, no. 154, p. 516-530.
- Sempere, J. C., and Macdonald, K. C., 1986, Overlapping spreading centers: implications from crack growth simulation by the displacement discontinuity method: *Tectonics*, v. 5, no. 1, p. 151-163.
- Sih, G. C., 1966, On the Westergaard method of crack analysis: *International Journal of Fracture*, v. 2, no. 4, p. 628-631.
- , 1973, *Handbook of stress-intensity factors: Stress-intensity factor solutions and formulas for reference*: Bethlehem, Lehigh University, 815 p.
- Smith, R. A., 1976, The application of fracture mechanics to the problem of crevasse penetration: *Journal of Glaciology*, v. 17, p. 223-228.
- Stephenson, S. N., 1984, Glacier flexure and the position of grounding lines: measurements by tiltmeter on Rutford Ice Stream, Antarctica: *Annals of Glaciology*, v. 5, p. 165-169.
- Tada, H., Paris, P. C., and Irwin, G. R., 2000, *The stress analysis of cracks handbook*: New York, ASME Press: Professional Engineering Publication: ASM International, 677 p.
- Thomas, A. L., 1991, FRAC2D, Stanford University.
- Thomas, R. H., Sanderson, T. J. O., and Rose, K. E., 1979, Effect of climatic warming on the West Antarctic ice sheet: *Nature*, v. 277, p. 355 - 358.
- Timoshenko, S., and Goodier, J. N., 1969, *Theory of elasticity*, Engineering societies monographs: New York, McGraw-Hill, 567 p.
- van der Veen, C. J., 1996, Tidewater calving: *Journal of Glaciology*, v. 42, no. 141, p. 375-385.
- , 1998, Fracture mechanics approach to penetration of surface crevasses on glaciers: *Cold Regions Science and Technology*, v. 27, p. 31-47.
- Vaughan, D. G., 1995, Tidal flexure at ice shelf margins: *Journal of Geophysical Research*, v. 100, no. B4, p. 6213-6224.
- Vieli, A., Funk, M., and Blatter, H., 2001, Flow dynamics of tidewater glaciers: a numerical modelling approach *Journal of Glaciology*, v. 47, no. 159, p. 595-606.
- Weertman, J., 1973, Can a water-filled crevasse reach the bottom surface of a glacier, in *Proceedings of Symposium on the Hydrology of Glaciers*, September 7-13, 1969, Cambridge, England, p. 139-145.
- Westergaard, H. M., 1939, Bearing pressures and cracks: *Transactions of the American Society of Mechanical Engineers*, v. 61, p. A49-A53.

APPENDIX

A Root-Mean Square Errors

Table A.1 Root-mean square errors for calibration of Experiment 1. Unless noted, remote stresses are $M_{xx} = 1.2$ MPa, $M_{yy} = 1.9$ MPa, and $M_{xy} = -0.1$ MPa, and the scaling factor $\mathfrak{S} = 0.8$.

Poisson's Ratio	Elasticity Modulus, MPa	Root-Mean Square Error	Comments
0.27	6500	375.40	
0.27	7000	129.17	
0.27	7400	164.28	
0.27	7500	78.05	
0.27	7600	231.61	
0.27	8000	1865.18	
0.28	7000	314.91	
0.28	7500	734.92	
0.28	8000	334.38	
0.29	8000	427.45	
0.29	9000	419.18	

Table A.2 Root-mean square errors for calibration of Experiment 2 simple boundary. Unless noted, remote stresses are $M_{xx} = 0.9$ MPa, $M_{yy} = 1.8$ MPa, and $M_{xy} = -0.3$ MPa, and the scaling factor $\mathfrak{S} = 0.8$.

Poisson's Ratio	Elasticity Modulus, MPa	Root-Mean Square Error	Comments
0.27	7500	117.18	
0.27	8000	198.90	
0.28	7500	418.05	
0.28	8000	185.24	
0.28	8500	227.21	
0.29	8000	85.34	
0.29	8000	278.34	3km step size along boundary instead of 2km
0.29	8500	128.38	

Table A.3 Root-mean square errors for calibration of Experiment 2 extended boundary. Unless noted, remote stresses are $M_{xx} = 0.9$ MPa, $M_{yy} = 1.8$ MPa, and $M_{xy} = -0.3$ MPa, and the scaling factor $\zeta = 0.8$. This boundary was not used in the propagation simulation.

Poisson's Ratio	Elasticity Modulus, MPa	Root-Mean Square Error	Comments
0.27	7500	166.25	
0.27	8000	170.16	
0.28	7500	372.08	
0.28	8000	358.22	
0.29	7500	234.94	
0.29	8000	641.08	
0.29	8000	201.31	changed remote stress
			3km step size along boundary
0.29	8000	200.23	instead of 2km

Table A.4 Root-mean square errors for calibration of Experiment 3 simple boundary. Unless noted, remote stresses are $M_{xx} = 0.9$ MPa, $M_{yy} = 1.8$ MPa, and $M_{xy} = -0.3$ MPa, and the scaling factor $\zeta = 0.8$.

Poisson's Ratio	Elasticity Modulus, MPa	Root-Mean Square Error	Comments
0.25	10000	164.86	
0.26	8000	142.08	
0.27	7500	85.97	
0.27	8000	69.46	
0.28	7500	246.58	
0.28	8000	48.66	
0.28	8000	64.65	0.9
0.28	8000	91.42	1
0.28	8000	137.08	0.9, no remote stresses
0.28	8500	168.41	
0.28	9000	57.44	
0.28	10000	1397.33	
0.29	8000	188.06	
0.29	8500	121.46	
0.3	8000	176.98	
0.3	9000	106.53	
0.3	10000	605.54	
0.33	10000	306.70	

Table A.5 Root-mean square errors for calibration of Experiment 3 extended boundary. Unless noted, remote stresses are $M_{xx} = 0.9$ MPa, $M_{yy} = 1.8$ MPa, and $M_{xy} = -0.3$ MPa, and the scaling factor $\mathfrak{S} = 0.8$.

Poisson's Ratio	Elasticity Modulus, MPa	Root-Mean Square Error	Comments
0.27	7500	146.39	
0.27	8000	66.12	
0.27	8000	47.43	0.9
0.28	7500	232.53	
0.28	8000	80.01	
0.29	7500	113.96	
0.29	7500	87.89	0.9, remote stress, 1 -0.35 1.9
0.29	7500	113.96	
0.29	8000	157.41	

Table A.6 Root-mean square errors for calibration of Experiment 4 upstream boundary. Unless noted, remote stresses are $M_{xx} = 0.9$ MPa, $M_{yy} = 1.8$ MPa, and $M_{xy} = -0.3$ MPa, and the scaling factor $\mathfrak{S} = 0.8$. Model setup in bold is used for propagation simulation.

Poisson's Ratio	Elasticity Modulus, MPa	Root-Mean Square Error	Comments
0.25	7500	111.51	0.85
0.26	7500	113.02	0.85
0.27	7000	114.82	0.85
0.27	7500	114.98	0.8
0.27	7500	113.43	0.9
0.27	7500	110.91	0.85
0.27	8000	115.83	0.8
0.28	8000	115.94	0.8
0.28	8500	114.99	0.8

Table A.7 Root-mean square errors for calibration of Experiment 4 downstream boundary. Unless noted, remote stresses are $M_{xx} = 0.9$ MPa, $M_{yy} = 1.8$ MPa, and $M_{xy} = -0.3$ MPa, and the scaling factor $\mathfrak{S} = 0.8$. This boundary was not used in the propagation simulation.

Poisson's Ratio	Elasticity Modulus, MPa	Root-Mean Square Error	Comments	in text
0.26	9000	216.73		0.85
0.27	7500	217.82		0.85
0.27	8000	222.34		0.85
0.28	8000	215.49		0.85
0.28	8000	210.79		0.8
0.28	8000	212.11	added fxM5 and fxM6 as boundaries	0.8
0.28	8000	212.97	added only fxM5 as boundary	0.8
0.29	7500	218.31		0.85

Table A.8 Root-mean square errors for calibration of Experiment 4 downstream extended boundary. Unless noted, remote stresses are $M_{xx} = 0.9$ MPa, $M_{yy} = 1.8$ MPa, and $M_{xy} = -0.3$ MPa, and the scaling factor $\zeta = 0.8$. This boundary not used in propagation simulation.

Poisson's Ratio	Elasticity Modulus, MPa	Root-Mean Square Error	Comments	factor
0.26	7500	38181.89	remote stress, 0.85 -0.35 1.9	0.85
0.26	8000	1543.14	remote stress, 0.85 -0.35 1.9	0.85
0.26	9000	1404.20	remote stress, 0.85 -0.35 1.9	0.85
0.26	9000	1402.41	remote stress, 0.9 -0.3 1.8	0.85
0.26	10000	2727.47	remote stress, 0.85 -0.35 1.9	0.85
0.27	7500	8368.00	remote stress, 0.85 -0.35 1.9	0.85
0.27	8000	6212.48	remote stress, 0.85 -0.35 1.9	0.85
0.27	10000	2337.57	remote stress, 0.85 -0.35 1.9	0.85
0.26	9000	1325.07	remote stress, 0.9 -0.3 1.8. added fx M5 and M6, not active	0.8

Table A.9 Root-mean square errors for calibration of Experiment 5 boundary. Unless noted, remote stresses are $M_{xx} = 0.9$ MPa, $M_{yy} = 1.6$ MPa, and $M_{xy} = -0.1$ MPa, and the scaling factor $\zeta = 0.8$.

Poisson's Ratio	Elasticity Modulus, MPa	Root-Mean Square Error	Comments
0.27	7000	135.40	
0.27	7000	178.53	0.9
0.27	7500	122.13	
0.27	7500	164.50	0.9
0.27	8000	138.42	
0.27	8000	199.33	
0.28	8000	2997.91	
0.27	7500	191.17	added J0

B Stress Intensity Factors

Table B.1 Stress intensity factors for Experiment 1: *Test fracture k1*, fracture scaling factor $\mathfrak{S} = 0.8$. The fracture toughness K_{IC} was $0.1 \text{ MPa m}^{1/2}$. The iteration number designates distinct model runs within a single test. The first iteration uses boundary stresses defined for the test, based on the model calibration and relevant scaling factors for domain and fracture boundaries. Each subsequent iteration uses the boundary stresses and computed during the previous iteration and any incremental growth in fracture geometry. K1 and K2 represent the stress intensity factors computed at the tip for propagation modes I and II, respectively. Angle θ_0 is the predicted angle of propagation for mixed-mode loading, in degrees. The mixed-mode failure criterion is based on the $\sigma(\theta)_{\max}$ theory (Erdogan and Sih, 1963). If the value listed as Failure exceeds 1, propagation occurs.

Iteration Number	Right tip				Left tip			
	K1	K2	Angle θ_0	Failure	K1	K2	Angle θ_0	Failure
1	-0.361	0.000	0.00	-3.61	-0.155	0.000	0.00	-1.55

Table B.2 Stress intensity factors for Experiment 1: *Test fracture k1*, fracture scaling factor $\mathfrak{S} = 0.75$. The fracture toughness K_{IC} was $0.3 \text{ MPa m}^{1/2}$. Refer to Table B.1 for description of headings.

Iteration Number	Right tip				Left tip			
	K1	K2	Angle θ_0	Failure	K1	K2	Angle θ_0	Failure
1	0.361	0.000	0.00	1.20	0.465	0.414	-51.26	2.59
2	0.361	0.000	0.00	1.20	0.827	-0.827	53.13	4.93
3	0.722	0.000	0.00	2.41	0.724	0.414	-43.01	3.26
4	0.722	0.000	0.00	2.41	1.241	-0.414	31.37	4.73
5	0.722	0.000	0.00	2.41	1.345	0.414	-29.64	5.04
6	1.083	0.000	0.00	3.61	1.655	-0.414	25.33	5.99
7	1.083	0.000	0.00	3.61	1.862	0.414	-23.04	6.63
8	1.083	0.000	0.00	3.61	2.482	-0.414	17.99	8.60
9	1.443	0.000	0.00	4.81	2.689	0.000	0.00	8.96
10	2.165	0.000	0.00	7.22	3.103	0.414	-14.69	10.61
11					3.724	-0.827	23.04	13.26
12					3.930	0.827	-22.02	13.91

Table B.3 Stress intensity factors for Experiment 2: *Test fracture j3* and *g6*, $\mathfrak{S} = 0.8$. The fracture toughness K_{IC} was $0.1 \text{ MPa m}^{1/2}$.

Iteration Number	Test fracture j3				Test fracture g6			
	K1	K2	Angle θ_0	Failure	K1	K2	Angle θ_0	Failure
1	0.00	0.351	undef	undef	0.00	0.311	undef	undef

Table B.4 Stress intensity factors for Experiment 2: *Test fracture j3* and *g6*, $\mathfrak{S} = 0.75$. The fracture toughness K_{IC} was $0.3 \text{ MPa m}^{1/2}$.

Iteration Number	Test fracture j3				Test fracture g6			
	K1	K2	Angle θ_0	Failure	K1	K2	Angle θ_0	Failure
1	0.351	0.351	-53.13	2.09	0.000	0.311	0.00	0.00
2	-0.701	-0.438	-44.82	-3.27	0.000	0.311	0.00	0.00

Table B.5 Stress intensity factors for Experiment 2: *Test fracture j3* and *g6*, $\mathfrak{S} = 0.7$. The fracture toughness K_{IC} was $0.3 \text{ MPa m}^{1/2}$.

Iteration Number	Test fracture j3				Test fracture g6			
	K1	K2	Angle θ_0	Failure	K1	K2	Angle θ_0	Failure
1	0.701	0.000	0.00	2.34	0.00	0.00	0.00	0.00
2	0.701	0.000	0.00	2.34	0.00	0.00	0.00	0.00
3	0.701	0.000	0.00	2.34	0.00	0.00	0.00	0.00
4	0.701	0.000	0.00	2.34	0.00	0.00	0.00	0.00
5	0.701	0.000	0.00	2.34	0.00	0.00	0.00	0.00
6	0.701	-0.351	40.21	3.00	0.00	0.00	0.00	0.00
7	0.570	1.052	-60.62	5.18	0.00	0.00	0.00	0.00
8	0.701	-0.526	48.30	3.57	0.00	0.00	0.00	0.00
9	0.438	0.701	-59.19	3.58	0.00	0.00	0.00	0.00

Table B.6 Stress intensity factors for Experiment 3: *Test fracture s6*, $\mathfrak{S} = 0.8$. The fracture toughness K_{IC} was $0.1 \text{ MPa m}^{1/2}$.

Iteration Number	Right tip				Left tip			
	K1	K2	Angle θ_0	Failure	K1	K2	Angle θ_0	Failure
1	-0.503	0.251	40.21	-6.45	-0.443	0.354	49.46	-6.99

Table B.7 Stress intensity factors for Experiment 3: *Test fracture s6*, $\mathfrak{S} = 0.75$. The fracture toughness K_{IC} was $0.15 \text{ MPa m}^{1/2}$.

Iteration Number	Right tip				Left tip			
	K1	K2	Angle θ_0	Failure	K1	K2	Angle θ_0	Failure
1	0.063	0.000	0.00	0.42	0.177	0.000	0.00	1.18
2	0.063	0.000	0.00	0.42	0.177	0.000	0.00	1.18
3	0.126	0.000	0.00	0.84	0.177	0.000	0.00	1.18
4	0.126	0.000	0.00	0.84	0.177	0.000	0.00	1.18
5	0.126	0.000	0.00	0.84	0.266	0.000	0.00	1.77
6	0.126	0.000	0.00	0.84	0.266	0.000	0.00	1.77
7	0.126	0.126	-53.13	1.50	0.266	0.000	0.00	1.77
8	-0.754	-0.188	-25.33	-5.45	0.266	0.000	0.00	1.77
9	-0.754	-0.188	-25.33	-5.45	0.266	0.000	0.00	1.77
10	-0.754	-0.188	-25.33	-5.45	0.354	0.000	0.00	2.36
11	-0.754	-0.188	-25.33	-5.45	0.354	0.000	0.00	2.36
12	-0.754	-0.220	-28.51	-5.59	0.354	0.000	0.00	2.36
13	-0.503	-0.220	-37.32	-4.11	0.443	0.000	0.00	2.95
14	-0.503	-0.220	-37.32	-4.11	0.443	0.000	0.00	2.95
15	-0.503	-0.220	-37.32	-4.11	0.531	0.000	0.00	3.54

Table B.8 Stress intensity factors for Experiment 3: *Test fracture s6*, $\mathfrak{S} = 0.75$. The fracture toughness K_{IC} was $0.3 \text{ MPa m}^{1/2}$.

Iteration Number	Right tip				Left tip			
	K1	K2	Angle θ_0	Failure	K1	K2	Angle θ_0	Failure
1	0.063	0.000	0.00	0.21	0.177	0.000	0.00	0.59

Table B.9 Stress intensity factors for Experiment 3 extended-boundary: *Test fracture s4*, $\mathfrak{S} = 0.8$. The fracture toughness K_{IC} was $0.3 \text{ MPa m}^{1/2}$.

Iteration Number	Right tip				Left tip			
	K1	K2	Angle θ_0	Failure	K1	K2	Angle θ_0	Failure
1	0.245	-0.245	53.13	1.46	0.575	-0.288	40.21	2.46
2	-0.184	0.980	66.99	-4.12	0.252	0.575	-62.44	2.70
3	-0.184	0.980	66.99	-4.12	0.575	-0.288	40.21	2.46
4	-0.122	0.980	68.16	-4.00	0.575	0.575	-53.13	3.43
5	-0.122	0.980	68.16	-4.00	0.000	-0.431	0.00	0.00

Table B.10 Stress intensity factors for Experiment 3 extended-boundary: *Test fracture s4*, $\mathfrak{S} = 0.75$. The fracture toughness K_{IC} was $0.3 \text{ MPa m}^{1/2}$.

Iteration Number	Right tip				Left tip			
	K1	K2	angle	failure	K1	K2	angle	failure
1	0.490	-0.245	40.21	2.09	0.575	-0.288	40.21	2.46
2	0.310	0.980	-64.62	4.36	0.476	0.575	-55.83	3.20
3	0.000	-0.367	0.00	0.00	0.575	-0.288	40.21	2.46
4	0.000	-0.367	0.00	0.00	0.719	0.575	-49.46	3.78
5	0.000	-0.367	0.00	0.00	0.575	-0.431	48.30	2.93
6	0.490	-0.367	48.30	2.49	0.863	0.575	-46.09	4.15
7	0.612	0.490	-49.46	3.22	0.575	-0.575	53.13	3.43
8	0.000	-0.612	0.00	0.00	0.935	0.575	-44.51	4.34
9	0.000	-0.612	0.00	0.00	0.863	-0.288	31.37	3.29
10	0.000	-0.612	0.00	0.00	1.150	0.575	-40.21	4.92
11	0.490	-0.612	56.28	3.37	1.150	-0.575	40.21	4.92
12	0.857	0.490	-43.01	3.86	1.438	0.000	0.00	4.79
13	0.490	-0.490	53.13	2.92	1.438	0.575	-35.36	5.73
14	0.764	0.490	-45.32	3.61	1.438	-0.575	35.36	5.73
15	0.980	-0.245	25.33	3.54	1.725	0.575	-31.37	6.57
16	1.102	0.490	-37.66	4.53	1.725	-0.575	31.37	6.57
17	0.735	-0.735	53.13	4.38	2.013	0.575	-28.07	7.44
18	1.072	0.490	-38.28	4.45	2.013	-0.575	28.07	7.44
19	0.980	-0.245	25.33	3.54	2.444	0.575	-24.14	8.77
20	1.225	0.490	-35.36	4.88	2.588	-0.288	12.38	8.78

Table B.11 Stress intensity factors for Experiment 3 extended-boundary: *Test fracture z2*, $\mathfrak{S} = 0.85$. The fracture toughness K_{IC} was $0.3 \text{ MPa m}^{1/2}$.

Iteration Number	Right tip				Left tip			
	K1	K2	Angle θ_0	Failure	K1	K2	Angle θ_0	Failure
1	-0.255	-0.509	-61.34	-2.46	0.288	-0.288	53.13	1.71
2	-0.255	-0.509	-61.34	-2.46	-0.072	0.575	68.16	-2.35

Table B.12 Stress intensity factors for Experiment 3 extended-boundary: *Test fracture z2*, $\mathfrak{S} = 0.8$. The fracture toughness K_{IC} was $0.3 \text{ MPa m}^{1/2}$.

Iteration Number	Right tip				Left tip			
	K1	K2	Angle θ_0	Failure	K1	K2	Angle θ_0	Failure
1	0.000	-0.509	0.00	0.00	0.575	-0.288	40.21	2.46
2	0.000	-0.509	0.00	0.00	0.485	0.575	-55.58	3.22
3	0.000	-0.509	0.00	0.00	0.575	-0.288	40.21	2.46
4	0.000	-0.509	0.00	0.00	0.719	0.575	-49.46	3.78
5	0.255	-0.509	61.34	2.46	0.575	-0.431	48.30	2.93
6	-0.255	0.509	61.34	-2.46	0.719	0.575	-49.46	3.78
7	-0.255	0.509	61.34	-2.46	0.575	-0.575	53.13	3.43
8	-0.255	0.509	61.34	-2.46	0.863	0.575	-46.09	4.15
9	-0.255	0.509	61.34	-2.46	0.575	-0.575	53.13	3.43
10	-0.255	0.509	61.34	-2.46	0.791	0.575	-47.74	3.96
11	-0.255	0.764	64.31	-3.43	0.863	-0.288	31.37	3.29
12	-0.255	0.764	64.31	-3.43	1.006	0.575	-43.01	4.53
13	-0.255	0.764	64.31	-3.43	0.575	-0.575	53.13	3.43
14	0.000	0.764	0.00	0.00	1.150	0.575	-40.21	4.92
15	0.000	0.764	0.00	0.00	1.150	-0.288	25.33	4.16
16	0.000	0.764	0.00	0.00	1.438	0.288	-21.09	5.06
17	0.000	0.764	0.00	0.00	1.438	-0.288	21.09	5.06
18	0.000	0.764	0.00	0.00	1.438	0.288	-21.09	5.06
19	0.000	0.764	0.00	0.00	1.725	-0.288	17.99	5.98
20	0.000	1.018	0.00	0.00	1.725	0.288	-17.99	5.98

Table B.13 Stress intensity factors for Experiment 4: *Test fracture N1*, $\mathfrak{S} = 0.8$. The fracture toughness K_{IC} was $0.3 \text{ MPa m}^{1/2}$.

Iteration Number	Right tip				Left tip			
	K1	K2	Angle θ_0	Failure	K1	K2	Angle θ_0	Failure
1	-0.003	1.027	70.48	-3.96	0.278	0.907	-64.79	4.02
2	-0.004	1.001	70.45	-3.86	-0.307	-0.473	-58.79	-2.44

Table B.14 Stress intensity factors for Experiment 4: *Test fracture NI*, $\mathfrak{S} = 0.75$. The fracture toughness K_{IC} was $0.3 \text{ MPa m}^{1/2}$.

Iteration Number	Right tip				Left tip			
	K1	K2	angle	failure	K1	K2	angle	failure
1	0.617	0.878	-57.88	4.63	0.350	1.001	-64.02	4.53
2	0.037	-0.640	69.42	2.53	-0.301	-0.565	-60.77	-2.77
3	0.548	0.341	-44.76	2.56	-0.275	-0.582	-61.82	-2.78
4	0.354	-0.531	58.49	2.76	-0.264	-0.600	-62.40	-2.82
5	0.324	0.706	-62.06	3.35	-0.235	-0.611	-63.38	-2.81
6	0.307	-0.485	59.05	2.48	-0.221	-0.623	-63.92	-2.82
7	0.422	0.608	-58.03	3.20	-0.195	-0.637	-64.80	-2.82
8	0.294	-0.542	60.61	2.67	-0.184	-0.651	-65.25	-2.86
9	0.448	0.608	-57.33	3.25	-0.161	-0.666	-65.99	-2.87
10	0.374	-0.525	57.71	2.78	-0.143	-0.680	-66.56	-2.89
11	0.516	0.628	-55.93	3.48	-0.118	-0.694	-67.33	-2.89
12	0.472	-0.539	55.08	3.06	-0.098	-0.709	-67.92	-2.91
13	0.648	0.643	-52.99	3.85	-0.072	-0.729	-68.66	-2.94
14	0.625	-0.582	52.03	3.57	-0.043	-0.746	-69.43	-2.95
15	0.843	0.674	-49.45	4.43	-0.011	-0.766	-70.24	-2.97
16	0.860	-0.643	48.24	4.37	0.026	-0.786	69.90	3.07
17	1.165	0.734	-45.00	5.46	0.823	0.232	-27.82	3.04
18	1.278	-0.723	42.80	5.73	0.776	-0.364	38.85	3.25
19	1.641	0.795	-39.52	6.94	0.634	0.843	-57.07	4.54
20	1.813	-0.792	37.28	7.41	0.481	-0.680	57.81	3.59
21	2.209	0.864	-34.85	8.75	0.691	0.709	-53.50	4.18
22	2.461	-0.838	31.82	9.42	0.552	-0.691	56.30	3.80
23	2.846	0.947	-31.32	10.84	0.674	0.792	-55.45	4.45
24	3.202	-0.800	25.33	11.59	0.587	-0.683	55.33	3.85
25	3.489	1.268	-33.26	13.56	0.651	0.803	-56.11	4.43

Table B.15 Stress intensity factors for Experiment 5: *Test fracture J5*, $\mathfrak{S} = 0.8$. The fracture toughness K_{IC} was $0.3 \text{ MPa m}^{1/2}$.

Iteration Number	Right tip				Left tip			
	K1	K2	angle	failure	K1	K2	angle	failure
1	0.704	-0.176	25.33	2.55	1.413	-0.442	29.97	5.31
2	0.704	0.308	-37.32	2.88	1.060	0.442	-36.25	4.27
3	0.704	-0.352	40.21	3.01	1.413	-0.353	25.33	5.11
4	0.704	0.352	-40.21	3.01	1.060	0.364	-32.04	4.07
5	0.704	-0.352	40.21	3.01	1.413	-0.530	33.94	5.54
6	0.704	0.352	-40.21	3.01	1.413	0.472	-31.41	5.39
7	0.704	-0.176	25.33	2.55	1.590	-0.353	23.04	5.66
8	0.704	0.044	-7.10	2.36	1.413	0.309	-22.74	5.03
9	0.704	0.000	0.00	2.35	1.767	-0.353	21.09	6.22
10	0.704	0.088	-13.84	2.40	1.767	0.309	-18.79	6.15
11	0.704	-0.176	25.33	2.55	1.944	-0.353	19.43	6.78
12	0.352	0.237	-46.24	1.70	2.120	0.353	-17.99	7.35
13	0.528	-0.176	31.37	2.01	2.120	-0.353	17.99	7.35
14	0.704	0.440	-44.82	3.29	2.120	0.398	-19.95	7.42
15	1.233	-0.352	28.07	4.56	2.474	-0.353	15.65	8.49
16	1.761	0.352	-21.09	6.20	2.474	0.265	-11.96	8.38
17	2.817	-0.176	7.10	9.45	2.827	-0.177	7.10	9.48
18					2.827	0.353	-13.84	9.64
19					3.004	-0.353	13.07	10.22
20					2.827	0.265	-10.53	9.55
21					3.180	-0.353	12.38	10.79
22					3.180	0.265	-9.40	10.71
23					3.357	-0.177	5.99	11.24
24					3.534	0.088	-2.86	11.79
25					3.534	-0.088	2.86	11.79
26					3.534	0.088	-2.86	11.79
27					3.710	-0.088	2.72	12.38
28					3.887	0.088	-2.60	12.97
29					3.887	-0.088	2.60	12.97
30					3.887	0.088	-2.60	12.97
31					4.240	-0.088	2.38	14.14
32					4.240	0.088	-2.38	14.14
33					4.417	-0.088	2.29	14.73
34					4.594	0.088	-2.20	15.32
35					4.594	0.000	0.00	15.31
36					4.770	0.000	0.00	15.90
37					4.947	0.000	0.00	16.49
38					5.124	0.000	0.00	17.08
39					5.124	0.000	0.00	17.08
40					5.300	0.000	0.00	17.67
41					5.477	0.000	0.00	18.26
42					5.654	0.088	-1.79	18.85
43					5.830	0.000	0.00	19.44
44					6.007	0.000	0.00	20.02
45					6.184	0.000	0.00	20.61
46					6.360	0.000	0.00	21.20
47					6.537	0.000	0.00	21.79
48					6.714	0.000	0.00	22.38

Table B.16 Stress intensity factors for Experiment 5: *Test fractures J7 and A4*, $\mathfrak{S} = 0.8$. The fracture toughness K_{IC} was $0.3 \text{ MPa m}^{1/2}$.

Iteration Number	fxJ7				fxJ7				fxA4			
	Right tip K1	Right tip K2	angle	failure	Left tip K1	Left tip K2	angle	failure	Right tip K1	Right tip K2	angle	failure
1	0.979	-0.612	44.82	4.57	1.072	-0.357	31.37	4.08	0.300	0.150	-40.21	1.28
2	0.979	0.245	-25.33	3.54	0.715	0.536	-48.30	3.64	-0.075	-0.900	-68.95	-3.60
3	0.979	0.031	-3.57	3.27	1.072	-0.536	40.21	4.58	-0.075	-0.900	-68.95	-3.60
4	0.979	0.031	-3.57	3.27	0.715	0.447	-44.82	3.34	-0.075	-0.900	-68.95	-3.60
5	0.979	0.000	0.00	3.26	1.072	-0.536	40.21	4.58	-0.075	-0.900	-68.95	-3.60
6	0.979	0.000	0.00	3.26	1.072	0.357	-31.37	4.08	-0.075	-0.900	-68.95	-3.60
7	0.979	0.000	0.00	3.26	1.072	-0.357	31.37	4.08	-0.075	-0.900	-68.95	-3.60
8	0.979	0.000	0.00	3.26	1.072	0.424	-35.13	4.26	-0.075	-0.900	-68.95	-3.60
9	0.979	0.000	0.00	3.26	1.072	-0.357	31.37	4.08	-0.075	-0.900	-68.95	-3.60
10	0.979	0.000	0.00	3.26	1.072	0.402	-33.94	4.20	-0.075	-0.900	-68.95	-3.60
11	0.979	0.000	0.00	3.26	1.251	-0.536	36.87	5.09	-0.075	-0.900	-68.95	-3.60
12	0.979	0.000	0.00	3.26	1.072	0.447	-36.25	4.32	-0.075	-0.900	-68.95	-3.60
13	0.979	-0.061	7.10	3.28	1.251	-0.536	36.87	5.09	-0.075	-0.900	-68.95	-3.60
14	0.979	0.084	-9.68	3.30	1.072	0.491	-38.33	4.45	-0.075	-0.900	-68.95	-3.60
15	0.979	0.000	0.00	3.26	1.251	-0.536	36.87	5.09	-0.075	-0.900	-68.95	-3.60
16	0.979	0.000	0.00	3.26	1.072	0.491	-38.33	4.45	0.000	-0.600	0.00	0.00
17	0.490	0.000	0.00	1.63	1.251	-0.536	36.87	5.09	0.000	-0.600	0.00	0.00
18	0.979	-0.061	7.10	3.28	1.072	0.469	-37.32	4.39	0.000	-0.600	0.00	0.00
19	0.490	0.031	-7.10	1.64	1.430	-0.536	33.94	5.60	0.000	-0.600	0.00	0.00
20	0.490	0.000	0.00	1.63	1.430	0.447	-29.97	5.37	0.075	-0.600	68.16	2.45
21	0.490	0.122	-25.33	1.77	1.430	-0.357	25.33	5.17	0.000	0.450	0.00	0.00
22	0.490	0.000	0.00	1.63	1.430	0.357	-25.33	5.17	0.000	0.487	0.00	0.00
23	0.245	0.000	0.00	0.82	1.608	-0.357	23.04	5.73	0.000	0.525	0.00	0.00
24	0.490	0.000	0.00	1.63	1.430	0.357	-25.33	5.17	0.300	0.544	-60.44	2.69
25	0.490	0.245	-40.21	2.09	1.787	-0.536	29.10	6.66	0.675	-0.600	51.26	3.76
26	0.490	-0.490	53.13	2.92	2.144	0.715	-31.37	8.17	1.200	0.825	-46.68	5.85
27	0.490	0.367	-48.30	2.49	2.680	-0.893	31.37	10.21	1.500	-1.350	51.46	8.41
28	0.979	-0.490	40.21	4.19	3.216	0.223	-7.87	10.80	2.399	0.112	-5.34	8.02
29	1.224	0.245	-21.09	4.31	3.216	-0.179	6.32	10.77	2.099	-0.150	8.09	7.05
30	1.714	0.000	0.00	5.71	2.859	0.357	-13.84	9.75	1.200	0.412	-32.04	4.60
31	1.959	0.000	0.00	6.53	2.859	-0.179	7.10	9.59	0.900	-0.450	40.21	3.85
32	2.449	-0.245	11.20	8.28	3.216	0.179	-6.32	10.77	-0.300	0.768	63.29	-3.54
33	2.938	0.490	-17.99	10.19	3.216	0.179	11.77	11.50	-0.600	0.750	56.28	-4.12
34	3.673	0.000	0.00	12.24	3.395	-0.357	11.77	11.50	-0.900	0.740	49.95	-4.80
35	5.877	0.000	0.00	19.59	3.395	-0.357	11.77	11.50	-0.900	0.792	51.10	-4.98
36									-0.600	0.694	55.24	-3.91

C MATLAB Scripts

C.1 preview_data.m

SCRIPT: preview_boundary.m

REQUIRES functions:
fget_corner.m
find_index.m

This script displays the boundary determined by corner coordinates associated with the input test name. Principal stresses, fractures, and relevant ice shelf features are displayed. The input file adj_stresses.mat contains only the full stresses required for the study area.

Sample run with user input

```
-- BEGIN SETUP --  
Enter test name: Test5b  
Use filter 15x15 (15), no smoothing (0), or 20x20 (20)? 20  
  
Loading ice shelf stresses...  
Plot principal stresses (1), mean stresses (2), effective strain rate  
(3), or thickness (4): 1  
Enter figure number: 100  
Enter skip amount: 4  
Modify principal stresses (y/n)? : n  
Plotting principal stresses...
```

C.2 get_export.m

SCRIPT: get_export.m

REQUIRES functions:
fget_corner.m
find_index.m
fget_obs.m

This script requires user input to setup variables needed for Frac2D code. The variables are setup so that each can be copied from the MATLAB array editor and pasted into the appropriate location in the Frac2D input file using a text editor. These variables for copy/paste are:

```
obs_lines: observation lines  
bd_lines: boundary lines  
fx_export: fracture data - copy the first 8 columns. The 9th  
           column stores the number corresponding to the  
           entry of
```

```

        fracture name (ex. 'Enter fracture 1: A1'). Here,
        the
        9th column would store '1' and would correspond to
        fracture 'A1' which should be entered in the
        Frac2D
        input file.
nblines:  number of boundary lines (entered near beginning
        of
        Frac2D input file.

```

Definition of variables that might correspond to columns in export data:

```

nblines:  number of boundary lines
num:      number of elements
xbeg:     beginning x-coord of element
ybeg:     beginning y-coord of element
xend:     ending x-coord of element
yend:     ending y-coord of element
kode:     kode=1 means that shear traction, ts, and normal
        traction, tn,
        are prescribed
bvs:      shear stress, MPa
bvn:      normal stress, Mpa

```

Sample run with user input

```

-- BEGIN SETUP --
Enter test name: test5b
Use filter 15x15 (15) or 20x20 (20)? 20

Loading ice shelf stresses...

Enter figure number: 1
Modify principal stresses? (y/n): y
Enter factor by which to multiply principal stresses: 0.75
Getting solution flag matrix...
Computing new deviatoric stress tensor...
Computing new full stresses...
Getting export data...

-- ENTER FRACTURE DATA --
Expected fractures for selected test: s1, s2, or s3, s5
Enter number of fractures: 1

Available fracture names:
fxA0
fxB0
fxC0
fxD0
fxE0
fxF0

```

```

...
fxz7
fxz8
fxz9

Enter fracture 1: fxs5

Number of observation lines: 44
Number of boundary lines: 40

Filter: 20x20
-- REMOTE STRESSES --
Mean boundary stresses: 0.95          1.731          -0.317
Median boundary stresses: 0.876       1.732          -0.351

Mean LEFT boundary stresses: 1.157     -0.138         1.869
Mean BOTTOM boundary stresses: 0.967    -0.326         1.676
Mean RIGHT boundary stresses: 0.828    -0.458         1.632
Mean TOP boundary stresses: 0.864     -0.338         1.753

```

C.3 read_outfile.m

```

SCRIPT: read_outfile.m

REQUIRES functions:
  fread_out.m
  fread_fracs.m
  fread_obs.m
  strip_obs.m
  calc_gridded_results.m
  angp.m
  ave.m
  sig1.m
  sig2.m
  taumax.m

```

This script reads the outfile from Frac2D.

```

variables:
  fig_base:  requested input of power-10 base number for figure
              numbering (ex. fig_base = 2, then fig 1 becomes fig
              21)
  frac_info: array holding stress info for fracture
  1:         fracture number, using <check_fx_num>
  2:         iteration number, using <iter_num>
  3:         tip element number
  4:         k1
  5:         k2
  6:         pangle
  7:         failure
  8:         fracture tip #, using <tip>
  fx:       array to hold fracture data for plotting

```

```

1:      x-coord
2:      y-coord
3:      boolean for original line element (0) or increment (1)
4:      iter num
5:      frac_num from fx_map
6:      line element number
has_data: vector containing boolean values for presence of data
  col 1: frac_info
  col 2: fx_temp
  col 3: obs_temp
my_fx:   array to store fracture data for given iter #
my_vals: array to store obs line data for specified iteration #
obs_file: name of output file with obs line data for given iter
          #
pickfx:   fracture selected for display of stresses (string)
results_file: gridded obs line and fracture data for given iter
            #
test_name: All lookups and automated filenames will be
            generated from the test name

```

Sample run with user input

```

Enter test name: Test5b4r
Plot figures? (y/n): n

```

```

Reading data ...

```

```

Saving output files ...

```

C.4 plot_data.m

```

SCRIPT: plot_frac2d_results.m

```

This script uses saved files from read_outfile.m. Specifically, files of the format 'Test2b_it1_test1_results.mat'. The results are loaded and through user input, different types of plots are generated for a selected test and iteration.

```

to get data from illustrator to km in matlab:
copy x, y data in pixels from illustrator
set to x, y
divide x, y by 8 to get data in km

```

```

* File format for plotting fracture data:

```

```

Array:  my_fx
1:  x
2:  y
3:  incr      1: line increment
              0: original segment

```

```
4: iter_num
5: fx_num
6: elt
```

Sample run with user input

To plot mean stresses, or another variable using contours:

```
Enter test name: Test5b8i
Enter iteration number: 4
Enter plot type (1: contour, 2: pcolor, 3: principal stresses): 1
Plot which variable (S1, S2, tau, g_Sxx, g_Sxy, g_Syy, mean, theta;
enter using
  format {'S1',S1}), leave blank for default Mean: {'mean',mean}
Enter figure base number (leave blank if none desired):
2
```

Please wait a moment...

Carefully select contours for labeling.

When done, press RETURN while the Graph window is the active window.

To plot principal stresses:

```
Enter test name: Test5b8i
Enter iteration number: 4
Enter plot type (1: contour, 2: pcolor, 3: principal stresses): 3
Enter skip amount (leave blank for default 4): 4
Enter figure base number (leave blank if none desired):
2
```